INERTIAL CONFINEMENT FUSION

Lawrence Livermore National Laboratory

ICF Quarterly Report *July—September 1998, Volume 8, Number 4*

Forming Uniform Deuterium Hydride and Deuterium—Tritium Layers in Shells

UCRL-LR-105821-98-4

The Cover: Smooth and uniform 50- to 300-μm-thick deuterium–tritium (DT) layers on the interior of 1- to 3-mm-diam spherical capsules are required for ignitable inertial confinement fusion targets for the National Ignition Facility. In addition, several implosion hydrodynamics issues of cryogenic targets can be investigated with deuterium hydride (HD) or deuterium (D_2) without the difficulties of handling high pressure tritium.

One way to form these layers is to initially freeze hydrogen (DT, HD, or D_2) to an anisotropic multicrystalline solid inside a capsule and then allow a volumetric heat generation to symmetrize the layer. Volumetric heat generation is provided by tritium decay for DT and, in the case of HD or D_2, by pumping the collisionally induced infrared (IR) vibration-rotation band in the solid. The volumetric heating causes the thicker regions of the solid to have a higher temperature and thus a higher vapor pressure. This results in a redistribution of the solid until the inner solid surface is isothermal. We have developed alternate techniques for growing layers by slowly cooling the hydrogen through the triple point. The images on the front cover show the growth of a solid layer from the liquid. These experiments are described more fully in the article "Forming Uniform Deuterium Hydride and Deuterium–Tritium Layers in Shells" on p.131.

On the Web:

http://lasers.llnl.gov/lasers/pubs/icfq.html

UCRL-LR-105821-98-4
July–September 1998

Printed in the United States of America
Available from
National Technical Information Service
U.S. Department of Commerce
5285 Port Royal Road
Springfield, Virginia 22161
Price codes: printed copy A03, microfiche A01.

The *ICF Quarterly Report* is published four times each fiscal year by the Inertial Confinement Fusion / National Ignition Facility and High-Energy-Density Experimental Science (ICF / NIF / HEDES) Program at the Lawrence Livermore National Laboratory (LLNL). The *ICF Quarterly Report* is also on the Web at http: / / lasers.llnl.gov / lasers / pubs / icfq.html. The journal summarizes selected current research achievements of the LLNLICF / NIF / HEDES Program. The underlying theme for this program's research is defined within DOE's Defense Programs missions and goals. In support of these missions and goals, the ICF / NIF / HEDES Program advances research and technology development in major interrelated areas that include fusion target theory and design, target fabrication, target experiments, and laser and optical science and technology.

While in pursuit of its goal of demonstrating thermonuclear fusion ignition and energy gain in the laboratory, the ICF / NIF / HEDES Program provides research and development opportunities in fundamental high-energy-density physics and supports the necessary research base for the possible long-term application of inertial fusion energy for civilian power production. ICF technologies continue to have spin-off applications for additional government and industrial use. In addition to these topics, the *ICF Quarterly Report* covers non-ICF funded, but related, laser research and development and associated applications. We also provide a short summary of the quarterly activities within Nova laser operations, Beamlet laser operations, and the NIF laser design and construction.

LLNL's ICF / NIF / HEDES Program falls within DOE's national ICF Program, which includes the Nova and Beamlet (LLNL), OMEGA (University of Rochester Laboratory for Laser Energetics), Nike (Naval Research Laboratory), and Trident (Los Alamos National Laboratory) laser facilities. The Particle Beam Fusion Accelerator and Saturn pulsed-power facilities are at Sandia National Laboratories. General Atomics, Inc., develops and provides many of the targets for the above experimental facilities. Many of the *Quarterly Report* articles are coauthored with our colleagues from these other ICF institutions.

Questions and comments relating to the technical content of the journal should be addressed to the ICF / NIF / HEDES Program Office, Lawrence Livermore National Laboratory, P.O. Box 808, Livermore, CA 94551.

Work performed under the auspices of the U.S. Department of Energy by Lawrence Livermore National Laboratory under Contract W–7405–Eng–48.

INERTIAL CONFINEMENT FUSION

ICF Quarterly Report July–September 1998, Volume 8, Number 4

In this issue:

FOREWORD

As the incredible construction effort to build the National Ignition Facility (NIF) at Lawrence Livermore National Laboratory (LLNL) reaches its midpoint, we reflect on the inspiring scientific endeavor it represents: to get ignition by inertial confinement fusion in a laboratory. Ignition on a laboratory scale will be one of the greatest scientific achievements of our generation. To achieve it, however, we must discover, develop, and cultivate a broad spectrum of scientific frontiers; this *Quarterly Report* is a snapshot of the broad scientific foundation being constructed. The scientific "bricks" laid down here are significantly more mature and detailed than those only a couple of years ago. A good example of this maturity is shown in the cover article "Forming Uniform Deuterium Hydride and Deuterium–Tritium Layers in Shells" on p. 131, which reveals a significant achievement in condensed-matter physics and the engineering of ignition targets. Very smooth and thick layers of solid deuterium–tritium (DT) on the inside of 1-mm-radius spherical shells are required for all ignition capsule designs for the NIF. However, because solid hydrogen near its triple-point temperature rapidly forms large HCP crystals with flat facets, it has been difficult to form such layers. The work summarized in this article describes a technique for growing such spherical crystal shells of DT for ignition targets and HD or D_2 for surrogate target designs.

The work described in "Sensitivity Studies of Power Imbalance and Asymmetry for NIF Indirect Drive" on p. 140 is part of an ongoing effort to improve, tighten, and distribute the error budget over the many parts of an ignition experiment. Initial specifications for laser power balance and pointing accuracy for indirect drive were established several years ago. This article refines earlier work by using the expected NIF illumination geometry and laser configuration (48 laser-beam quads each with four beams instead of 192 independent beams) and uses a statistical model of the NIF power balance.

To achieve the required radiation drive temperatures on the NIF, it is critical that we control the amount of laser energy scattered out of a NIF hohlraum from both stimulated Raman scattering (SRS) and stimulated Brillouin scattering (SBS). These instabilities are seeded by hot spots in the laser footprint. To reduce these instabilities, several beam-smoothing techniques have been developed over the years. "Calculating and Measuring the Effects of Polarization Smoothing on Scattering Instabilities in a NIF-Like Plasma" on p. 155 presents simulations and experiments confirm that polarization smoothing, which reduces spatial inhomogeneities at short time scales, combined with smoothing by spectral dispersion, provides the greatest reduction yet achieved for SBS and SRS.

One reason the NIF is an affordable project is that new laser technologies have provided significant cost reductions, as exemplified in the NIF amplifiers. "Design and Performance of Flashlamp-Pumped Nd:Glass Amplifiers for the NIF" on p. 162 describes the design and performance of the cost-efficient, compact, combined-beam, large-aperture amplifier to be used on the NIF.

Finally, hohlraum energetics is a key to understanding all indirect-drive measurements as well as designing NIF ignition targets, as discussed in "Status of Our Understanding and Modeling of Ignition Hohlraum X-Ray Coupling Efficiency" on p. 171. Current LASNEX simulations are shown to accurately model the drive for several different hohlraum designs on both the Nova and Omega lasers (at LLNL and at the University of Rochester's Laboratory for Laser Energetics, respectively). These results, which cover a variety of different pulse shapes lasting from 1 to 14 ns, provide confidence that the model drive used for NIF ignition target designs is accurate.

Gilbert Collins
Scientific Editor

FORMING UNIFORM DEUTERIUM HYDRIDE AND DEUTERIUM–TRITIUM LAYERS IN SHELLS

*D. N. Bittner** *B. Kozioziemski* *J. Pipes***
T. P. Bernat *S. Letts* *M. Saculla*
*J. Burmann** *E. R. Mapoles* *J. D. Sater**
G. W. Collins *E. Monsler** *W. Unites*

Introduction

Smooth and uniform, 50- to 300-μm-thick deuterium–tritium (DT) layers on the interior of 1- to 3-mm-diam spherical capsules are required for ignitable inertial confinement fusion (ICF) targets for the National Ignition Facility (NIF).[1] One way to form such layers is to initially freeze DT to an anisotropic, multicrystalline solid inside a capsule and then allow the tritium-decay volumetric heat generation, $Q_{DT} = 0.05\ W/cm^3$, to symmetrize the layer. Volumetric heating causes the thicker regions of the solid to have a higher temperature, thus higher vapor pressure. The result is a redistribution of the solid until the inner DT surface is isothermal. The time constant for such redistribution (when no ^3He is present) is $\tau_0 = H_s\rho / Q_{DT} = 27$ min, where H_s is the heat of sublimation (1580 J/mole), and ρ is the density (0.0503 moles/cm^3) (Ref. 2). If bulk heating were the only factor controlling the layer profile, DT would form a uniform spherical layer inside an isothermal spherical capsule. However, crystal surface stiffness contributes to the final layer shape. The surface smoothes until the thermal energy associated with material redistribution is comparable to the surface energy gained in having to form a higher-energy viscinal surface.[3] The surface structure of a multicrystalline DT film is a function of the DT bulk heating rate and the distribution of crystallite sizes and orientations, which are determined by the initial nucleation and growth.[4]

Several implosion hydrodynamics issues of cryogenic targets can be investigated with deuterium hydride (HD) or deuterium (D_2) without the hazards of handling high-pressure tritium. To generate bulk heat for mass redistribution without tritium radiation, we pump the collisionally induced, infrared (IR) vibration–rotation band. We regulate the solid volumetric heating rate Q_{IR}, thus the redistribution rate $1/\tau_{IR}$, and surface roughness by controlling the incident IR intensity. We have measured laser-power-limited $1/\tau_{IR}$ (thus Q_{IR}) in HD up to 10 times higher than the DT value. The maximum Q_{IR} for hydrogen isotopes is limited by the vibrational relaxation time to $Q_{IR} \approx 1000\ Q_{DT}$.[5] Such large Q_{IR} values enable us to control the hydrogen layer profile and to explore the redistribution process of laser-heated solids.

Forming Uniform HD Layers in Shells

Experimental Overview

We previously measured redistribution time constants τ_{IR} from IR illumination of both solid HD and D_2 at several different wavelengths versus incident IR flux to determine Q_{IR}.[6,7] Our redistribution experiments showed that the illumination of a solid sample with IR radiation resulted in redistribution of the solid in a manner analogous to that seen with tritium heat generation in DT. In a second series of experiments using a similar experimental design, but with a larger sapphire cell, we investigated the surface roughness of a layer formed by illuminating the solid with IR. The illumination pattern of the IR was found to have significant influence on layer shape. The resultant phase-shifting interferometric analysis revealed that surface perturbations with spatial extent greater than the layer thickness have amplitudes that decrease with increasing volumetric heating. The minimum roughness achieved at a given volumetric heating rate was found to depend on the nucleation and subsequent crystal growth during freezing. Both of these experiments

*Schafer Corporation, Livermore, CA
**Allied Signal Inc., Livermore, CA

were effectively one dimensional. A laser beam made one pass coaxially along the inner bore of the cell, and measurements were made by looking through the side of the container or coaxially along the bore of the cell. In the present experiments, we generated 4π illumination of HD inside a 1-mm–outside-diameter (o.d.) spherical capsule and observed the evolution of a uniform solid layer as a function of time and IR intensity.

Experimental Design and Layout

Several issues needed to be addressed in designing our experiments. The first issue was the choice of capsule material. The goal was to heat the HD (D_2 or DT) and not the plastic shell. Therefore, it was important to minimize the amount of IR absorption (heating) by the capsule. Standard plasma polymer, $CH_{1.3}$, used in current Nova experiments has several absorptions overlapping the absorption band for both D_2 and HD. Thus, it would be difficult to redistribute HD or D_2 in shells made of this material. The absorption bands are primarily CH and OH stretch modes. A broadband loss of transmission, which may result from IR scattering, also extends over the entire spectral range of measurement (400 to 5125 cm^{-1}). Therefore, we explored alternatives and found that a CD plasma polymer made with deuterated p-xylene monomer and D_2 flow gas does not have corresponding strong CH absorption lines and has good broadband transmission as well. Furthermore, whereas the OH absorption band increased with time in air, it is controlled by keeping the shell in a dry box. CD plasma polymer was the shell material used for our experiments (Figure 1).

A second issue was the technique for generating uniform IR illumination. The experiments on surface roughness showed that diffuse illumination was necessary to reduce laser-induced coherence effects.

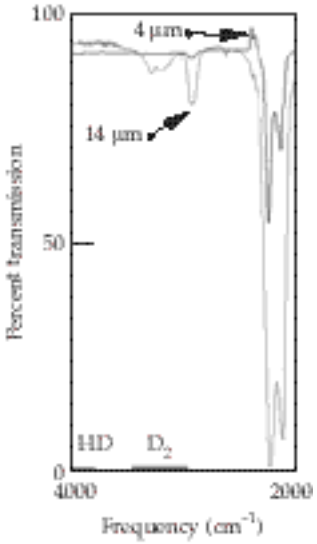

FIGURE 1. IR transmission spectra of 4-μm and 14-μm-thick CD plasma polymer films. Overlapping absorption-band ranges for HD and D_2 are indicated along the bottom of the plot. (08-00-1298-2502pb01)

Calculations showed that illumination uniformity to better than 99% could be achieved[8] by using an integrating sphere. The integrating sphere for our experiments was a vacuum-tight enclosure made from aluminum, with four window ports and an Infragold coating[9] on the inner surface. The Infragold surface is greater than 96% reflecting at wavelengths of interest.

Although we did not perform a systematic study of surface roughness as a function of Q_{IR}, the smoothest surfaces were generated at $Q_{IR} \approx 200$ mW/cm^3. Using this value, we can estimate the IR power requirements for the integrating sphere. The volumetric heating rate is related to IR intensity by $Q_{IR} = \alpha I$, where α is the absorption coefficient [α(HD) ≈ 8/cm], and I is the intensity. The requisite volumetric heating rate is produced by injecting sufficient IR into the integrating sphere to produce the required intensity $I_0 = Q_{IR}/\alpha$. For weakly absorbing layers, $I \approx I_0$, the incident intensity. The capsule is small compared to the integrating sphere, so that most of the power losses occur at the integrating sphere wall and through the viewports. The injected power only needs to be sufficient to compensate for integrating sphere losses of about 4%. This results in a linear relation between laser power and incident intensity, $P_{IS} = 0.04 I_0 A_{IS}$, where P_{IS} and A_{IS} are the injected IR power and surface area of the integrating sphere, respectively. Thus, an intensity of I_0 = 25 mW/cm^2 incident on the 1-mm-o.d. capsule in the center of a 25-mm–inside-diameter (i.d.) integrating sphere requires 21 mW of IR.

Finally, asymmetries in the solid layer, arising from perturbations in the thermal environment caused by the fill tube, needed to be minimized. The fill tube essentially acts as a cooling fin on the shell. Thermal conductance through the fill tube is greater than that of the surrounding helium exchange gas. The difference causes the shell area around the fill tube to be cooler than the rest of the capsule, resulting in formation of a thicker layer in this region. Various means of attaching a fill tube to the capsule were investigated and modeled using the finite element code COSMOS. The final design involved overcoating a composite-shell/fill-tube mandrel with plasma polymer. The resulting capsule was nominally 1-mm o.d. with a 10-μm-thick wall seamlessly attached to a 1- to 2-mm-long by 30-μm-o.d. plasma polymer fill-tube extension.[10]

Figure 2 shows a sketch of the experimental layout. A CD shell containing HD was placed in the center of a 25-mm-i.d. integrating sphere filled with roughly 0.5 Torr of helium exchange gas. The fill line consisted of three sections: a 0.82-mm-long CD tube attached to a 5-mm-long glass tube, which was, in turn, attached to a stainless steel tube. The stainless tube extended through the integrating sphere wall. To minimize IR absorption in the fill line, the glass tube was gold coated. The shell containing HD was illuminated through one pair of viewports by an IR laser beam,

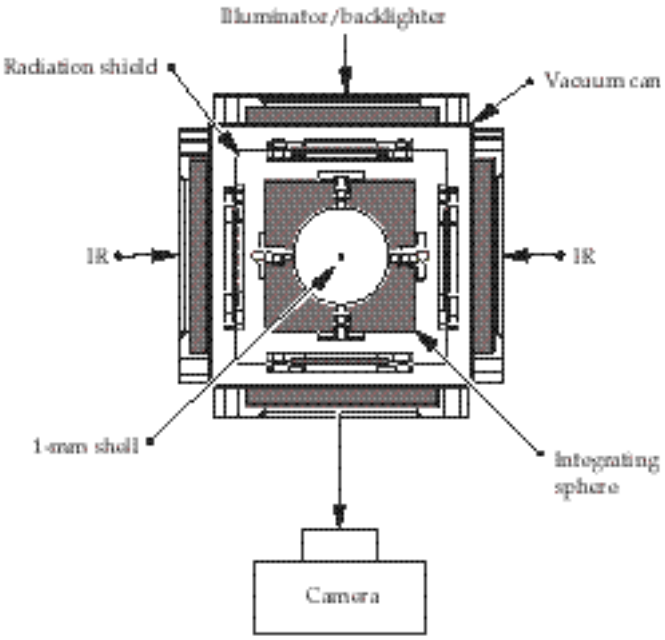

FIGURE 2. Experimental layout indicating the viewing axis and IR injection axis. Sapphire ball lenses on the integrating sphere ports spread the IR beam in an $f/1$ cone. (08-00-1298-2503pb01)

and the layer was monitored along a second orthogonal axis by backlighting the capsule through one port and using a Questar microscope on the opposite port for viewing. Images were acquired periodically during layer formation using a Photometrics 1317×1035 array charge-coupled device (CCD) camera attached to the microscope. Real-time monitoring of the layer was done with a Cohu camera mounted on the microscope eyepiece port. The integrating sphere was thermally and mechanically attached to the cold tip of a helium flow cryostat.

Data Collection and Analysis Procedures

To determine the bulk heating rate, we measured the redistribution time constant τ_{IR}. This measurement was accomplished by filling the capsule with HD, rapidly cooling to approximately 15 K to freeze the HD, and then turning on the IR illumination and collecting images of the evolving layer with time. The HD thickness was typically small near the top of the shell, but grew exponentially with time to form a uniform layer. The exponential time constant is related to the volumetric heating rate by $\tau_{IR} = H_s \rho / Q_{IR}$.

Roughness of the inner solid surface was determined by performing a fast Fourier transform (FFT) analysis of the bright band in the CCD camera images. The bright band can be understood by performing a ray trace[11] through a 1-mm-o.d. shell containing a uniform layer inside an integrating sphere with 4-mm-o.d. ports. The HD-filled capsule acts as a weak, negative lens, resulting in light near the edge of the shell being refracted out of the field of view. Rays internally reflected off the inner solid surface do not leave the field of view and travel through the shell and integrating sphere viewport to the collection optics. Figure 3a shows a closeup view of a bundle of rays incident on the capsule. Figure 3b is an expanded view, showing the rays exiting the integrating sphere through a viewport. Bundles of rays incident on the shell at the largest incident angles consistent with our optical arrangement were traced and found to produce the same bright band.

Refraction also affects the determination of layer thickness. Typically, layer thickness is determined by acquiring an image with the CCD camera, measuring the distance from the bright band to the edge of the shell in pixels, comparing that to the measured distance across the diameter of the shell, also in pixels, and scaling pixels to micrometers using the shell diameter previously determined by standard characterization techniques.[12] If the microscope is focused at the center plane of the shell, then by using this method, one assumes that the rays from the bright band extrapolate in a straight line back to the center of the shell. Figure 3a shows a dashed line extrapolating the rays to the center plane of the shell. The measured, or apparent, layer thickness determined from a camera image is less than the actual layer thickness by the difference between the dashed line and the inner solid surface. To estimate the actual layer thickness, a simple model was generated to calculate both apparent and actual layer thicknesses inside a 10-μm-thick, 1-mm-o.d. plastic shell. The results in Figure 4 show that refractive effects have a significant impact on the measurement of thin layers, especially those less than 100 μm. For example, a 100-μm-thick layer would appear to be only 45 μm thick on the image.

Once the images were shot and stored, the objective of the experiment was to extract an estimate of surface roughness from the stored data. We previously

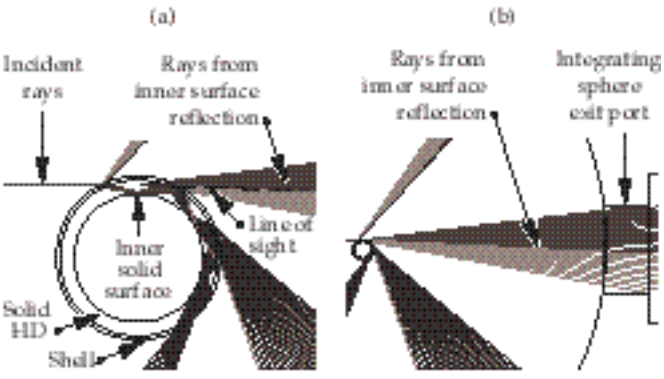

FIGURE 3. (a) Ray trace plot showing the reflection of light off the inner solid surface. (b) Most such light passes out of the integrating sphere through the viewport. (08-00-1298-2504pb01)

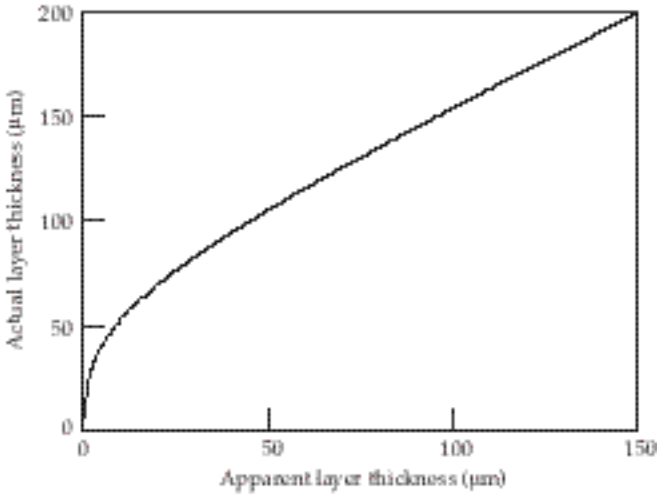

FIGURE 4. Apparent versus actual layer thickness inside a 1-mm-o.d. shell. (08-00-1298-2505pb01)

developed software that locates the surface of the solid in the image.[3] The resultant 1D estimate of solid thickness variations are Fourier transformed to estimate the power spectrum of perturbations on the solid layer.

The software begins by taking an estimate of the center of the bright band in the image and drawing a ray from the center to the edge. At 1-pixel increments along the ray, the intensity is estimated by fitting a plane to the four neighboring pixel values and interpolating to obtain the intensity at the point on the ray. This procedure is done for a series of rays offset by some given angular increment to generate an image of the target in polar coordinates. Each column in the image is then processed to locate the light-to-dark transition associated with the inner edge of the solid. Estimates of the locations of the edge of the bright band are averaged to give a new value of the center of the bright band, and the image is reprocessed until the estimates converge.

A large step in intensity occurs at the inner edge of the solid. Refraction at the inner edge creates intensity minima in the spherical geometry, which are located using an algorithm to find the minima in each ray. Minima are sorted by depth for each ray to give an array of locations as a function of angle for each feature. The profiles can be Fourier transformed and the results used to calculate power spectra for the surfaces. Because we do not locate the shell edge, we do not determine the offset of the inner surface from the capsule (Fourier mode 1), but fit Fourier modes 2 through 128.

Results and Discussion

Layers grown by the rapid-cooling technique typically result in rough, multicrystalline surfaces. Figure 5 shows the evolution of one of the rough layers in which the volumetric heating rate was ~250 mW/cm^3 (or 5 Q_{DT}). The layering process began by performing a controlled liquid fill. Once sufficient liquid was inside the capsule (Figure 5a), the temperature was quickly lowered to freeze the solid (Figure 5b). The randomly grown solid was then illuminated with IR radiation, and redistribution of the solid was recorded with time. Figure 5c shows the resultant layer.

To improve the quality of the inner solid surface, we developed a second technique. The technique is currently performed by manually entering the temperature into a temperature controller while viewing the layer evolution on a monitor. To grow higher-quality layers, we freeze the HD, inject IR radiation into the integrating sphere, raise the temperature of the capsule until the solid just finishes melting, and slowly lower the temperature in approximately 0.005-K steps until freezing onset occurs, at which point the temperature is no longer lowered. If solidification appears to stop, then the temperature would be lowered in 0.005-K steps until a uniform layer forms. Images of the evolving layer were recorded with time. Figure 6 shows an approximately 200-μm-thick layer grown by this technique. Figure 7 is the power spectrum for the solid layer in Figure 6d. The resultant rms for this layer is 2.24 μm. This technique is slightly different from the slow-growth technique used for DT layers, which is

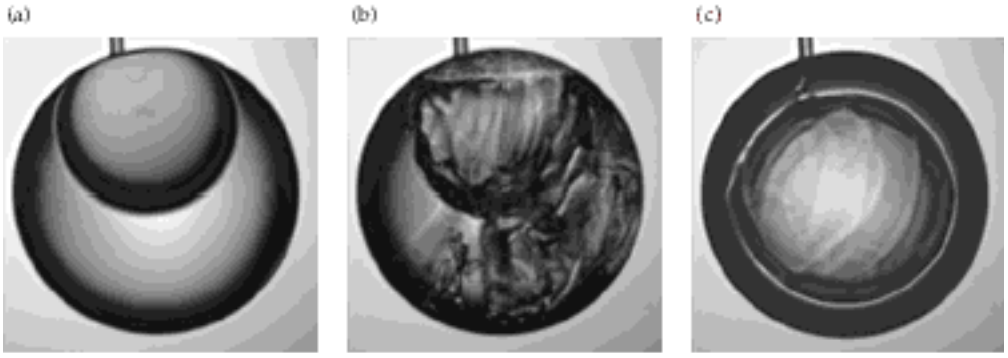

FIGURE 5. To generate a layer from the solid, (a) the capsule is filled with liquid at 16.6 K, (b) the temperature is lowered to 15.8 K to form solid, and (c) upon application of IR, the solid redistributes to form a layer. Layers typically have a rough surface, even after 16 hr in this case. (08-00-1298-2506pb01)

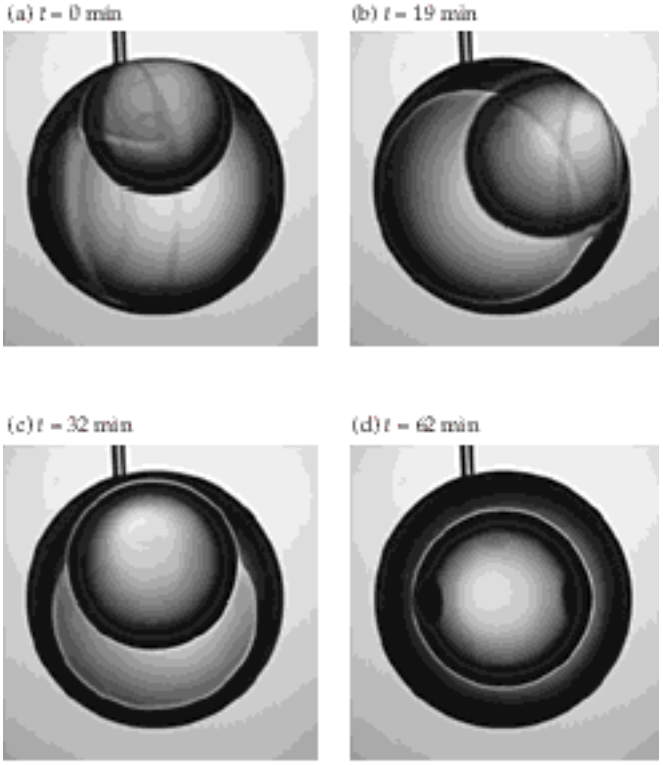

FIGURE 6. In an improved layering technique, IR is continually applied to the capsule. The capsule is warmed to the liquid phase (16.6 K) and slowly cooled until (a) solid starts forming. The temperature is then held constant during the solidification process (b through d). (08-00-1298-2507pb01)

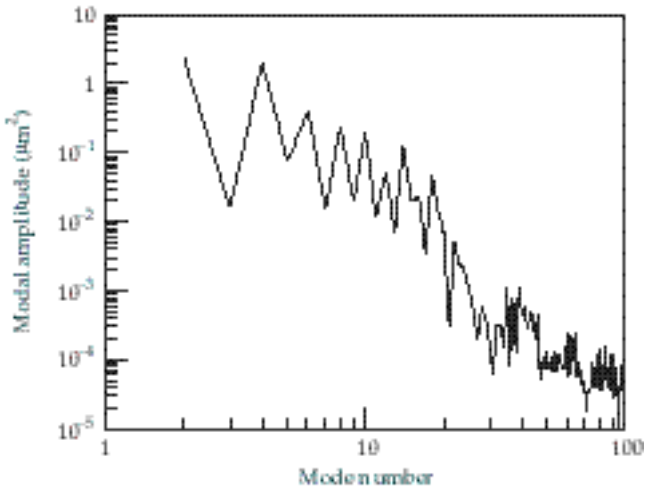

FIGURE 7. Power spectrum for the layer shown in Figure 6d. The rms value of this layer is 2.34 μm. (08-00-1298-2508pb01)

discussed later in this article. Because DT is a mixture, there is no triple point as in a single-component system (D_2), but a three-phase region. The slow-growth technique cools the DT slowly through this region.

Laser power and temperature stability affect the growth of the solid. Higher-quality layers were formed when the temperature was controlled to at least ±5 mK under stable laser power. The impact of the laser is twofold. In addition to generating a given volumetric heating rate, the absorbed energy also raises the temperature of the solid. Variations in laser power cause both volumetric heating rate and temperature variations. Large temperature fluctuations cause the HD to melt and freeze too rapidly, resulting in rough layers. When both systems were stable, it typically took about one hour for layer completion.

As shown in Figures 5c and 6d, some features in the layers are similar in these images. One is a "bump" (or flat spot) near the fill tube. The fill tube has higher thermal conductivity than the surrounding helium exchange gas, producing a cold spot at the fill-tube–shell junction and resulting in a thickening or bump in the layer. The only way to remove this feature is to eliminate the fill tube. The second pair of features, seen at the shell equator, is due to the IR injection method. The IR is injected along an axis through the equator of the shell, resulting in more intense illumination than from the rest of the integrating sphere. The locally warmer areas result in thin spots in the layer. Such features can be removed by alternative injection techniques, such as shaping the beam, inserting a beam block in front of the shell, or, more easily, by initially directing the beam to miss the shell instead of passing through it.

Figure 8 shows a 180-μm layer produced by directly injecting the beam into the integrating sphere. For this arrangement, the sapphire balls were removed, and one beam was injected off-axis at an angle of 11° through the integrating sphere window. Such injection permitted the ~2.5-mm-diam beam to pass through the window, miss the shell, and hit the integrating sphere wall. A thickening of the layer near the fill tube can still be detected, but the thin spots at the equator seen in the previous arrangement are gone. Layers grown using IR illumination are comparable to DT layers grown by the slow-freeze technique. Figure 9 shows the power spectrum for this layer and, for comparison,

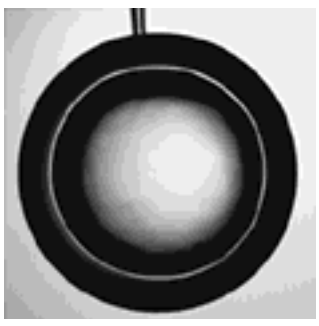

FIGURE 8. Layer formed by direct injection of the IR laser beam after removal of sapphire ball lenses. Thinning of the layer at the capsule equator is no longer evident. (08-00-1298-2509pb01)

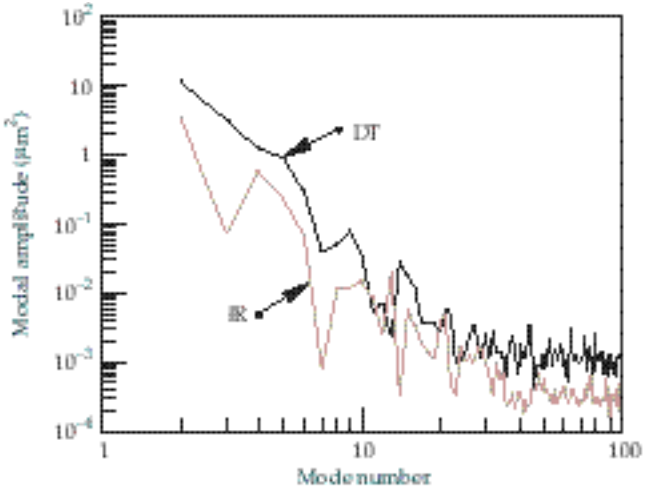

FIGURE 9. Power spectrum for the layer shown in Figure 8 along with a DT layer of comparable thickness. (08-00-1298-2510pb01)

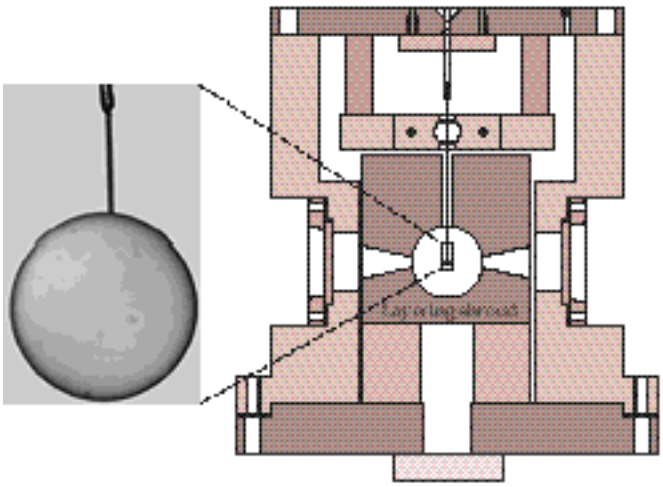

FIGURE 10. Layering occurs in a spherically symmetric geometry. (08-00-1298-2511pb01)

a power spectrum for the ~150-μm-thick DT layer grown by the slow-freeze technique. The IR-generated layer has the same general modal shape as the DT layer.

Forming Uniform DT Layers in Shells

Experimental Overview

We also conducted experiments on a mixture of approximately 25% T_2, 25% D_2, and 50% DT, referred to as DT. The sample was introduced as a liquid in the normal rotational state. Throughout the experiment, $J = 1$ to $J = 0$ conversion occurs continuously, but no measurements were made of rotational content. Our experimental setup, data collection, and analysis were similar to procedures described in a recent paper.[13] The main difference between this experiment and the previous experiment was the replacement of a cylindrical sapphire sample cell with a series of 1-mm-diam plastic shells with 10- to 20-μm-thick walls.

Experimental Design and Layout

A DT ice surface conforms to the isotherms shaped by the surrounding layering shroud. Because a smooth, spherical shape was desired, the layering shroud was a 25.4-mm-diam hollow sphere made of OFHC copper, shown in Figure 10. This shroud provided a constant-temperature, spherical boundary condition. The cell was filled with DT liquid via a fill tube, as shown in Figure 10. A few Torr of ^{4}He gas inside the sphere caused conductive cooling of the plastic shell. The cavity was cooled from the bottom to minimize convection inside the sphere. This design allowed us to study layering in a system quite similar to that required for many ICF target designs.

The plastic shell was placed at the center of the hollow sphere. A pair of 3-mm holes and a pair of 5-mm holes were bored in the layering shroud on perpendicular axes to provide a view of the sample cell. The holes had negligible effect on the spherical isotherms. The shroud was placed inside of a vacuum-sealed secondary container.

Temperature was measured by two calibrated germanium resistance thermometers (GRTs) placed on the top and bottom of the copper cavity. The mean value of the two GRTs was the reported temperature. Temperature stability was better than 2 mK over a period of hours, and temperature resolution was 1 mK. Calibration was checked by measuring the triple point of our D_2 sample, which was 18.72 K, compared to 18.73 K reported for nD_2.[14]

Because the IR and beta layering experiments were of similar design, we were able to share resources. For example, the shells used for both experiments were made from CD plasma polymer. In addition, thermal and ray trace modeling, discussed previously, were applicable to both experiments.

Results and Discussion

Figure 11 shows the evolution of the temperature and rms surface-roughness σ during the course of an experiment carried out on a 3-day-old sample of DT. The value of σ was calculated from modes 2 through 128. In this experiment, we cooled slowly through the triple point at a constant rate of 0.5 mK/min, until the set-point temperature of 19.78 K was reached. The temperature was then held constant for a period of time. The DT layer grows during the temperature ramp,

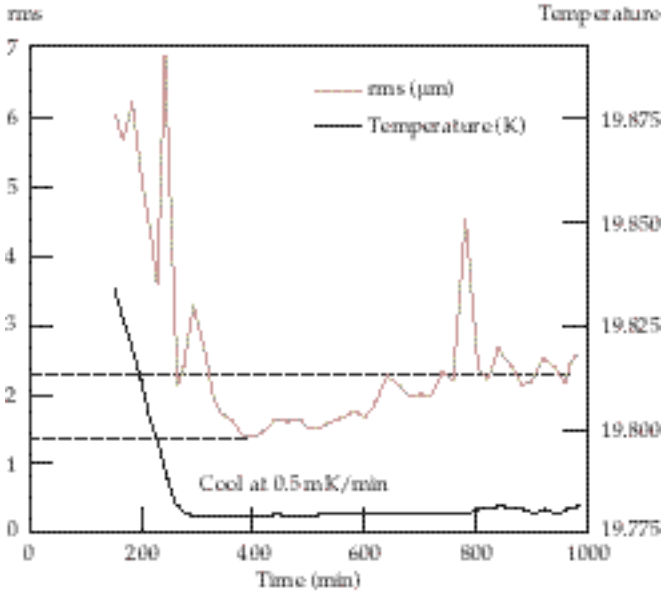

FIGURE 11. The layer smoothes to a minimum value and then roughens with longer times. (08-00-1298-2512pb01)

with a single growth front that begins near the top of the shell. The crystal growth front converges at the bottom of the shell to complete the layer. After formation, T = 19.78 K, time = 295 min, and σ = 2.65 μm. The layer continues to smooth, reaching a minimum σ of 1.15 μm at about 383 min. Afterwards, the layer roughens; however, such behavior is not well understood.

Figure 12 shows the power spectral density for the layer at 400 and 1000 min. The layer at 400 min is smoother at all mode numbers, except perhaps at a singular point at mode 7. Most of the difference between the two layers occurs in modes 2 to 4.

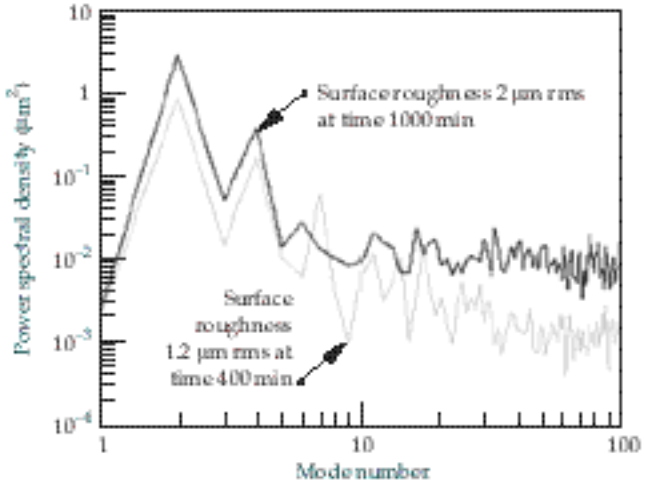

FIGURE 12. An increase in roughness over time after minima is largely due to effects at modal numbers between 2 and 4, although the largest relative increase occurs above mode 20. (08-00-1298-2513pb01)

The freezing rate has a strong effect on layer smoothness. In Figure 13, σ is plotted for a series of 210-μm layers formed at different freezing rates. For rates slower than 3 mK/min, a dramatically smoother layer is produced. At faster freezing rates, the DT nucleates several small crystals instead of growing with a single front. Layers with several distinctly observable crystals are significantly rougher than those formed from a single nucleation site.

Our data indicate that σ increases with decreasing layer thickness. Figure 14 shows a collection of all our

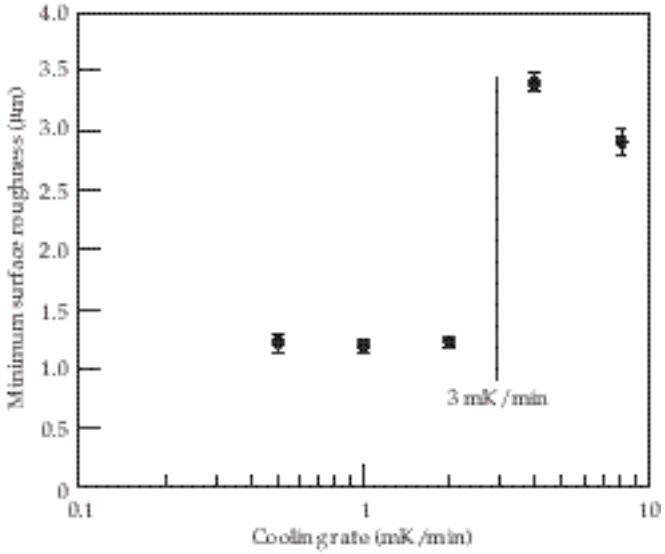

FIGURE 13. Best surface roughness achieved for a series of 210-μm layers created with different cooling rates through the triple point of DT. (08-00-1298-2514pb01)

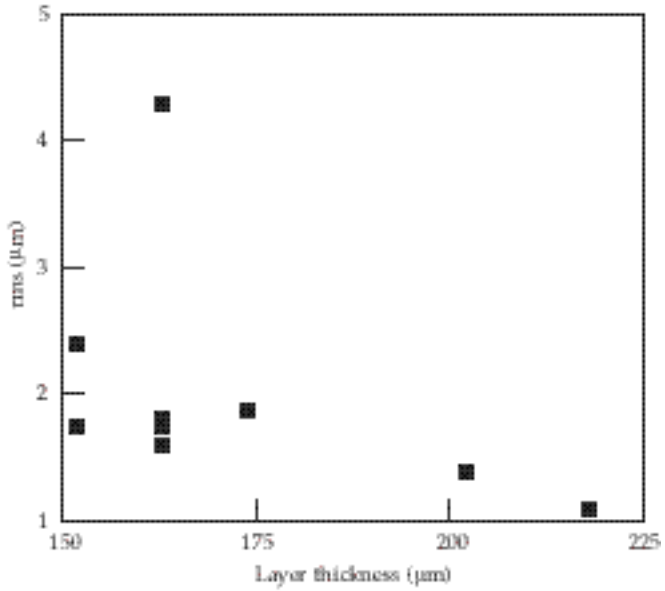

FIGURE 14. Thinner ice layers have a larger σ. (08-00-1298-2515pb01)

layering data with cooling rates between 1 and 2 mK/min and layer thicknesses between 150 and 225 μm. The 4.2-μm point was for a layer formed at the upper end of the cooling rate. Figure 15 shows the power spectral density for a 152-μm layer and a 220-μm layer. The thicker layer is substantially smoother at all mode numbers. This result could be due to the observed relative ease by which thick layers nucleate, compared to thin layers. A contributing factor is the increase in variation of temperature near the ice–gas interface with thicker layers. That is, $\delta T_{bump} = Qh\delta h_{bump}/k$, where δT is the variation from the average temperature at the ice–gas interface, and δh is the variation from the mean ice thickness.

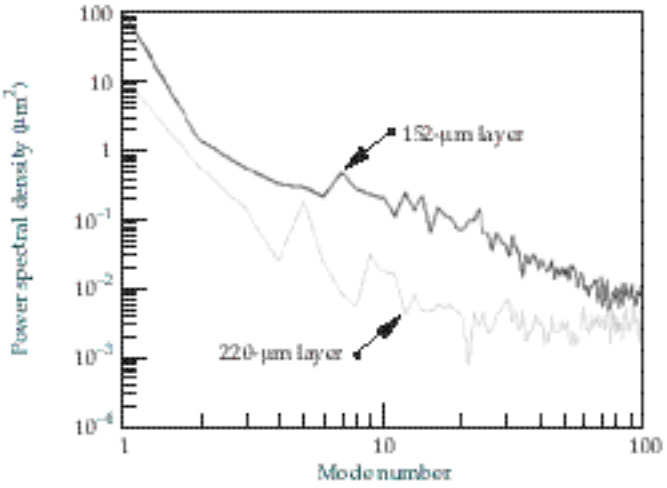

FIGURE 15. Power spectral density plots indicate that a large amount of excess power for the thinner layers is in the middle part of the modal spectrum. (08-00-1298-2516pb01)

The second type of distinct experiment we carried out was a slow, continuous freeze through the triple point of DT to a point well below the triple point. Figure 16 shows the temperature versus time evolution and σ versus time plotted on the same graph. Once again, we observe that the surface reaches a minimum roughness, then at later times becomes quite rough as the layer continues to cool.

Layers at temperatures below T_{TP} – 0.5 K are typically rougher than layers produced just below T_{TP}. Currently, NIF ignition target designs contain 80-μm-thick DT layers at 18 K inside a 2-mm-o.d. capsule. Our best DT layers are produced just below T_{TP} at about 19.7 K. Gas density inside the capsule is ρ_{gas} = 0.7 mg/cm³, instead of the specified ρ_{gas} = 0.3 mg/cm³, and would therefore change the convergence of the ignition capsule design.

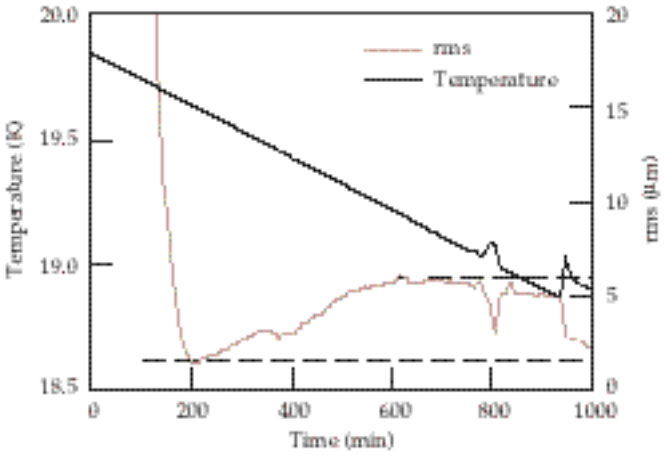

FIGURE 16. With a continuous freeze, the layer reaches a minimum σ early and then degrades. (08-00-1298-2517pb01)

Surface Roughness Model

The equilibrium ice layer minimizes the total free energy at constant volume. The thermal gradient resulting from tritium decay heating favors uniform layers; however, the anisotropic surface energy favors facets. The curved shell geometry prevents the layer from having a single low-energy facet exposed along the entire surface, and any recrystallization to reorient the surface is limited by grain-boundary energy. We can model each of these energies to understand the layer roughness.

The total free energy per unit length is expressed as

$$E_T = \int_A C\rho T dA + \sum_{i=1}^{n} \gamma_s^i L_i + \sum_{i=1}^{n} \gamma_{gb}^i t_i \ , \qquad (1)$$

where C is the specific heat, ρ is the ice density, γ_s^i is the orientation-dependent surface energy, L_i is the length of the crystal facet, γ_{gb}^i is the grain-boundary energy, t_i is the grain-boundary length, and A is the bulk ice area perpendicular to the cylindrical axis.

The c-facet for solid deuterium was determined to have $\gamma = 6 \times 10^{-3}$ J/m² (Ref. 15). The best estimate for γ_{gb}^i is 0.6×10^{-3} J/m², or 10% of the surface energy.[16] Using a 1D heat-flow model for a layer with cylindrical geometry and n regular low-energy facets, as shown in Figure 17, we find that n = 53 minimizes the free energy for a 210-μm layer. The corresponding rms surface roughness is 0.15 μm. The model predicts that rms surface roughness decreases with increasing layer thickness out to 300 μm for a 1-mm shell, consistent with the data in Figure 14.[17] The magnitude of the predicted roughness is smaller by a factor of 10 than the data because of the highly idealized nature of the model. A more detailed model should include multiple crystal orientations and grain-boundary energies.

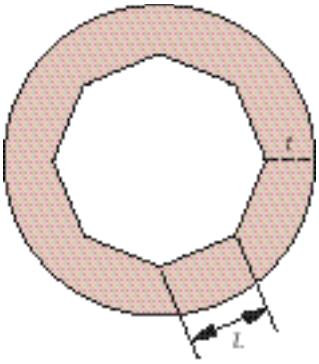

FIGURE 17. Simplified crystal geometry in a DT ice layer. Length of a single crystal facet is denoted as *L*, and *t* is crystal thickness. (08-00-1298-2518pb01)

Summary

We have presented the first results from beta layering in 1-mm plastic shells with fill tubes. Our best beta layers have a roughness as small as 1.2 µm rms for a 210-µm-thick ice layer. Layer smoothness depends on cooling rate as well as layer thickness. Our best DT ice layers are formed when freezing through the triple point is slower than 3 mK/min for 210-µm layers. Data and simple calculations indicate that thinner layers are rougher layers.

We have developed a technique to redistribute and smooth hydrogen (D_2, HD, DT, etc.) layers for ICF by slow solidification with simultaneous pumping of the rotation–vibration absorption bands of the solid. Relatively uniform layers can now be grown with a surface roughness comparable to that of DT. Crystals formed during a quick freeze to the solid phase are not readily smoothed by IR heating. Solid layers slowly grown from the melt were much smoother.

Notes and References

1. J. Lindl, *Phys. Plasmas* **2**(11), 3933–4024 (1995); E. M. Campbell and J. C. Browne, *Science* **271,** 130–132 (1996).
2. A. J. Martin, R. J. Simms, and R. B. Jacobs, *J. Vac. Sci. Technol. A* **6**(3), 1885 (1988); J. K. Hoffer and L. R. Foreman, *Phys. Rev. Lett.* **60**, 1310 (1988); T. P. Bernat, E. R. Mapoles, and J. J. Sanchez, *ICF Quarterly Report* **1**, 57, Lawrence Livermore National Laboratory, Livermore, CA, UCRL-LR-105821-91-1 (1991).
3. G. W. Collins et al., *ICF Quarterly Report* **3**, 81, Lawrence Livermore National Laboratory, Livermore, CA, UCRL-LR-105821-93-3 (1993).
4. *Solids Far From Equilibrium*, C. Godreche, Ed. (Cambridge University Press, Cambridge, 1992). In this article, we ignore effects from ^{3}He born in the solid. The effects of ^{3}He cannot be ignored in DT layers that have aged for longer than ~1 day.
5. C. Y. Kuo, R. J. Kerl, N. D. Patel, and C. K. N. Patel, *Phys. Rev. Lett*. **53**, 2575 (1984).
6. H. P. Gush, W. F. J. Hare, E. J. Allin, and J. L. Welsh, *Can. J. Phys.* **38**, 176 (1960).
7. G. W. Collins et al., *J. Vac. Sci. Technol. A* **14**(5), 2897 (1996).
8. R. B. Stephens and G. Collins, *Fusion Technol.* **31**, 485 (1997).
9. Infragold™ is an electrochemically plated, diffuse, gold-metallic coating. For information, contact Labsphere, North Sutton, NH, 03260.
10. *General Atomics Inertial Confinement Fusion Annual Report*, General Atomics report GA-A22816, UC-712, 5–7 (1997).
11. Ray tracing was performed using the TracePro™ commercial optical modeling program. For further information, contact Lambda Research Corp., Littleton, MA 01460.
12. After pyrolysis, the shells were inspected and measured using a microscope calibrated using a 1-mm-diam reference sphere.
13. E. R. Mapoles, J. Sater, J. Pipes, and E. Monsler, *Phys. Rev. E* **55**, 3473 (1997).
14. P. C. Souers, *Hydrogen Properties for Fusion Energy* (University of California Press, Berkeley, CA, 1986), p. 61.
15. B. J. Kozioziemski, G. W. Collins, and T. P. Bernat, *Fusion Technology* **31**, 482 (1997).
16. W. W. Mullins, *J. App. Phys*. **28**, 333 (1957).
17. DT experiences a 12% shrinkage when cooling through the triple point. Thus, a 1-mm capsule full of liquid at just above the triple point would have a uniform solid layer 253-µm thick just below the triple point temperature.

SENSITIVITY STUDIES OF POWER IMBALANCE AND ASYMMETRY FOR NIF INDIRECT DRIVE

O. S. Jones *S. M. Pollaine*

S. W. Haan *D. R. Speck*

J. T. Hunt *L. J. Suter*

Introduction

The time-averaged radiation asymmetry on a National Ignition Facility (NIF) capsule must be kept to a minimum to achieve high-yield implosions. The radiation asymmetry has an intrinsic component and a random component. Intrinsic asymmetry of the drive arises from a finite number of laser spots on the hohlraum, the presence of laser entrance holes, and coupling of Legendre modes between the cylindrical hohlraum and a spherical capsule. Random asymmetry arises from random variations in the power and pointing of each laser spot.

The emphasis of this article is on random asymmetry. The NIF requirements for power balance and pointing accuracy have already been established. The power balance requirement states that the rms "... deviation in the power delivered by the laser beams from the specified power shall be less than 8% of the specified power averaged over any 2-ns time interval." Similarly, the pointing specification allows for a 50-μm rms deviation in the centroids of the laser spots from their desired locations in the target plane. These specifications are based, in part, on the results of previous radiation viewfactor and radiation hydrodynamics calculations.[1]

Our work is a refinement of the earlier work and differs from it in two ways. First, the illumination geometry and laser configuration have changed substantially since the earlier work was done. The previous work was based on a design using 192 independent laser spots, whereas the NIF is now configured to have 48 quads, with each quad made of four beamlets. The spots from each beamlet in a quad overlap on the hohlraum wall, and the power to each beamlet in a quad is not completely independent because the same preamplifier module (PAM) feeds all beams in a quad. Second, rather than simply randomly varying the laser power to each spot, we have created a statistical model of the NIF laser and used it to predict power balance as a function of time for a given pulse shape.

Figure 1 shows laser power versus time for a single outer-cone beam for the NIF-baseline, 1.8-MJ, indirect-drive pulse. (For indirect drive, the beams are divided into inner and outer cones, and pulse shapes for each are slightly different.) We refer to the initial, low-intensity part of the pulse (roughly, the first 14 ns of the pulse) as the foot. We refer to the remainder of the pulse as the peak. Our overall approach to estimating flux asymmetry on the capsule for this pulse consisted

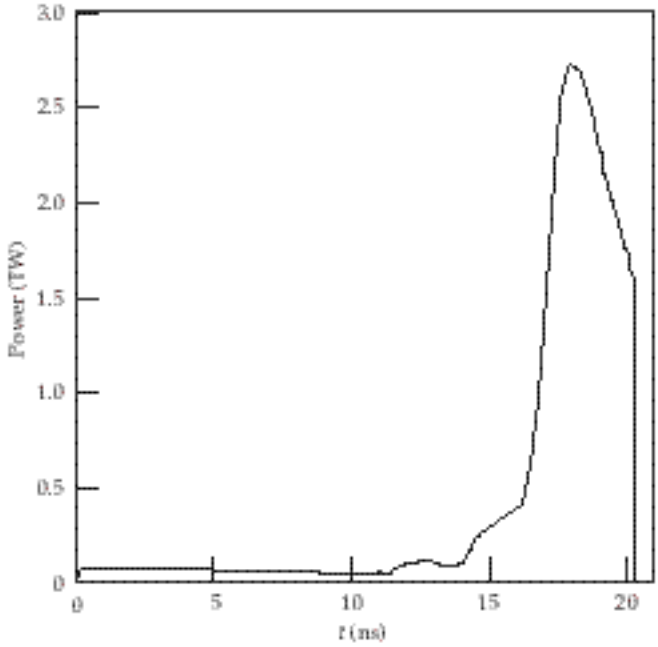

FIGURE 1. Laser power versus time for a single outer-cone beam for the NIF-baseline, 1.8-MJ, Haan indirect-drive pulse.
(50-00-1298-2545pb01)

of first estimating the random variations in laser power and pointing as a function of time. To do so, we developed a statistical model of the NIF laser system. Next, we used the radiation viewfactor code (Gertie, which is described in more detail later) to relate the random power and pointing distributions to flux asymmetry on the capsule at two times: the middle of the foot and the middle of the peak. Finally, we decomposed the flux asymmetry into Legendre modes and used linear growth factors from LASNEX capsule calculations to estimate the magnitude of each mode at ignition.

This article first describes the results of the statistical model of the NIF laser power balance. The calculation yields beam-to-beam and quad-to-quad power balance as a function of time. Next, we describe the radiation viewfactor calculations. These calculations yield the sensitivity of capsule flux asymmetry and spatial rms at ignition to the amount of power imbalance and pointing error. Finally, we provide our best estimate of capsule flux asymmetry during the foot and peak, from the power balance results, and use linear response coefficients to estimate the peak-to-valley variation in the hot-spot radius at ignition.

Laser Power Imbalance

The time-averaged (2-ns averaging time) deviation in power of a given beam, $P(t)$, from the desired power curve $P_0(t)$ is

$$\frac{\Delta P(t)}{P_0(t)} = \frac{1}{2}\int_{t-1}^{t+1} \frac{P(u) - P_0(u)}{P_0(u)}\, du \ , \qquad (1)$$

where u is a dummy variable of integration. The rms power imbalance is then

$$\sqrt{\frac{1}{N}\sum_{j=1}^{N}\left(\frac{\Delta P(t)}{P_0(t)}\right)_j} \ , \qquad (2)$$

where N is the total number of power-versus-time curves over which we average. For example, if we average over 10 shots and all 192 beams, then N is 1920. The NIF requirement is that the rms power imbalance must be less than 8%.

Power balance is a systemwide issue on the NIF. A certain level of random variations (also referred to as shot-to-shot variations or jitter) in power output of a given beam will occur, and this level will depend on the jitter levels of various laser subsystems. In addition to shot-to-shot variations, each of the 192 beams will, on average, yield a different output pulse if given identical input pulses. Such repeatable or systematic differences among beams must be minimized to meet the power balance requirement. In addition, the power measurement system must accurately measure the power history so that adjustments can be made to bring the output to the required balance.

We have developed a computer model of the NIF laser system to estimate the power balance. The model has been used to determine the allocation of random variations to subsystems, and to develop procedures for minimizing repeatable differences among beams.

NIF Power Balance Model

Two types of variations in laser performance lead to power imbalance: random (shot-to-shot) variations and systematic (repeatable) variations. Figure 2 identifies the sources of random and repeatable variations in beam power that are included in our model. The sources are the optical pulse generation (OPG) subsystem, the 1-μm laser, and the frequency-conversion and ultraviolet (UV) optics (0.35-μm) subsystem. Systematic differences are caused by differences in gain, transmission, beam area, and frequency conversion that repeat from shot to shot. Random variations are caused by shot-to-shot fluctuations in the OPG output (pulse injected to main laser), amplifier gain, pulse arrival time, and frequency conversion. In addition, a 4% rms random uncertainty arises from measurement of the power.

The laser-output pulse for a given injected pulse is predicted using the BTGAIN code.[2] BTGAIN models the propagation of an optical pulse through a laser chain consisting of a series of components having specified transmissions and gains. For the calculations in our study, the transmissions and gains represent average values over the beam cross-sectional area. Elements having gain (amplifier slabs) are modeled using Frantz–Nodvik theory,[3] which accounts for the gain depletion of an amplifying medium as an optical pulse travels through it.

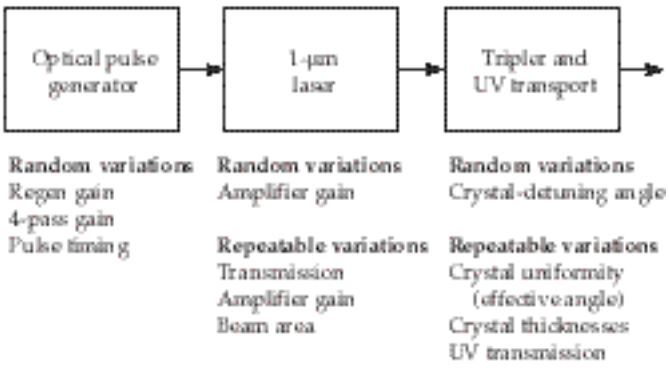

FIGURE 2. Schematic of the NIF laser showing sources of power balance included in the model. (50-00-1298-2546pb01)

Frequency conversion is calculated within BTGAIN from a table relating 1ω input intensity to 3ω output intensity. The conversion table is generated in a separate step by the THGFT02 code,[4] which calculates the frequency conversion for an arrangement of conversion crystals of given thicknesses and angles with respect to the beam axis (detuning angles). A decrease in frequency-conversion efficiency with imposed bandwidth is included.

The NIF model consists of 192 beams having repeatable differences in performance. That is, given identical input pulses, the beams produce different output pulses. The repeatable differences are modeled by assuming a random variation in optical properties (transmission, gain, frequency-conversion efficiency, and so forth) of the components that make up each beam. Table 1 shows the mean values and standard deviations of the amplifier gain coefficient and transmissions of optical components. The gains and transmissions are assumed to obey a Gaussian distribution. The mean values and standard deviations in Table 1 are consistent with the NIF optical specifications for the various components.

Each of the 192 beams has its own frequency-conversion curve (3ω versus 1ω intensity) that represents the repeatable performance of each converter. The baseline frequency converter has a doubler crystal thickness of 11.0 mm, a tripler crystal thickness of 9.0 mm, a doubler detuning angle of 240 μrad, a tripler detuning angle of 30 μrad, and 30 GHz of bandwidth. Systematic differences in frequency conversion are assumed to arise from beam-to-beam variations in average crystal thickness and from beam-to-beam variations in the effective detuning angle between the beam axis and the doubler crystal (the tripler crystal conversion is relatively insensitive to angle).

Figure 3 shows the power imbalance for beams with crystal thickness or doubler detuning angle different from that for the reference converter, compared to the same beam with the reference converter. We assume the doubler thickness varies uniformly from 11.0 to 11.2 mm, resulting in a 2% variation in frequency-conversion efficiency at the foot intensity, and less variation at higher intensity. Similarly, the tripler thickness varies from 9.0 to 9.2 mm, which results in a 3% variation in conversion efficiency at the foot intensity, and less at higher intensity.

Spatial nonuniformities in the crystals cause the local detuning angle to vary across a given crystal. The spatial variation in angles will differ for each crystal, so the overall (spatially integrated) conversion efficiency will vary systematically from beam to beam. We assumed that the distribution of conversion efficiencies among beams could be modeled by a Gaussian spread in the doubler detuning angle with a standard deviation of 28.6 μrad. The result is about a 3.5% rms deviation in frequency-conversion efficiency at the foot intensity, and less deviation at higher intensity. Because our assumption is highly conservative, actual systematic differences among crystals should be less than this value.

In addition to systematic differences among the 192 beams, the output of each beam will vary randomly from shot to shot about its average. Random variations in laser output depend on several factors,

TABLE 1. Mean and standard deviation (sigma) of component gains and transmissions.

Component	Mean value	Sigma
Amplifier gain coefficient	0.05 / cm	0.00125 / cm
Transmission coefficients		
Laser glass at Brewster's angle	0.9945	0.0015
Sol gel AR per surface	0.995	0.0015
KDP switch crystal	0.934	0.002
Polarizer transmission	0.97	0.005
Polarizer reflection	0.98	0.002
Multilayer dielctric mirror	0.99	0.0015
Doubling-crystal AR per surface	0.995	0.0015
Tripling-crystal AR per surface	0.995	0.0015
Focus lens	0.99	0.0015
Color-separation grating	0.977	0.005
Kinematic phase plate	0.97	0.003
Debris shield	0.98	0.003

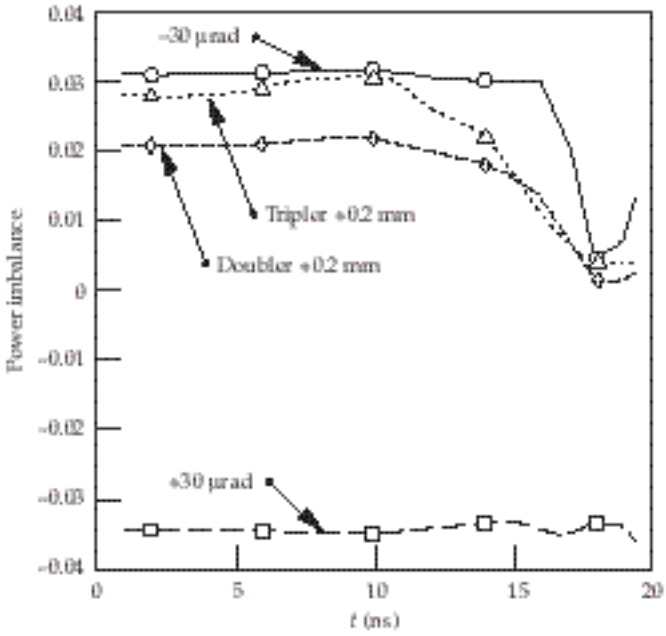

FIGURE 3. Power imbalance versus time for beams having different frequency-conversion crystal thicknesses or detuning angles than the reference beam. (50-00-1298-2547pb01)

some of which are correlated for beams in the same quad or bundle (a bundle is a pair of quads driven by a common set of capacitor banks). The fact that some variations are correlated among beams is important because the power imbalance will be greater than if the beams were completely independent.

Table 2 lists the sources of jitter in measured power, shows the allowable rms variation for each source (in some cases, values were established as a result of this study), and shows how the source is correlated among beams. For example, random variations in the injected pulse from the OPG are due to variations in gains of the regenerative and rod amplifiers that are part of each PAM. Because there is one PAM per quad, this source is correlated for beams within a quad. Pairs of quads (bundles) are driven by common capacitor banks, so the jitter in the main amplifier gains is correlated for the eight beams in a bundle. Jitter in the pulse-arrival time results in power imbalance only when the pulse shape is changing. For the Haan pulse, timing jitter contributes a maximum of 3.2% rms power imbalance during the period of steepest slope just before peak power. The allocated jitter in the doubler detuning angle (from jitter in the beam angle) results in 1.9% rms variation in frequency conversion at the foot intensity, and less at higher intensity.

Influence of Frequency Conversion and Gain Saturation on Power Balance

Frequency conversion and gain saturation have large effects on the time-dependence of power imbalance for shaped pulses. First, the intensity dependence of conversion efficiency amplifies the 1ω power imbalance, especially at low intensity. Second, gain saturation tends to reduce power imbalance, especially late in the pulse when gain saturation is greatest. Both factors tend to make the power imbalance the largest at the beginning, or foot, of the pulse when the intensity is lowest.

Figure 4 shows conversion efficiency as a function of 3ω intensity. At an intensity of 0.043 GW/cm^2, which corresponds to the foot of the Haan, 1.8-MJ, indirect-drive pulse, the frequency-conversion efficiency increases rapidly with increasing intensity. At the peak intensity of the Haan, 1.8-MJ pulse, the variation with intensity is much less.

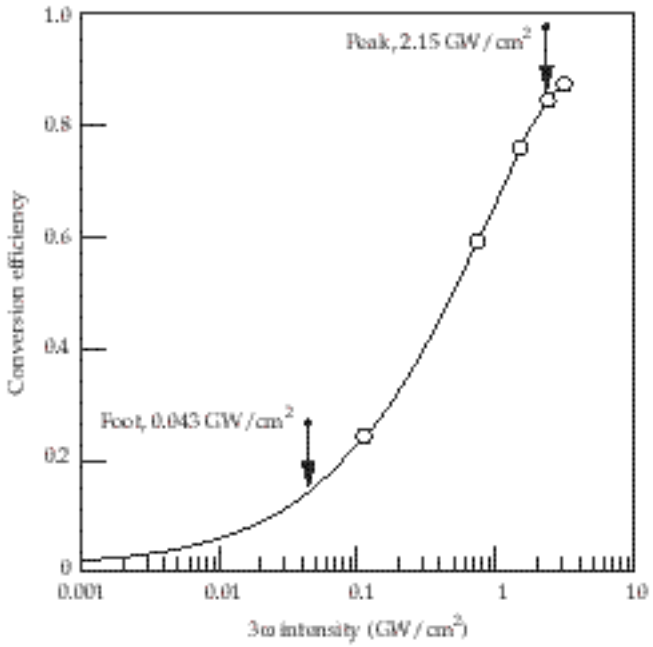

FIGURE 4. Frequency-conversion efficiency versus 3ω intensity. (50-00-1298-2548pb01)

In general, 3ω intensity out of the frequency converter is related to 1ω intensity into the converter by

$$I_{3\omega} \approx I_{1\omega}^{n} \ , \tag{3}$$

where the exponent n varies between 3 at very low intensities and 1 at very high intensities. Taking the logarithmic derivative of this expression, we find that the change in intensities is related by

$$\frac{\Delta I_{3\omega}}{I_{3\omega}} = n \frac{\Delta I_{1\omega}}{I_{1\omega}} \ . \tag{4}$$

Figure 5 shows the exponent n as a function of 3ω intensity. In the foot of the pulse, the 1ω power balance entering the frequency converter is amplified by a factor of 2.4. At the peak of the pulse, the amplification

TABLE 2. Subsystem allocations and correlations for sources of random power imblance.

Source	Allocation	Correlation
Injected power (from OPG)	3%	Beams in a quad (4)
Amplifier gain	2%	Beams in a bundle (8)
Frequency conversion	16 μrad	Uncorrelated
Pulse timing	30 ps	40% quad, 60% uncorrelated
Measurement	4%	Uncorrelated

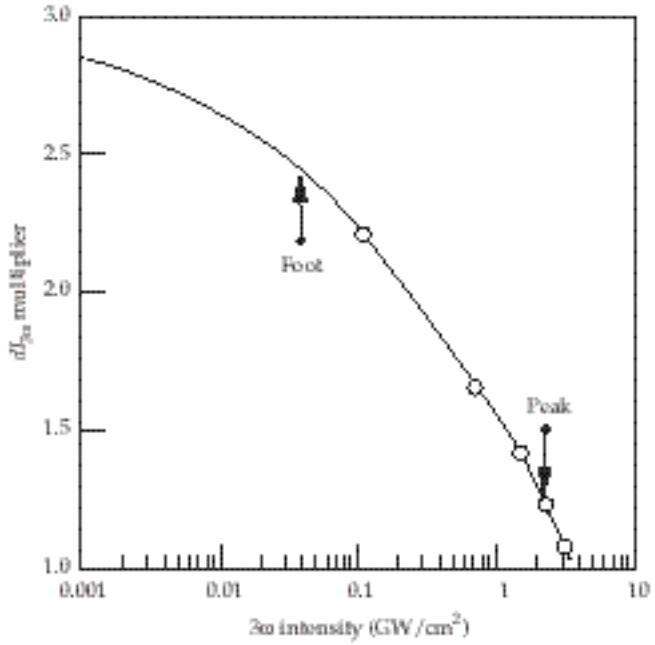

FIGURE 5. 1ω to 3ω power imbalance amplification factor versus 3ω intensity. (50-00-1298-2549pb01)

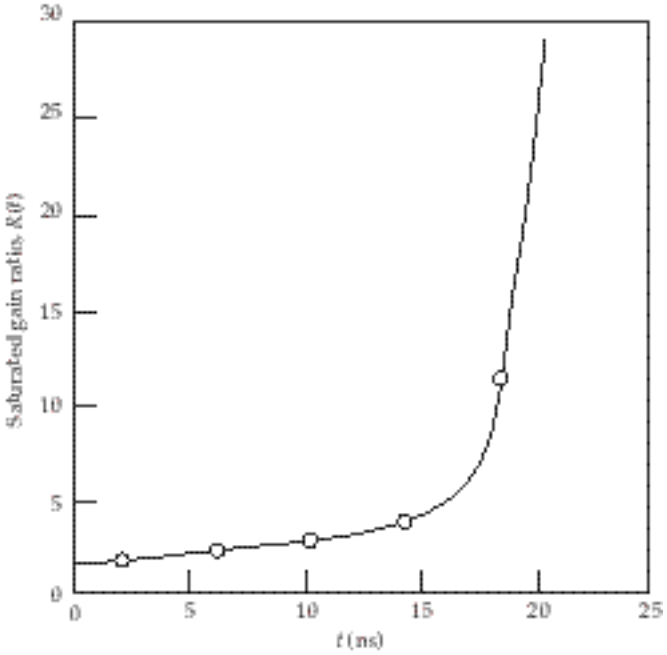

FIGURE 6. Saturated gain ratio versus time for the 1.8-MJ Haan pulse. (50-00-1298-2550pb01)

is only about 1.2.

As energy is extracted from amplifier slabs during a laser pulse, fewer excited atoms remain in the glass, and the gain is reduced. We call the ratio of small signal gain to actual gain the saturated gain ratio (or square pulse distortion). Figure 6 shows the saturated gain ratio as a function of time during the Haan pulse. The ratio increases from about 1.7 at the beginning of the pulse to more than 20 by the end. The reason the gain ratio is not 1 at $t = 0$ is that this is a multipass laser. During the final pass through the laser, even the foot of the pulse is passing through laser slabs that have already had significant energy extracted by previous passes of the entire pulse. The curve in Figure 6 is specific to the Haan pulse, but it is possible to write a more general expression for the gain ratio as a function of the amount of 1ω energy extracted from the laser. For a single-pass amplifier, there is a simple analytical expression; however, for the multistage, multipass NIF design, the expression is not so simple. Using BTGAIN, we obtained the following curve fit

$$R(E) = A \exp(BE), \tag{5}$$

where $E(t)$ is the ratio of amount of 1ω fluence (energy per area) extracted from the laser at a given time in a pulse to the saturation fluence (4.5 J/cm^2). The coefficients A and B depend on the total amount of normalized 1ω extracted fluence E_{tot}. The coefficients are

$$A = 0.79174 + 0.0093524\,(E_{tot}) + 0.0013361\,(E_{tot})^2\ , \tag{6}$$

and

$$B = 1.2078 - 0.55346(E_{tot}) + 0.56418\,(E_{tot})^2 - 0.22564(E_{tot})^3 + 0.035275(E_{tot})^4\ . \tag{7}$$

The expression is independent of pulse shape, and it applies for E_{tot} from 0.8 to 3.4. For the 1.8-MJ Haan pulse, E_{tot} is about 3.4.

If we know how the laser saturation and frequency-conversion exponent vary as a function of time for a given pulse, then we can estimate the random component of 1ω power imbalance as a function of time. Ignoring timing errors, the variation in 1ω power depends on the amount of variation in injected power (from the OPG) and the gain. Using a simplified analysis for a single-pass laser, and assuming that the logarithmic derivatives of the injected power and gain do not change significantly during the pulse, the 1ω power balance is related to these two sources by

$$\frac{\Delta P_{1\omega}(t)}{P_{1\omega}(t)} = \frac{1}{R(t)}\left(\frac{\Delta P_{inj}}{P_{inj}} + \frac{\Delta G_0}{G_0}\right)\ . \tag{8}$$

As energy is extracted from the laser, the gain ratio increases, and 1ω power imbalance decreases. To obtain the contribution of this part of the 1ω power

imbalance to 3ω power imbalance, we simply multiply the above expression by the frequency-conversion exponent. By adding this contribution in quadrature with estimates of the remaining contributions to power imbalance, we could estimate the power imbalance as a function of time. However, for highly saturated pulses, it is more accurate to extract the time-dependent 3ω power imbalance directly from BTGAIN calculations, which is what we have done in this work.

Minimizing Systematic Variations in Laser Power

By systematic variations in laser power, we mean that if the same pulse is repeatedly injected into a given laser beam, it will, on average, yield an output pulse that differs somewhat from the output pulse of the average beam. Systematic differences can arise from several factors, including differences in beam area, component transmissions, amplifier gains, and frequency conversion. Systematic variations in laser-power output must be made as small as possible for the system to meet the power balance requirement.

The simplest and most effective way to compensate for systematic differences is to increase the injected energy to consistently low beams and decrease injected energy to consistently high beams to minimize the systematic power imbalance at t = 1 ns, where the power imbalance is always highest for shaped, indirect-drive pulses. This approach works well because gain saturation and the intensity dependence of frequency conversion allow us to adjust the power in the foot of the pulse without changing the power imbalance in the peak very much.

Such a procedure requires setup shots in which all beams are given the same injected pulse, and the power in the foot of each pulse is measured and compared to the average value. The injected pulse is a nearly flat, 20-ns pulse that yields a flat output pulse at the same intensity as the foot of the Haan pulse. Because the pulse is flat, power can be inferred from an energy measurement, whose accuracy is better (2.8%) than that of the power measurement (4%). By averaging over four shots for each beam, accuracy is further improved to 1.4%. The injected energy to each beam is then adjusted to eliminate the systematic difference in power at t = 1 ns. The energy to each beam is adjusted by setting the PAM energy and adjusting the half-wave plates in the optics that split the beam from the PAM into four beams.

Although it is somewhat surprising, it appears that using a single input pulse shape (calculated by BTGAIN using average laser components) for all 48 PAMs is sufficient. That is, setting 48 different input pulse shapes to tune out systematic quad-to-quad differences results in only a marginal improvement in power balance. Figure 7 shows the results of a simulation in which we compared the performance of 192 lasers with randomly selected 1ω components and identical frequency converters. For each beam, we used BTGAIN to compute the input pulse shape that resulted in exactly the same output pulse for all the beams. The curve labeled "192 pulse shapes" shows that the rms power imbalance is zero when these input pulse shapes are used. Next, we averaged the input pulse shapes for each pair of beams to obtain 96 different pulse shapes. We averaged the input pulse shapes for each set of four beams to obtain 48 pulse shapes (one for each quad). We then compared the cases to that for a single input pulse shape. There is little difference in beam-to-beam power imbalance when comparing 1 pulse shape to 48 pulse shapes.

Figure 8 shows the systematic rms power imbalance

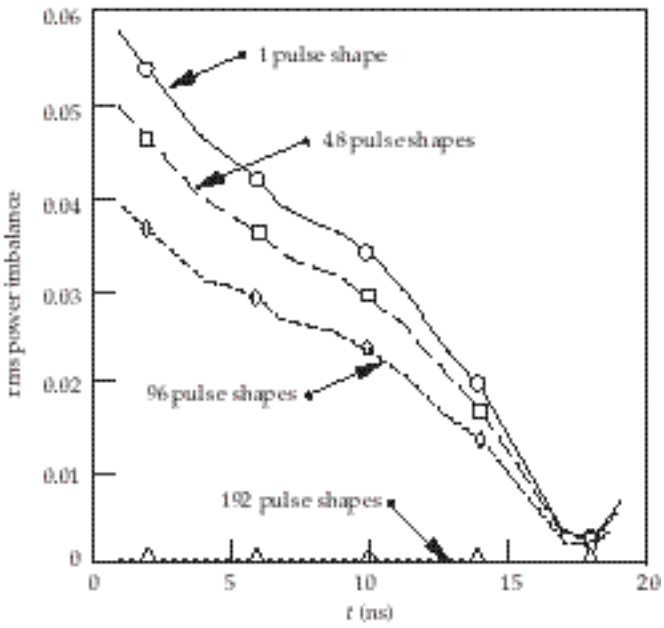

FIGURE 7. Sensitivity of systematic, beam-to-beam power imbalance to the number of independent pulse shapes. (50-00-1298-2551pb01)

(3ω) for the 192 beams of the power balance model with and without injection-energy correction. The upper curve is the systematic spread in power that arises from the differences in component performances when each beam is injected with the same energy. The uncorrected systematic power imbalance is clearly much too large to meet NIF requirements. The lower curve shows the rms power imbalance after adjusting injected energies to balance the power at t = 1 ns. It is

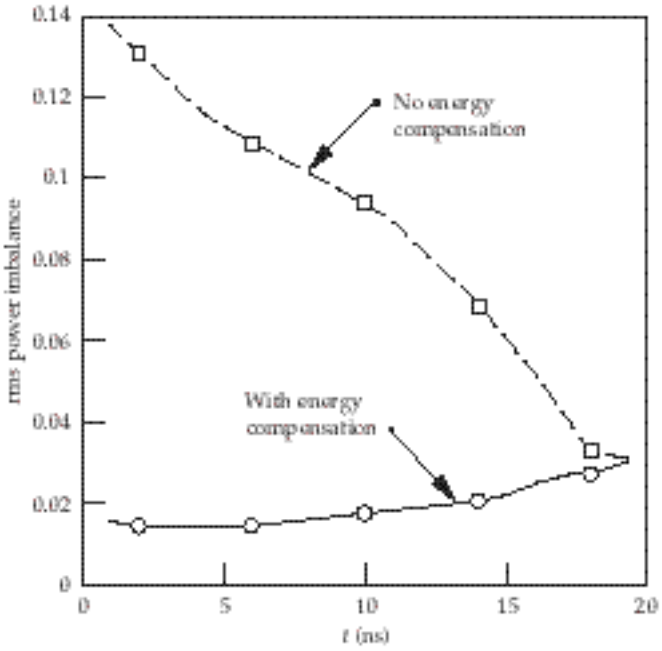

FIGURE 8. Systematic rms power imbalance as a function of time for the 1.8-MJ Haan pulse with and without injected-energy compensation. (50-00-1298-2552pb01)

approximately equal to the 1.4% measurement error at 1 ns, and rises to about 3% by the end of the pulse. In both cases, we used a single pulse shape.

Figure 9 shows the spread in injected energies of the 192 beams required to tune out systematic errors. The spread in energies is approximately Gaussian, with an 11% rms variation about the mean. The relatively large spread in energies is good, because it means the adjustment has some resolution. Figure 10 shows two histograms that compare the spread in 1ω power at t = 1 ns for the uncompensated case and the compensated case. Figure 11 shows the same kinds of plots, but for 3ω power at the target. Without compensation, the 1ω systematic rms power imbalance is 5.65%, which is then amplified by the frequency-conversion process to 13.8%.

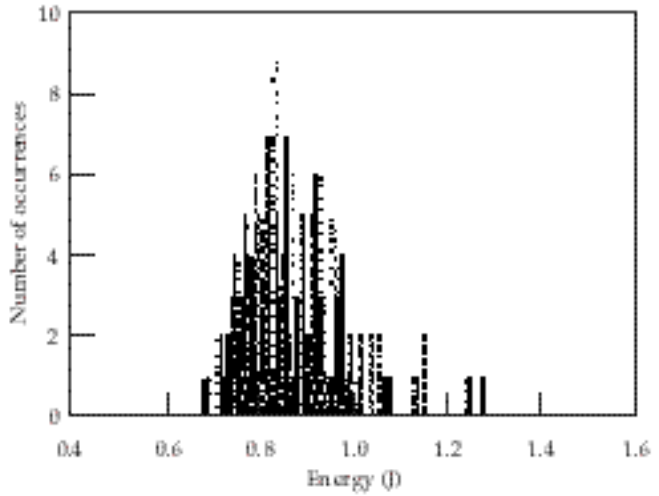

FIGURE 9. Histogram of the spread in injected energies required to tune out the t = 1 ns power imbalance. (50-00-1298-2553pb01)

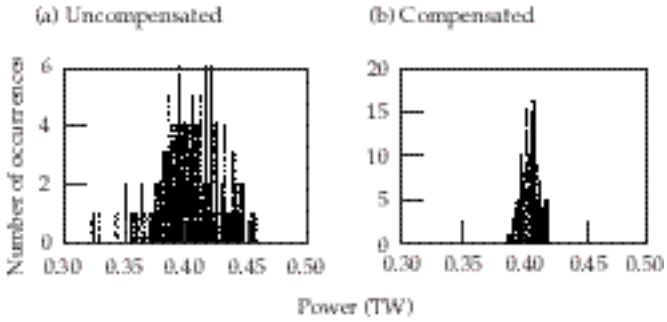

FIGURE 10. Histograms comparing the spread in 1ω power at t = 1 ns for the (a) uncompensated and (b) compensated cases. (50-00-1298-2554pb01)

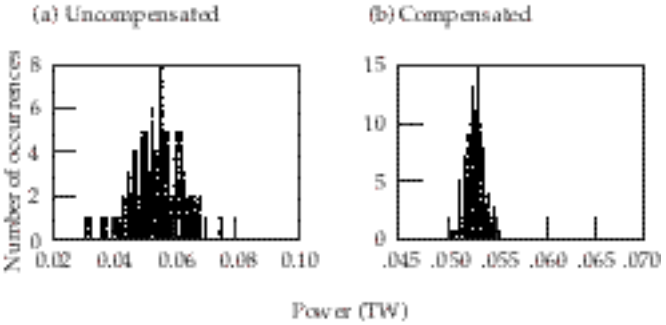

FIGURE 11. Histograms comparing the spread in 3ω power at t = 1 ns for the (a) uncompensated and (b) compensated cases. (50-00-1298-2555pb01)

Estimate of Overall Laser Power Imbalance

We included all known sources of random and systematic errors to obtain an estimate of the overall power imbalance. Such an estimate can be used as a basis for the flowdown of requirements to the subsystems and to confirm that our strategy for minimizing systematic power balance errors will result in a total error that meets the NIF power balance requirement. We averaged over 192 beams and 10 shots (1920 power-versus-time curves) to obtain the rms values for these calculations.

Figure 12 shows beam-to-beam, quad-to-quad, and intraquad rms power imbalances versus time. The beam-to-beam imbalance for a single calculation can be obtained from Eqs. (1) and (2), with N = 192. We then take the rms average over the number of runs to obtain the final result. The quad-to-quad imbalance is

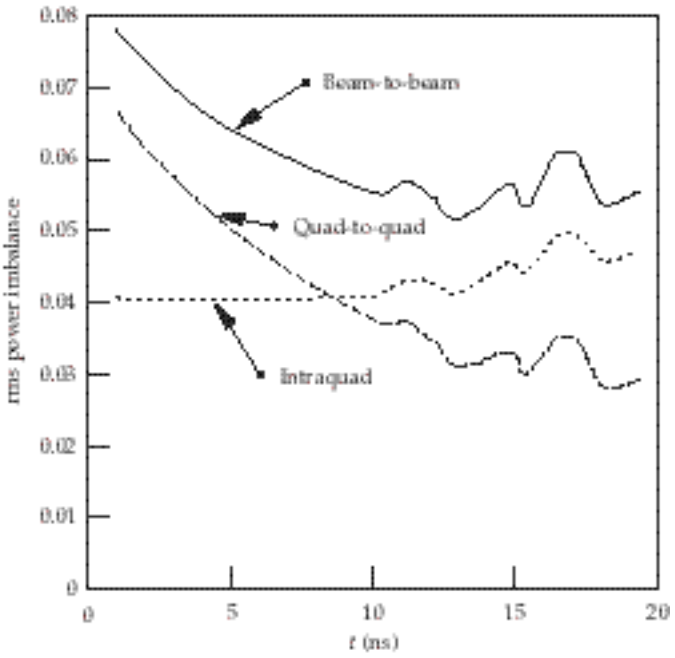

FIGURE 12. Total rms power imbalance versus time for the 1.8-MJ Haan pulse. (50-00-1298-2556pb01)

obtained by averaging over the four beams in each quad to obtain the power in each quad, taking the rms average over the 48 quads, and then taking the rms average over the number of runs. The intraquad imbalance is a measure of the imbalance for beams in the same quad. It is the square root of the difference between the square of the beam-to-beam imbalance and the square of the quad-to-quad imbalance. The rms beam-to-beam power imbalance is 7.8% at t = 1 ns, and decreases to about 6% by the end of the pulse. The bumps in the curve appearing late in the pulse are due to timing jitter during pulse-shape changes. The value we obtained is less than the NIF 8% limit for the entire pulse. To meet the overall NIF power balance requirement, we reduced the allowable random variation in amplifier gain from its original allocation of 3% to 2%.

If the beams were completely independent, then the quad-to-quad imbalance would be exactly half the beam-to-beam imbalance because the power in each quad would be the average of four independent quantities. Early in the pulse, power imbalance is dominated by the OPG and amplifier jitter, which are correlated for beams within a quad, so the quad-to-quad imbalance is much more than half of the beam-to-beam imbalance. By the end of the pulse, these sources of imbalance make a relatively small contribution to the total, and the beams are largely uncorrelated. This is an important result because, as shown next, capsule flux asymmetry depends most directly on quad-to-quad power imbalance.

Calculations of Radiation Asymmetry on a NIF Capsule

Here, we describe our calculations of the effects of random variations in laser power and pointing on radiation flux symmetry at the target. We estimated the sensitivity of capsule flux asymmetry to various amounts of power imbalance and pointing errors, and then used our results from the detailed laser model, described above, to estimate the expected capsule flux asymmetry during the foot and peak of a shaped, indirect-drive pulse.

Calculating the Random Component of Radiation Flux on a Capsule

We used the radiation viewfactor code, Gertie,[5] to estimate the flux on a capsule. The geometry of the hohlraum and capsule are the primary inputs to the code. The surfaces of each are divided into a discrete number of area elements A_i. Each element has an albedo α_i, which is the ratio of emitted radiation over absorbed radiation, averaged over all frequencies and angles. In addition, surface elements on the hohlraum wall that correspond to laser hot spots are given a source power P_i. Radiation power leaving the ith element y_i, and radiation power arriving at that element x_i, are related to each other by

$$y_i = \alpha_i x_i + P_i \tag{9a}$$

and

$$x_i = \sum_j f_{ij} y_j \ , \tag{9b}$$

where f_{ij} is the geometric viewfactor matrix constructed by Gertie. Thus, once the geometry, albedos, and radiation sources are defined, the matrix equations can be solved to obtain the radiation flux incident on the capsule (and on all other surfaces as well). The viewfactor analysis has two principal limitations. Sources and albedos are not frequency-dependent, and there is no absorption and emission of radiation by the plasma inside the hohlraum (i.e., vacuum transfer is assumed between the walls and capsule). However, the technique does provide an estimate of the 3D variation of flux on the capsule.

Viewfactor calculations were done for the point-design target[6] (PT design), which is shown in Figure 13. This target has a 0.111-cm radius and uses a Br-doped plastic ablator. It is driven by a 1.3-MJ, 17-ns pulse, shown in Figure 14. This pulse is similar to the 1.8-MJ, NIF-baseline pulse shown earlier; however, the foot is about 3-ns shorter, and the peak power and energy are

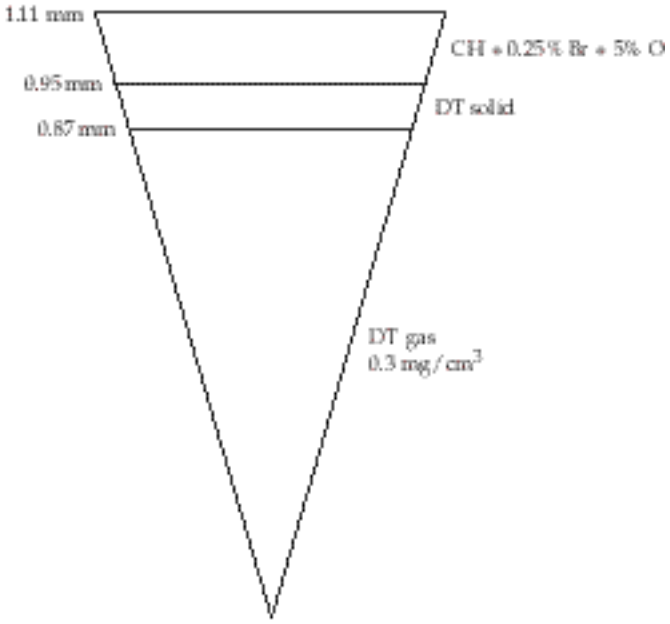

FIGURE 13. The PT design features a Br-doped plastic ablator and has an initial radius of 0.111 cm. (50-00-1298-2557pb01)

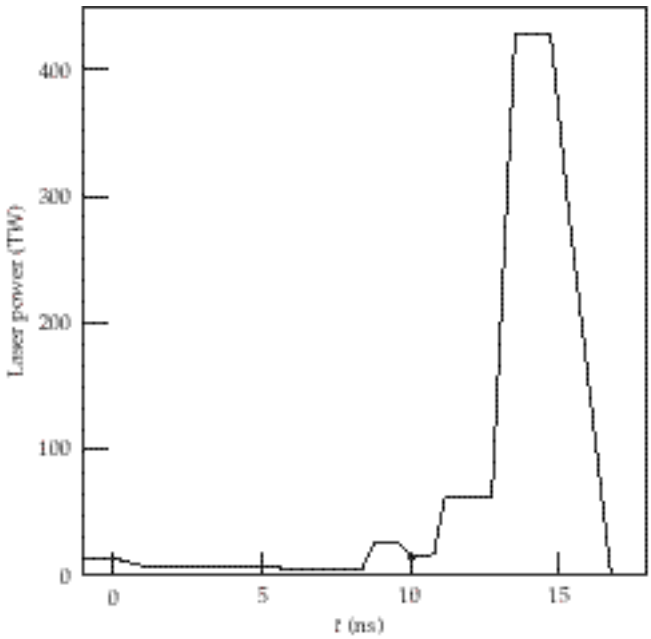

FIGURE 14. The PT is driven by a 17-ns, 1.3-MJ, shaped pulse. (50-00-1298-2558pb01)

less. From radiation-hydrodynamics calculations of the PT design using LASNEX,[7,8] we inferred the time dependence of the capsule and hohlraum albedos, the capsule ablation surface radius, and the hohlraum emission radius (which moves in as gold blows off the wall).

The albedo of the gold wall is greater than that of the plastic ablator, and both increase as radiation temperature rises during the pulse. As the albedo increases, a smaller fraction of total radiation emanates from the laser hot spots, and the radiation is spatially smoothed. In addition, as the hohlraum emission radius and capsule ablation surface radius both decrease with time, the viewfactor matrix that maps the hohlraum radiation onto the capsule also changes. Late in the pulse, as the capsule ablation surface radius decreases rapidly, each point on the capsule sees a larger fraction of the hohlraum wall; therefore, higher wave number components of the radiation asymmetry on the hohlraum are smoothed at the capsule.

In principle, we could divide the pulse into a few time steps and do a viewfactor calculation at each time to obtain the time-dependent flux on the capsule. However, we found it more practical to divide the pulse into two parts. We defined the foot to be the first 11 ns, and the peak to be the remainder of the pulse. We then did the viewfactor analysis midway through the foot and midway through the peak, using average values for the albedos and dimensions shown in Table 3. We subdivided the capsule and hohlraum surfaces into 3,840 subpanels, with 32 panels per 360° of azimuthal angle.

TABLE 3. Geometric parameters and albedos used in the viewfactor calculations of the foot (t = 0 to 11 ns) and peak (t = 11 to 17 ns).

Parameter	Foot	Peak
Hohlraum albedo	0.65	0.86
Capsule albedo	0.35	0.63
Hohlraum radius	0.27 cm	0.234 cm
Hohlraum length	1.0 cm	0.95 cm
LEH radius	0.135 cm	0.117 cm
Capsule radius	0.111 cm	0.085 cm

Estimating Capsule Perturbation Resulting from Radiation Asymmetry

If we denote the radiation on a capsule as F, then rms flux asymmetry at the capsule is

$$cap_{\mathrm{rms}} = \sqrt{\frac{1}{4\pi}\int\left(\frac{F-F_0}{F_0}\right)^2 d\Omega} \quad . \tag{10}$$

The flux can be expanded, in terms of associated Legendre polynomials, as

$$F(\theta,\phi) = \sum_{l=0} b_{l0} P_l^0 + \sum_{l=1}\sum_{m=l}^{l} 2b_{lm} P_l^m \times \cos m\phi$$

$$-\sum_{l=1}\sum_{m=-l}^{l} 2b_{lm} P_l^m \sin m\phi \quad . \tag{11}$$

This form of the expansion is the same as that computed by the Gertie viewfactor code. By substituting Eq. (11) into Eq. (10) and including the appropriate normalization factors, we can express the rms flux asymmetry as the root of the sum of squares of contributions from each mode. That is, the capsule asymmetry is

$$cap_{\mathrm{rms}} = \sqrt{\sum_{l=1}\sum_{m=-l}^{l} \left(a_{lm}\right)^2} \ , \tag{12}$$

where

$$cap_{\mathrm{rms}} = \sqrt{\sum_{l=1}\sum_{m=-l}^{l} \left(a_{lm}\right)} \tag{13}$$

and

$$a_{lm} = \sqrt{\frac{2}{2l+1}\frac{(l-|m|)}{(l+|m|)}\left(\frac{b_{lm}}{b_{00}}\right)^2} \ . \tag{14}$$

For each l mode, we can sum the squares of the rms contributions for all m to obtain the rms for an equivalent 2D mode, which we denote as a_l.

Now that we have extracted the mode structure (rms per mode) of the equivalent 2D flux asymmetry from the viewfactor calculation, we can use LASNEX to calculate the spatial perturbation in the capsule radius at ignition due to each mode. As long as radiation-induced perturbations on the capsule remain linear, we can use the principle of superposition to equate the calculated 2D rms flux asymmetry at ignition to the rms flux asymmetry at ignition that results from linear growth of the original 3D spectrum of modes from the viewfactor calculation.

The linear response coefficients that relate a flux perturbation to spatial perturbation on the capsule for each mode were calculated in LASNEX by applying a frequency-dependent source to the capsule that had a small perturbation in each mode applied during the foot (0 to 11 ns) or peak (11 to 17 ns) of the pulse. These coefficients yield the capsule rms spatial asymmetry for the case where the 3D capsule flux asymmetry calculated at the midpoint of the foot or peak is present and unchanging for the entire foot or peak. This is a simplification of the actual situation, where the magnitude and mode structure of the capsule flux asymmetry change during the foot and peak.

NIF Illumination Geometry

Figure 15 shows the NIF indirect-drive geometry. Laser rays are shown from their focal points to the point at which they hit the hohlraum walls. Two cones, an outer and an inner cone, illuminate each side of the hohlraum. The outer cone is made of beams having angles of 44.5° and 50° with respect to the z (cylindrical) axis. The inner cone beams have angles of 23.5° and 30°. Two-thirds of the laser energy is directed to the outer cones, and one-third to the inner cones. Figure 15 also shows the target geometry that we assumed for this study. The hohlraum length is 1.0 cm, the hohlraum radius is 0.27 cm, laser entrance holes have a radius of 0.135 cm, and the initial capsule radius is 0.111 cm.

Spots from the four beams in a quad partially overlap on the hohlraum wall, forming one larger spot, as shown in Figure 16. Differences in power among the four beams in a quad cause a shift in the spot centroid and are equivalent to a pointing error in the quad spot. The distance from the centroid of the quad spot to centroids of each of the individual beam spots, r_j, is about 230 μm. The offset of the centroid of the quad spot, r_c, is related to beam power by

$$r_c = \sum_{j=1}^{4} \frac{r_j P_j}{P_{\mathrm{quad}}} \ , \tag{15}$$

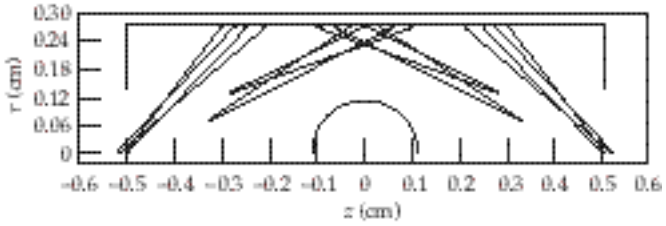

FIGURE 15. Side view of the hohlraum showing placement of inner and outer cones. (50-00-1298-2559pb01)

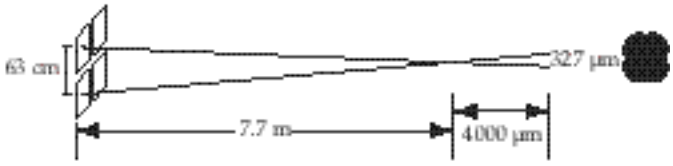

FIGURE 16. Four beams within a quad form a single, overlapped spot on the hohlraum. (50-00-1298-2560pb01)

where P_j is the power from the jth beam, and P_{quad} is the total quad power. Using Eq. (15), we can calculate that the 4% to 5% intraquad power imbalance, which was calculated previously in Figure 12, results in a 5- to 6-μm rms error in quad spot position.

Sensitivity of Ignition Capsule to Random Flux Asymmetry

Figure 17 shows the sensitivity of total rms capsule flux to the amount of quad-to-quad power imbalance using the viewfactors midway through the foot and peak of the pulse. These results were obtained by averaging over 10 sets of random power distributions that were generated using the statistical model of the NIF laser, discussed previously. We assumed that the viewfactor calculations done for a 17-ns pulse could be applied to the 20.4-ns Haan pulse. For the foot, we used BTGAIN results at t = 7 ns (midway through the 14-ns foot). For the peak, we used BTGAIN results at t = 17 ns (approximately midway through the peak). Figure 17 shows that, compared to the peak, the larger ratio of capsule radius to hohlraum radius for the foot, and the lower albedos in the foot, result in a larger amount of flux asymmetry. The average quad power imbalance during the foot of the Haan pulse is approximately 4%, and it is about 3% during the peak (see these two points as plotted in Figure 17). Thus, the resulting rms flux asymmetry due to power imbalance will be about 0.6% during the foot, and 0.2% during the peak. Note that rms flux asymmetry is plotted here as a function of the quad-to-quad imbalance, rather than beam-to-beam imbalance. As shown below, quad-to-quad imbalance can be generally related to asymmetry on the capsule, whereas beam-to-beam imbalance cannot.

The other contributor to random flux asymmetry is pointing errors. Figure 18 shows rms flux asymmetry on the capsule as a function of rms quad pointing error. The results were obtained by averaging over 50 random pointing configurations. By quad pointing error, we mean the deviation in the location of the quad centroid. The NIF specification for allowable beam-to-beam pointing errors is 50 μm rms. It is likely that there will be sources of pointing error that are common to beams within a quad; however, the breakdown between correlated and uncorrelated pointing errors has not been determined at this time.[9] If we assume that pointing errors are uncorrelated, then a 50-μm, beam-to-beam error corresponds to a 25-μm, quad-to-quad error, which leads to capsule flux asymmetry of about 0.4% during the foot, and less than 0.2% during the peak. Figures 17 and 18 are plotted on the same scale, and a comparison between them shows that power imbalance will generally have a larger effect on capsule flux asymmetry than will the pointing errors.

Recall from Eq. (12) that capsule flux rms asymmetry can be expressed as the root of the sum of squares of contributions from each associated Legendre polynomial. The square of the rms is called the variance. Thus, the variance per mode is a_{lm}^2, where a_{lm} is given by Eqs. (13) or (14). The variance per l mode, which is what we need to apply the 2D linear response coefficients calculated from LASNEX, is

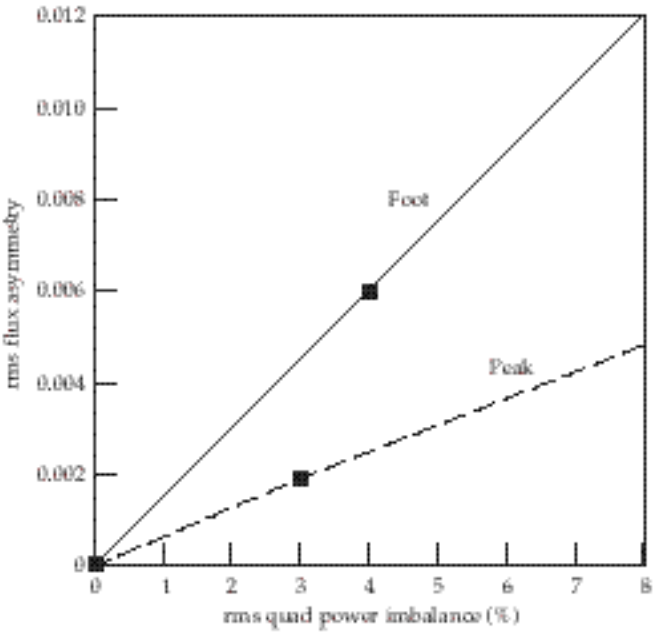

FIGURE 17. The rms capsule flux asymmetry as a function of amount of quad-to-quad power imbalance. (50-00-1298-2561pb01)

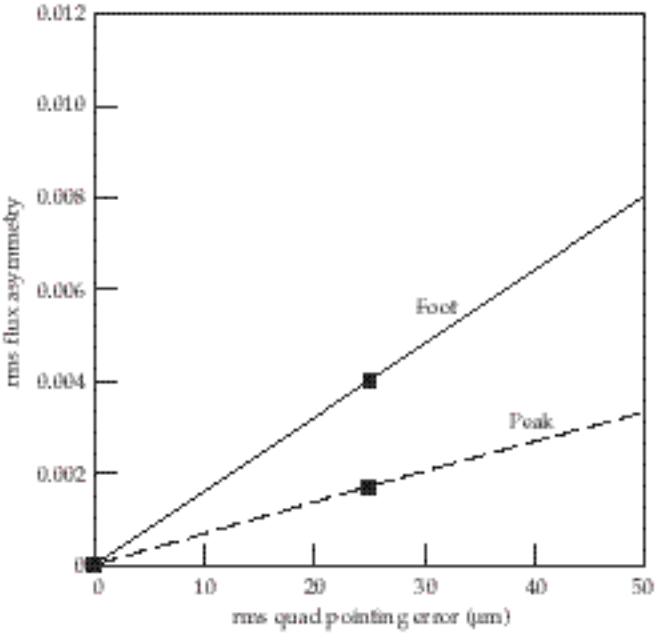

FIGURE 18. The rms capsule flux asymmetry as a function of quad-to-quad pointing errors. (50-00-1298-2562pb01)

$$a_l^2 = \sum_{m=-l}^{m=+l} a_{lm}^2 \quad . \tag{16}$$

The ratio of a_l^2 to total variance of capsule flux is plotted in Figure 19 as a function of l-mode number for power imbalance. For both the foot and peak, the largest contribution is from P_1, and there is little contribution from modes larger than $l = 4$. Figure 20 shows the modal decomposition for pointing errors. Similar to the power imbalance, the contribution to variance falls off rapidly with increasing mode number. However, the dominant mode is P_2, and there is a larger relative contribution from higher modes.

From the modal decomposition of flux asymmetry, we can find each mode's contribution to the capsule spatial asymmetry at ignition using the linear response coefficients obtained from LASNEX capsule calculations. The capsule spatial rms is given by

$$(\text{spatial})_{\text{rms}} = \sqrt{\sum_{l=1} \left[a_l (\text{lrc})_l \right]^2} \quad , \tag{17}$$

where $(\text{lrc})_l$ is the linear response coefficient relating capsule flux rms due to the lth mode to the spatial rms at ignition due to that mode. We multiply the spatial rms by 2 times the square root of 2 to convert the rms to the maximum difference in peak-to-valley (ptv) of the spatial variation. This parameter is plotted in Figure 21 as a function of percent rms quad power imbalance. Such a plot shows that the peak is slightly more sensitive to power imbalance than the foot, even though the capsule flux asymmetry is less for the peak. The shaded portion of the plot (6-µm ptv perturbation or less) represents the level of capsule perturbations arising from random asymmetry that is definitely

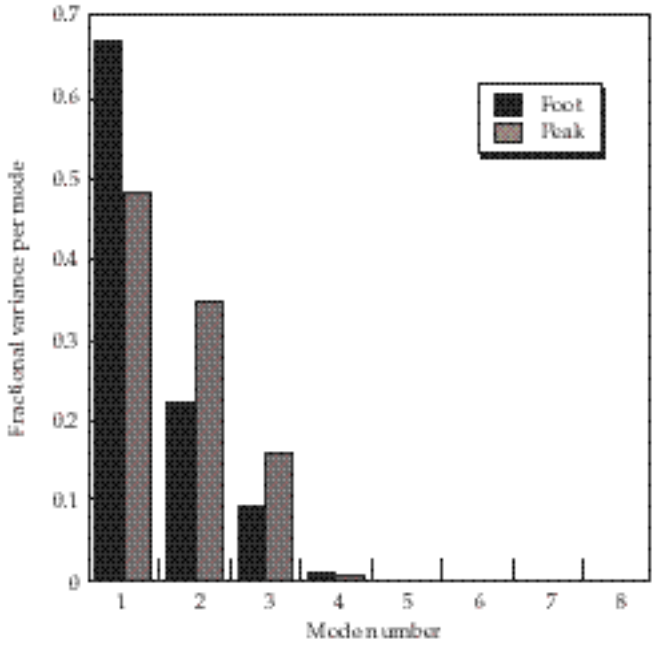

FIGURE 19. Fractional contribution of each Legendre mode to total variance of the capsule flux due to power imbalance.
(50-00-1298-2563pb01)

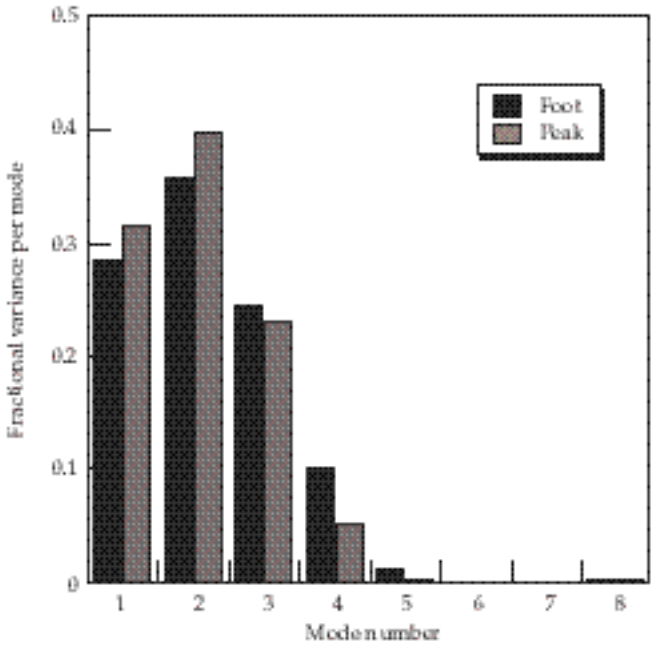

FIGURE 20. Fractional contribution of each Legendre mode to total variance of the capsule flux due to beam pointing errors.
(50-00-1298-2564pb01)

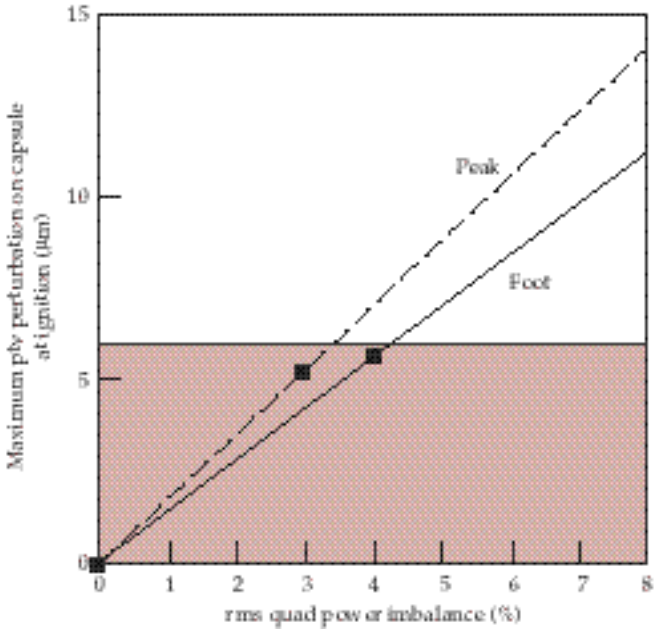

FIGURE 21. Maximum peak-to-valley perturbation in hot-spot radius at ignition as a function of percent rms quad power imbalance.
(50-00-1298-2565pb01)

safe.[10] Thus, the time-averaged quad power imbalance must remain well below 8% to keep the resulting spatial perturbations in the safe regime. At the power imbalance levels extracted from BTGAIN calculations (see data points), power imbalance only during the foot results in a 5.6-μm ptv perturbation, whereas power imbalance only during the peak results in a 5.2-μm ptv perturbation.

Figure 22 is a similar plot, but for pointing errors. It shows that if the pointing errors are uncorrelated, resulting in 25-μm rms quad-to-quad pointing error, then pointing errors make a slightly smaller contribution to the total capsule spatial perturbation at ignition (5.1 versus 4.3-μm ptv for the foot versus peak, respectively).

Figure 23 shows the fractional contribution of each mode to total variance (the square of the rms) of spatial asymmetry on the capsule. For the foot, P_1 and P_2 are the largest contributors, whereas for the peak, P_1 is by far the largest. In fact, it is primarily the much larger linear response factor for P_1 in the peak, compared with that of the foot, that makes the overall capsule rms larger for the peak, despite the fact that rms flux asymmetry is less for the peak due to hohlraum smoothing. Figure 24 is a similar plot for pointing errors. Pointing errors during the foot give rise mainly to modes P_2 through P_4 on the capsule surface at ignition, whereas pointing errors during the peak contribute mostly to P_1 on the capsule. The combined effects of power imbalance predicted by the BTGAIN model and 25-μm rms quad pointing errors result in a capsule spatial perturbation of 7.5-μm ptv for asymmetry imposed during the foot only, and 6.7-μm ptv for asymmetry imposed during the peak only.

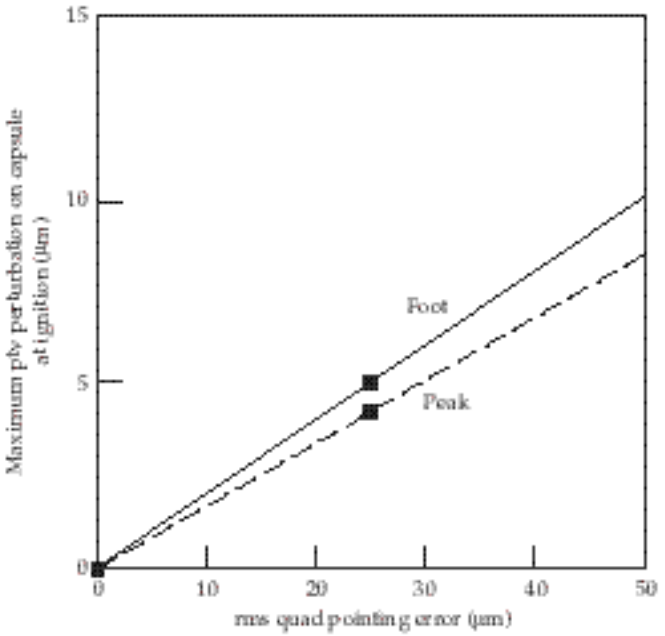

FIGURE 22. Maximum peak-to-valley perturbation in hot-spot radius at ignition as a function of percent rms quad pointing error. (50-00-1298-2566pb01)

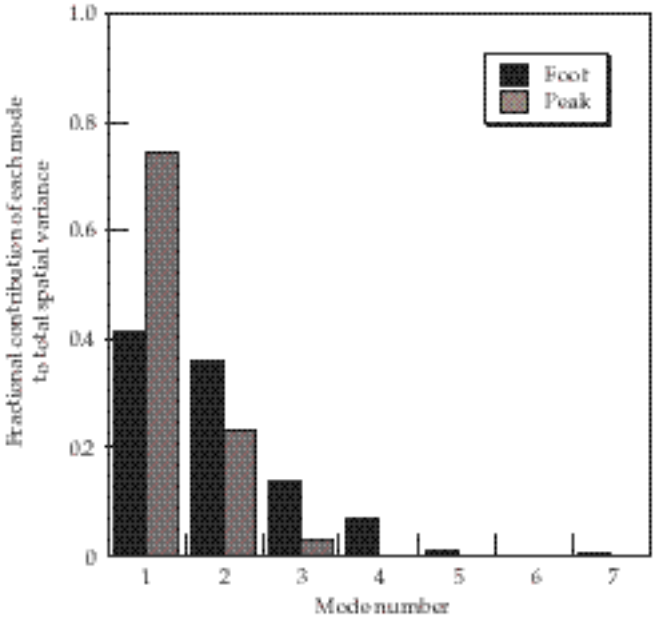

FIGURE 23. Fractional contribution of each Legendre mode to total variance of the hot-spot radius at ignition due to quad power imbalance. (50-00-1298-2567pb01)

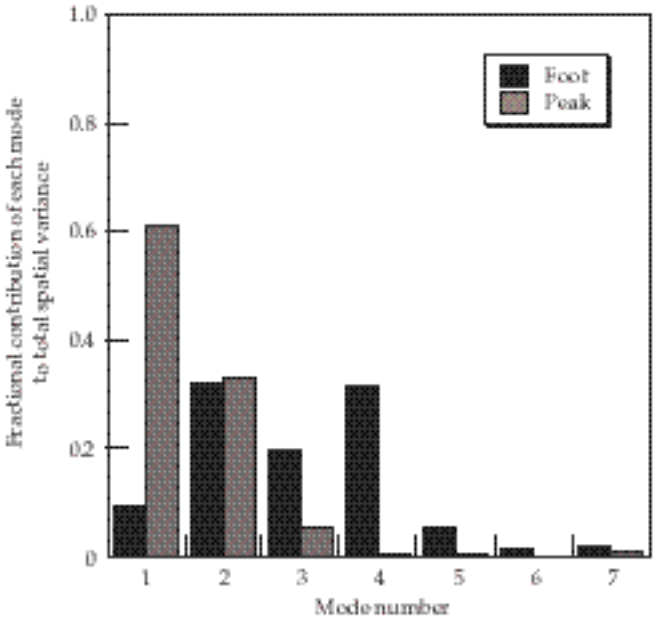

FIGURE 24. Fractional contribution of each Legendre mode to total variance of the hot-spot radius at ignition due to quad pointing errors. (50-00-1298-2568pb01)

Effect of Correlations on Power Balance

The powers to each of the 192 spots are not statistically independent. As discussed in the previous section, beams in a quad are driven by a common PAM, so the portion of the power imbalance arising from

jitter in the PAMs will be correlated for beams in the same quad. There is also a correlation between pairs of quads whose amplifiers are driven by common capacitor banks (such pairs of quads are called bundles), so jitter in amplifier gain will be correlated between bundles. Figure 25 is a schematic drawing of the overlapped quad spots on one-quarter of an unrolled hohlraum cylinder. The shading and numbers on the spots indicate which quads are driven by common capacitor banks. Correlated spots are separated from each other spatially in a pseudo-random pattern. The pattern repeats itself in the next quadrant. For the two remaining quadrants ($\pi < \phi < 2\pi$) the relation between bundles 5 and 6 is reversed.

The idea behind bundle mapping is to ensure that neighboring quads are not correlated; if they were, statistically they would behave like a single spot. This would increase the power imbalance due to the amplifier gain jitter by reducing the number of independent spots from 48 to 24.

To assess possible effects of correlations between beams on the power imbalance, we computed the power imbalance for three extreme cases:

Case 1. 192 independent beams.
Case 2. 48 independent quads, with the 4 beams within each quad correlated.
Case 3. 24 independent bundles, with the 8 beams within each bundle correlated.

The calculations were all done for the foot of the pulse. Figure 26 shows that the rms capsule flux asymmetry is about the same for a given amount of quad-to-quad power imbalance, regardless of how the power is correlated among the beams. This result indicates that quads in the same bundle are mapped to the hohlraum in a way that does not degrade capsule symmetry, even if all of the power imbalance were correlated for beams in the same bundle. Figure 27 shows the contribution of each mode to total spatial variance on the capsule at ignition. The modal structure is also fairly similar for the three cases. This result implies that the most important parameter needed to estimate capsule asymmetry due to power imbalance is an accurate estimate of quad-to-quad power imbalance. Knowing the fraction of quad-to-quad imbalance from beam-, quad-, and bundle-driven power imbalance is less important.

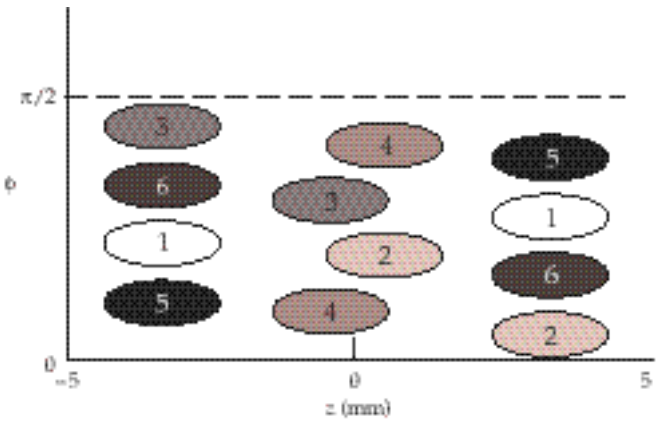

FIGURE 25. One-quarter of a hohlraum cylinder unrolled to show the approximate arrangement of overlapped quad spots on the hohlraum and the relative locations of quads sharing capacitor banks. (50-00-1298-2569pb01)

Summary

We have developed a model to analyze power balance for the NIF. Our model includes the effects of laser gain saturation and frequency-conversion intensity dependence. Statistical variation in component performance was included to account for systematic and random variations in the power output of each beam. We found that the effects of gain saturation, which tends to reduce power imbalance late in the pulse, and the strong intensity dependence of frequency conversion at low intensity early in the pulse, combine to make the power imbalance largest at the beginning of shaped, indirect-drive pulses. We then used the model to determine the allocation of random variations to subsystems and to develop procedures for minimizing repeatable differences among beams. The results of our power balance analysis indicate that we can meet the NIF 8% rms power balance requirement for a 1.8-MJ, indirect-drive pulse. To minimize

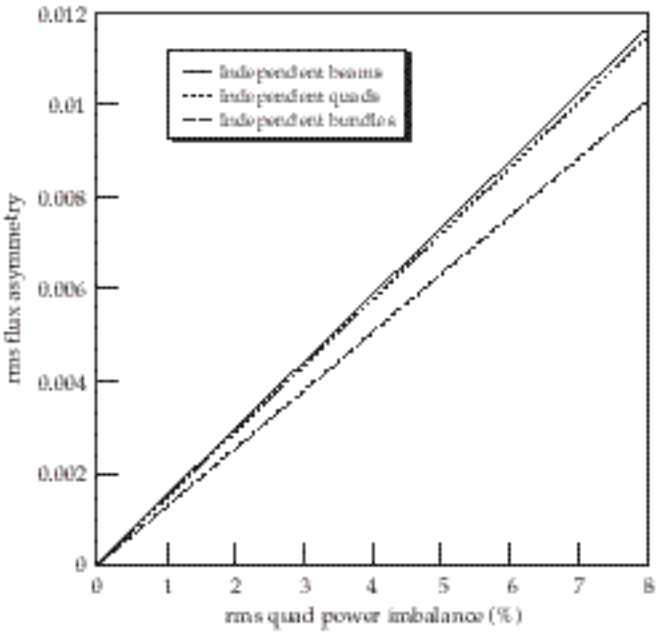

FIGURE 26. The rms capsule flux asymmetry in the foot as a function of rms quad power imbalance for 192 independent (uncorrelated) beams, 48 independent quads with all 4 beams in each quad correlated, and 24 independent bundles with all 8 beams in each bundle correlated. (50-00-1298-2570pb01)

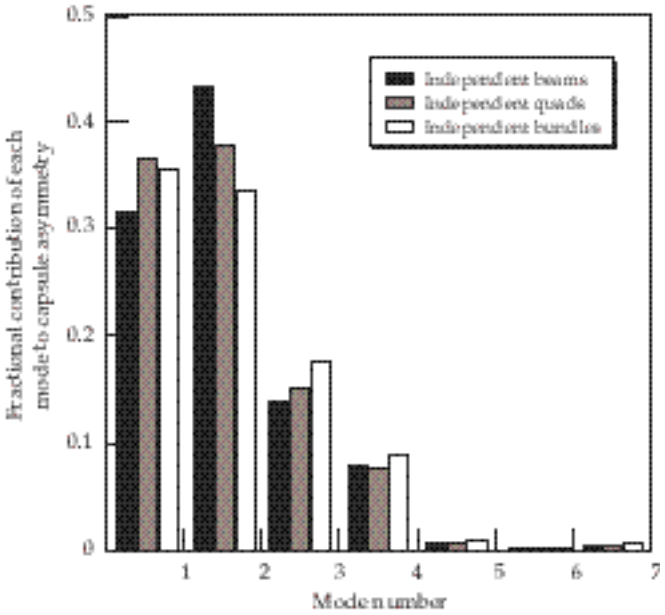

FIGURE 27. Fractional contribution of each Legendre mode to total variance of the hot-spot radius at ignition for power imbalance in the foot due to 192 independent beams, 48 independent quads with all 4 beams in each quad correlated, and 24 independent bundles with all 8 beams in each bundle correlated. (50-00-1298-2571pb01)

the systematic imbalance, we use a single-input pulse shape, but adjust the energy to each beam to minimize the repeatable power imbalance at $t = 1$ ns.

We also performed a radiation viewfactor analysis to determine the effect of various levels of random flux asymmetry on ignition capsule performance. The capsule rms flux asymmetry is larger—for a given level of imposed power imbalance or pointing errors—during the foot of the pulse than during the peak. The reason is that lower albedos and larger capsule-radius-to-hohlraum-radius ratio lead to less smoothing of the Legendre modes onto the capsule. However, the capsule is more sensitive to the P_1 mode during the peak. Thus, the resulting spatial perturbation on the capsule at ignition is about the same for radiation asymmetry imposed during the foot or peak. Power imbalances contribute slightly more to the total capsule perturbation at ignition than do pointing errors.

The fraction of power imbalance that is correlated for beams within the same quad is very important, because flux asymmetry on the capsule is twice as large for fully correlated beams than for fully uncorrelated beams. Our NIF laser modeling indicates that power imbalance is highly correlated early in the pulse when the power imbalance is dominated by OPG and amplifier jitter. By the end of the pulse, the largest sources of power imbalance (random variations in timing and frequency conversion, and all systematic variations) are mostly uncorrelated, which reduces the effect on the capsule. The fraction of power imbalance that is correlated between quads whose amplifiers are driven by common capacitor banks was found to be a minor effect.

Integrated viewfactor simulations that assumed a level of 50-μm rms uncorrelated pointing errors and a level of power imbalance extracted directly from the statistical NIF laser model indicate maximum peak-to-valley perturbations on the hot-spot radius at ignition of 7.5 μm due to random flux asymmetry applied only during the foot of the pulse, and 6.7 μm due to random flux asymmetry applied only during the peak of the pulse. These values are close to the maximum amount of capsule perturbation allocated to random flux asymmetry.

Acknowledgments

We thank Clay Widmayer and Paul Renard for helping to set up the BTGAIN simulations. Thanks to Jerry Auerbach for providing the frequency-conversion performance code THGFT02. Thanks to Wade Williams and Ken Manes for helpful discussions regarding laser performance.

Notes and References

1. L. Powers and L. J. Suter, Lawrence Livermore National Laboratory, Livermore, CA, private communication (1991).
2. J. B. Trenholme, "Theory of Irregularity Growth on Laser Beams," *1975 Laser Annual Report*, Lawrence Livermore National Laboratory, Livermore, CA, UCRL-50021-75 (1975).
3. L. M. Frantz and J. S. Nodvik, *J. Applied Physics* **14**(8) (1963).
4. J. Auerbach, Lawrence Livermore National Laboratory, Livermore, CA, memorandum NIF-LLNL-94-516 (1994).
5. G. B. Zimmerman wrote Gertie. The user interface was written by D. H. Munro. The viewfactor subroutine was written by R. Kirkpatrick and modified by D. S. Bailey.
6. S. W. Hann et al., *Phys. Plasmas* **2**(6), 2480–2487 (1995).
7. G. B. Zimmerman and W. B. Kruer, *Comments Plasma Phys. Control. Fusion* **2**, 85 (1975).
8. J. A. Harte et al., *ICF Quarterly Report* **6**(4), 150–164, Lawrence Livermore National Laboratory, Livermore, CA, UCRL-LR-105821-96-4 (1996).
9. S. Sommer, Lawrence Livermore National Laboratory, Livermore, CA, private communication (1998).
10. S. W. Haan, Lawrence Livermore National Laboratory, Livermore, CA, private communication (1997).

CALCULATING AND MEASURING THE EFFECTS OF POLARIZATION SMOOTHING ON SCATTERING INSTABILITIES IN A NIF-LIKE PLASMA

J. D. Moody

R. L. Berger

J. E. Rothenberg

Introduction

The present schemes for inertial-confinement-fusion (ICF) target ignition require a high uniformity in the intense laser beams that will strike the target directly (direct drive) or the hohlraum wall (indirect drive).[1] The large-aperture glass laser systems used in ICF applications produce beams with nonuniform intensity speckle structures ("hot spots") at their focus. With intensities that are significantly above the spatial average beam intensity, these hot spots can lead to substantial power losses from stimulated Raman scattering (SRS) and stimulated Brillouin scattering (SBS) in hohlraum plasmas. To reduce these scattering losses, various beam-smoothing techniques have been developed to create more uniform beam intensity distributions.[2–11]

As part of a plan for attaining ignition at the National Ignition Facility (NIF), we used the Nova laser system to systematically study the effectiveness of the beam-smoothing techniques in reducing the backscattered light. Previously, experiments examined the effects of random phase plates (RPPs),[3] kinoform phase plates (KPPs),[10] and smoothing by spectral dispersion (SSD)[4] using a 3-GHz modulator.[11] Under various laser and plasma conditions, these techniques all showed certain advantages with respect to reducing the backscattered light level.

Most recently, we studied the effect of polarization smoothing (PS)[6–9] by itself and combined with smoothing by spectral dispersion, using a high-frequency (17-GHz) modulator. The higher frequency modulator reduces the beam dispersion necessary for optimal SSD, thereby allowing laser propagation through spatial-filter pinholes and hohlraum entrance holes without clipping.[12] This article describes the predicted and measured effects of polarization smoothing (with and without smoothing by spectral dispersion) on the stimulated Raman and Brillouin backscattering. Both the experimental work and the modeling show that the combination of polarization smoothing with smoothing by spectral dispersion gives the greatest reduction in the backscattering levels for SRS and SBS.

Relevance to NIF

Target designs for the NIF currently consist of gas-filled, 9-mm long, Au hohlraums that will be heated with a 1.3-MJ (430-TW peak power) laser, at a 351-nm wavelength.[13] The laser energy will be delivered to the hohlraum by 192 beams in shaped pulses about 20 ns long. The beams will be focused with $f/20$ lenses arranged in clusters of four, effectively producing an $f/8$ beam. For symmetric capsule implosions, two rings each of inner and outer beams will be used, which reach the hohlraum wall at different distances from the laser entrance holes (LEHs) and have different path lengths in the hohlraum plasma.

Beam smoothing will be done by using spectral dispersion with a kinoform phase plate. This phase plate will produce a flat-top focal spot with a factor-of-two intensity variation over the 3- to 5-mm-long laser path in the hohlraum. The point design ignition target[13] is a 300-eV radiation temperature hohlraum, which will contain a low-Z, fully ionized plasma (initially a mix of He and H_2) at about 10% of the critical density. At the time of maximum laser power, the peak laser intensity will be 2×10^{15} W/cm^2 at the best focus of the $f/8$ cluster; other regions along the beam path will have intensities ranging from 10^{15} to 2×10^{15} W/cm^2. Over most of their path lengths, the laser beams will interact with the low-Z plasma. However, for the last 400 μm, the interaction will be with a high-Z, high-T_e Au plasma ablated from the hohlraum wall. The low-Z plasma between the hohlraum wall and the laser entrance holes will have an electron temperature T_e ranging from 3- to 6-keV, and an electron density n_e of from 0.07 n_c to 0.12 n_c ($n_c = 9 \times 10^{21}$/cm^3 for 351-nm light).

We have done calculations and experiments studying the effects of smoothing by spectral dispersion and polarization smoothing in various combinations—with plasma conditions and at length scales that are relevant to NIF. The two NIF plasma conditions that are important to emulate are (1) a long-scale-length (2-mm), low-*Z* plasma (with a high-gain exponent for stimulated Brillouin and Raman scattering) that the inner-beams encounter and (2) a shorter-scale-length, outer-beam plasma, corresponding to the plasma conditions near the Au wall[14] (with a higher-gain exponent for stimulated Brillouin scattering).
We modeled the low-*Z*, inner-beam case experimentally with gasbag targets. The NIF's outer-beam plasma was modeled with a scale-1 hohlraum described in a separate article.[15]

Polarization Smoothing: Optical Theory and Experimental Implementation on Nova

Spatial smoothing using a random phase plate works by eliminating the long coherence length in a beam's near field, thereby randomizing and reducing the high-intensity, small-scale structure within the focal spot. A similar kind of spatial smoothing uses a kinoform phase plate, which produces a speckle distribution of intensities in the far field—as does the random phase plate—but which makes the average intensity at focus spatially flat. Smoothing by spectral dispersion causes the local speckle intensity (produced by either type of phase plate) to vary in time at a given spatial location. The laser light is first broadened in frequency by $\Delta\nu$ using frequency modulation (FM) and then it is dispersed with a grating. At any time, the resulting speckle pattern is a superposition of interfering patterns from each wavelength, which decorrelate and yield a new speckle pattern with a coherence time of $\sim 1/\Delta\nu$. Practical limitations in the available laser bandwidth will typically limit the coherence time to a few picoseconds. This is a short enough time to possibly affect the filamentation instability. However, since the scattering instabilities in ICF plasmas typically develop in less than a picosecond, it is also desirable to employ a technique that can smooth out intensity non-uniformities instantaneously. Polarization smoothing provides a way of doing just this.

In polarization smoothing, the near field of the incident laser light is divided into two orthogonal polarizations, each containing half of the beam's incident power. By passing these beams through a phase plate, two uncorrelated speckle patterns are produced, with each beam generating a distinct speckle pattern in the focal plane. One technique used for polarization smoothing is to alternately rotate the polarization by 90° in subapertures of the near-field beam.[7,8] The technique that we chose for Nova uses a birefringent wedge to create orthogonally polarized beams in the same subaperture of the near-field beam.[6] The wedge creates a spatial offset in the speckle patterns corresponding to the two polarizations. In either technique, the speckle intensities in the two beams add incoherently, thus reducing the maximum intensities arriving at the focal plane. The essential advantage of polarization smoothing is that the light intensity is smoothed instantaneously, whereas smoothing by spectral dispersion requires a smoothing time that is inversely proportional to the laser bandwidth.

In polarization smoothing by a wedge, the primary adjustable parameter is the size of the shift generated between the orthogonal speckle patterns. Recent calculations have shown that supression of filamentation is fully effective when PS is used with a minimum shift of one to two speckle half-widths.[9] Since plasma filamentation and stimulated scattering instabilities are generally very sensitive to the transverse scale length of the incident illumination, it is useful to consider the spatial spectrum of the focal-spot intensity pattern resulting from the polarization smoothing of simple square-aperture beams. (Although the spectrum changes slightly in going from square to circular apertures, the qualitative features remain the same.)

The effect of the polarization-smoothing shift on the intensity distribution in the focal plane is best understood in terms of its effect on the spatial spectrum of the speckle intensity. We begin by writing down the spatial power spectral density of the speckle intensity from a uniformly illuminated (but randomly phased) square aperture as:[16]

$$\frac{\left|\tilde{I}(f_x, f_y)\right|^2}{\tilde{I}^2} = \Lambda(f_x / f_{\max})\Lambda(f_y / f_{\max}) \Big/ f_{\max}^2 + \delta(f_x, f_y) \quad . (1)$$

In this expression, $f_x(k_x/2\pi)$ and $f_y(k_y/2\pi)$ are spatial frequencies of the speckle in the far field, $\Lambda(x) \equiv 1 - |x|$ for $|x| \le 1$, and 0 for $|x| > 1$, $f_{\max} \equiv D/F\lambda$ (where F is the focal length of the lens and D is the aperture width), $\tilde{I}(f_x, f_y)$ is the Fourier transform of the speckle intensity in the far field $I(x_{FF}, y_{FF})$, and $\tilde{I} \equiv \left\langle I(x_{FF}, y_{FF}) \right\rangle$ denotes the average speckle intensity. The first term on the right of Eq. (1) corresponds to the speckle noise and is referred to as the AC spatial-power spectrum; the delta function is determined by the average intensity level.

The spatial power spectrum of the far-field intensity pattern for the two spatially offset speckle patterns, created by the birefringent wedge, can now be quantified. Let the speckle pattern from a single polarization be given by $I_1(x_{FF}, y_{FF})$. Assuming that the wedge disperses the two polarizations by an angle $\Delta\theta$ along the x direction, its effect is to generate two such patterns shifted along x by the distance $\Delta x_{FF} = \Delta\theta F$. Because

there is no interference between the orthogonal polarizations, the total intensity on the target can be written as the incoherent sum

$$I_{\text{total}}(x_{\text{FF}}, y_{\text{FF}}) = I_1(x_{\text{FF}}, y_{\text{FF}}) + I_1(x_{\text{FF}} + \Delta x_{\text{FF}}, y_{\text{FF}}) = I_1(x_{\text{FF}}, y_{\text{FF}}) * \left[\delta(x_{\text{FF}}) + \delta(x_{\text{FF}} - \Delta x_{\text{FF}})\right], \quad (2)$$

where * denotes convolution $\left[a(x) * b(x) \equiv \int a(x-s)b(s)ds\right]$. The Fourier transform can now be taken, to obtain the spatial power spectrum of the total intensity distribution

$$\frac{\left|\tilde{I}_{\text{AC,total}}(f_x, f_y)\right|^2}{\bar{I}_{\text{total}}^2} = 4\left|\tilde{I}_1(f_x, f_y)\right|^2 \cos^2(\pi \Delta x_{\text{FF}} \bullet f_x) \,/\, 4\bar{I}_1^2 = \Lambda(f_x)\Lambda(f_y)\cos^2(\pi \Delta x_{\text{FF}} \bullet f_x) / f_{\max}^2 . \quad (3)$$

where the single polarization result of Eq. (1) has been used.

We have now obtained the result that the wedge modifies the spatial spectrum by imposing a sinusoidal modulation, along the shift direction, with a period of $1/\Delta x_{\text{FF}}$. Smoothing very low spatial frequencies requires a large shift, since the first null of the spectral modulation imposed by the polarization smoothing is located at $\pm 1/2\Delta x_{\text{FF}}$. On average, for any shift larger than the speckle half-width $F\lambda/D$, the speckle noise power is reduced by a factor of two; thus, the intensity contrast is reduced by $\sqrt{2}$. This is consistent with simulations of plasma filamentation, which showed that suppression of the instability is fully effective only if the shift is larger than $F\lambda/D$.

The polarization smoothing done in our Nova experiments used a birefringent wedge[6] (a KDP crystal cut at an angle of 41.2° to the optic axis) to create two orthogonally polarized beams with a selected angular deviation (Figure 1). An equal distribution of the incident laser power into each polarization was accomplished by orienting the crystal wedge so that the linearly polarized 351-nm beam (from the frequency-conversion crystals) is incident with its polarization at a 45° angle to the KDP wedge's ordinary (o-wave) and extraordinary (e-wave) axes. The wedge causes the polarizations to be refracted into two beams, separated by an angle, $\Delta\theta = a\Delta n$, where a is the wedge angle and Δn is the birefringence between the ordinary and extraordinary polarizations (0.021 for the KDP used in this experiment).

After passing through the kinoform phase plate (KPP), the two orthogonally polarized beams form identical speckle patterns in the focal plane that are shifted by the amount, $\Delta\theta \cdot F$, where the focal length F is 5.6 m. The minimum shift required to decorrelate a speckle pattern generated by a square near-field beam is the half-speckle width, $F\lambda/D$ = 3.2 μm; the incident Nova beam width D was 62 cm.[17] The KDP crystals used for polarization smoothing in our experiments had a wedge angle of 270 μrad. Therefore, they generated an angular shift of 5.7 μrad between the orthogonally polarized beams, which corresponded to about a 30-μm far-field displacement, or about 10 speckle half-widths. This is much larger than the minimum shift of one to two speckle half-widths that was calculated as being required for suppressing filamentation.[9]

In our Nova experiments, we used four subapertures in a 2×2 array, similar to the NIF configuration; each subaperture was 27×27 cm and was separated by ~8 cm. The half-speckle width from one such subaperture was 7.3 μm; the polarization smoothing shift of 30 μm that resulted is about four times larger than the minimum shift needed to decorrelate the speckle originating from one subaperture. Thus, even for illumination from a single subaperture, filamentation would be effectively suppressed by the 30-μm wedge shift. The direction of the spatial shift from the polarization smoothing was arranged approximately orthogonally to the direction of the shift from SSD. Done in this manner, the polarization smoothing is expected to instantly improve the averaged contrast of the target illumination by a factor of $\sqrt{2}$ beyond that done only with SSD.

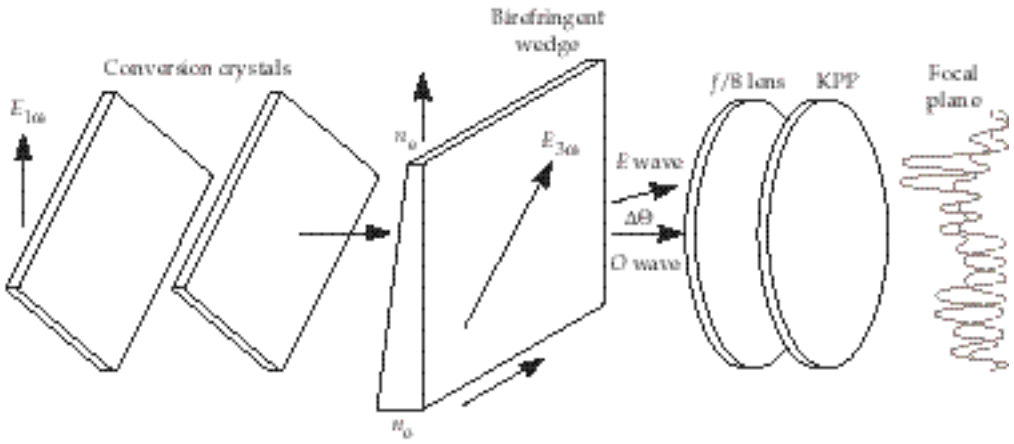

FIGURE 1. Schematic showing the use of a birefringent wedge to generate two shifted and orthogonally polarized speckle patterns for beam smoothing. (08-00-1298-2535pb01)

Polarization smoothing and smoothing by spectral dispersion can be combined to give a more effective smoothing, even though a range of low spatial frequencies is left unsmoothed by this combination. In our experiments, the full extent of the shift obtained with SSD is ~40 μm / Å of bandwidth (specified at the fundamental 1.053-μm wavelength). At a bandwidth of 3 Å, the resulting 120-μm shift is much larger than the 30-μm shift used for polarization smoothing. As a result, if the direction of the latter shift is parallel to the direction of spectral dispersion, little extra benefit might be expected from the added polarization smoothing.

However, because polarization smoothing is instantaneous, it is possible that a significant additional benefit from this method exists for some initial period of time (depending on the response time of the plasma instabilities), even for the case of parallel dispersion directions. This reasoning is supported by simulations of plasma filamentation, which found that SSD and PS dispersions oriented in the same direction work nearly as well at suppressing filamentation as do orthogonally oriented dispersions. However, we did not test this calculation in this set of experiments.[9]

Plasma Theory

The backscattering of laser light begins when a background plasma density fluctuation reflects a small fraction of the incident laser light via Thomson scattering. As the backscattered light interferes constructively with the incoming light, the resulting ponderomotive force enhances the density perturbation. If threshold conditions are satisfied, an instability, resulting in stimulated backscatter, can develop. If the density perturbation is an ion acoustic wave, stimulated Brillouin scattering (SBS) occurs; if the perturbation is a Langmuir wave, stimulated Raman scattering (SRS) occurs.

The laser speckles (hots pots) are also subject to a self-focusing instability (filamentation) in the plasma. This occurs when the light's ponderomotive force and the increased electron pressure (from local laser power absorption) act to expel plasma, thereby increasing the refractive index and further concentrating the light energy into a smaller volume. Smoothing by spectral dispersion reduces this tendency towards filamentation, if the speckle dissolves before the self-focusing process is complete. Thus, it is most effective on lower-intensity hot spots. In addition, polarization smoothing controls filamentation by reducing the fraction of the laser power present in high-intensity speckles. We expect then, that a combination of the two smoothing methods should be very effective for filamentation control.

Because the background density fluctuations tend to be very small, the mean intensity of the backscattered light must grow by about 10 orders of magnitude to scatter a significant portion (such as 10%) of the laser light. In contrast to this, a self-focusing amplification (resulting from filamentation) of as little as 2.7 times is dramatic. This is because, with a typical hot spot having an intensity twice that of the mean intensity, a great deal of laser energy can be transferred to high intensity and subsequently backscattered.

It appears that a bandwidth sufficient to reduce filamentation might also reduce the faster-growing stimulated Brillouin scattering, if the laser hot spot dissolves before the scattered light fully amplifies. The growth rate for stimulated Brillouin scattering exceeds that for filamentation, but is almost an order of magnitude smaller than for stimulated Raman scattering. The latter will grow to saturation in a few picoseconds for laser and plasma parameters that are of interest to ICF, long before smoothing by spectral dispersion can change the speckle pattern. On the other hand, polarization smoothing is instantaneous and it will reduce both stimulated Raman scattering (to the extent that SRS relies on higher-intensity speckles) and the stimulated Brillouin scattering.

The arguments just given for the effect of polarization smoothing considered each instability in isolation. Actually, the stimulated Raman and Brillouin scatterings, and filamentation instabilities, all interact with one another, leading to a complex beam-smoothing response. We used the F3D code[18] to simulate beam-smoothing effects on interacting stimulated Raman and Brillouin scatterings.[19] Filamentation was included in all cases. The plasma parameters that were chosen in the first simulations are representative of the NIF inner beams (n_e / n_c = 0.1; low-Z; combination of C_3H_8 and C_5H_{12}; T_e = 3 keV; T_i / T_e = 0.15; 2×10^{15} W / cm^2). The plasma length along the laser propagation direction (L_z = $1000\lambda_0$) is twice the length of the $f/8$ speckle; the plasma width in the x and y transverse directions is $160\lambda_0$. The intensity-gain exponents for the stimulated Raman and Brillouin scatterings are 12 and 9, respectively. These values are about one-half of those calculated for NIF and for the gasbag experiments reported in this article, primarily because of the shorter plasma length used in the simulation. Thus, we are using the simulations as a qualitative guide to the trends in the data. With a transverse resolution of 1.25 λ_0, there are 440 independent phase-plate elements or independent Fourier components for the incident laser light, which is a statistically representative sample.

In Figure 2, we show the stimulated Raman and Brillouin scattering reflectivities for different smoothing conditions, when both stimulated scatterings are competing for laser energy. In this case, smoothing by spectral dispersion would appear to be more effective than polarization smoothing in suppressing the SBS. However, this happens merely because the SRS has taken a significant amount of energy from the

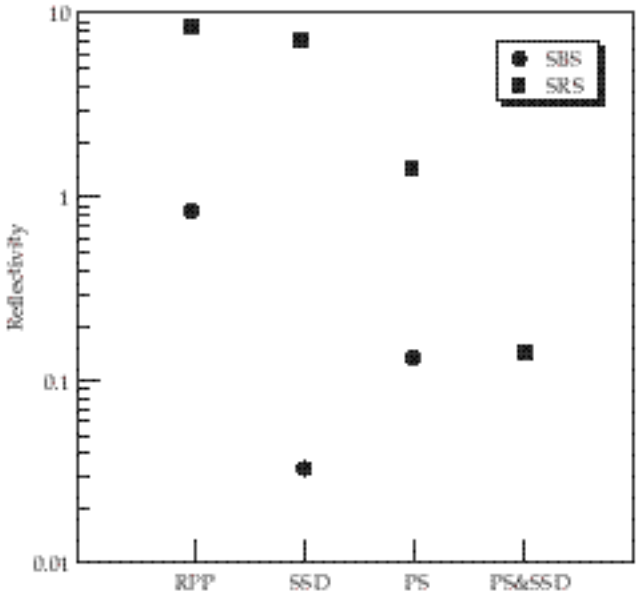

FIGURE 2. The stimulated-Raman-scattering and stimulated-Brillouin-scattering reflectivities, in a 10% critical plasma, are shown for different smoothing conditions when both instabilities are present in the simulation. (08-00-1298-2536pb01)

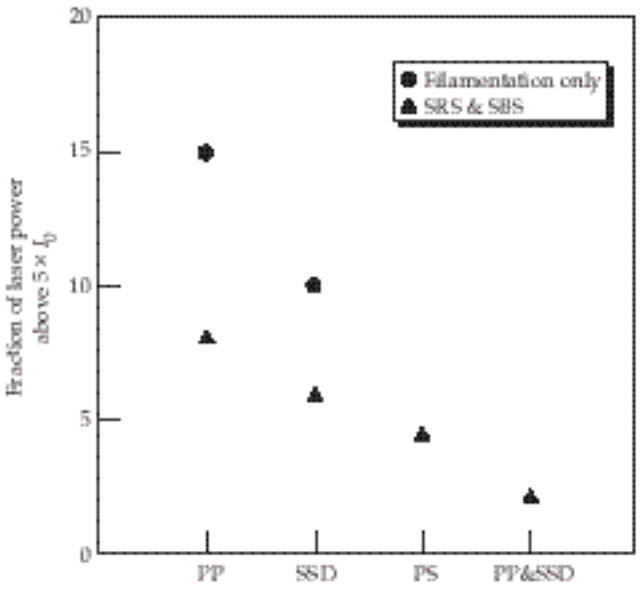

FIGURE 3. The stimulated-Brillouin-scattering reflectivity and the fraction of laser energy having more than five times the average intensity (I_0), for different smoothing conditions. The values have been averaged over the last 20 ps of the simulation to eliminate transient effects (T_i / T_e = 0.11; the axial length, L_z = 351 μm = 1000λ_0; an electron temperature of 2.7 keV; and an electron density of 0.07 n_c) (08-00-1298-2537pb01)

high-intensity laser hot spots in the SSD case, which suppresses the SBS. Simulations without SRS show a SBS reflectivity dependence on smoothing that is similar to the SRS dependence shown in Figure 2.

An interesting feature of Figure 2 is the prediction that the combined smoothing techniques will dramatically suppress stimulated Brillouin scattering, as well as reduce stimulated Raman scattering—despite the very fast growth rate of the latter. We attribute this reduction to the effective control of filamentation that the combined techniques have, as is shown in Figure 3. Here, the fraction of laser beam power at an intensity greater than $5 \times I_0$ (where I_0 is the average intensity) is shown as a function of beam smoothing, with and without stimulated backscatter. Without polarization smoothing, the simulations with backscatter show less power at high intensity because power is lost from the speckles as they start to self focus. With polarization smoothing, there is too little backscatter to affect the self-focusing. Combining SSD and PS reduces the power at high intensity more than either method does individually. This fact can explain the simulation result that smoothing by spectral dispersion reduces the stimulated Raman scattering when polarization smoothing is also used.

Using F3D simulations, we have shown that polarization smoothing is a very promising beam-smoothing technique for controlling laser plasma instabilities. This is especially true with respect to stimulated Raman scattering, which the more common smoothing-by-spectral-dispersion technique cannot directly control, because the scattering grows to saturation before the hot spots can be relocated. However, smoothing by spectral dispersion combined with polarization smoothing is particularly powerful. The latter method dramatically reduces the fraction of the beam power at high intensity, thus lowering filamentation growth rates and Brillouin instabilities to a level ($\Delta\omega \approx \gamma_0$) where the smoothing by spectral dispersion is more effective. At these levels, smoothing by spectral dispersion can also indirectly reduce stimulated Raman scattering by reducing self-focusing of the hot spots.

We also carried out simulations with plasma conditions that favored growth of stimulated Brillouin scattering over stimulated Raman scattering (T_i / T_e = 0.11; an axial length, L_z = 351μm = 1000λ_0; an electron temperature of 2.7 keV; and an electron density of 0.07n_c). Under these conditions, the stimulated Raman scattering is always insignificant, and the stimulated-Brillouin-scattering reflectivity follows similar trends to those shown in Figure 2 for the stimulated-Raman-scattering reflectivity.

Gasbag Plasma Experiments

We used the Nova laser to do experiments with targets developed to reproduce the plasma conditions and length scales of the NIF. As mentioned earlier, the

two plasma conditions of importance for the NIF are the inner-beam plasma (a large-scale-length, low-Z plasma, with high-gain exponents for both stimulated Raman and Brillouin scatterings), and the outer-beam plasma (with shorter scale lengths and a higher-gain exponent for stimulated Brillouin scattering in the plasma near the Au wall).[19]

The low-Z, inner-beam case was studied with gasbag targets. These consist of two membranes, one on either side of a thin Al washer, which are inflated with a C_3H_8 and C_5H_{12} gas mixture at a one atmosphere pressure to produce an almost spherical gas volume. Nearly symmetric irradiation by nine heater beams produces a 6% to 15% critical-density plasma, with 1- to 2-mm scale lengths and a peak central T_e = 3 keV. The tenth Nova beam, called the interaction beam, was used to drive the instabilities in the plasma. It was configured as an $f/8.5$ beam, with options for smoothing by spectral dispersion and polarization smoothing.

Figure 4 shows the stimulated Raman and Brillouin scattering reflectivities that were measured from gasbag targets. Most of the data shown is for intensities of ~2×10^{15} W/cm^2. All targets with density above 13% critical used a higher interaction intensity of ~5×10^{15} W/cm^2. These high-intensity experiments were intended to explore the conditions expected in a higher-radiation-temperature, NIF-hohlraum design. Most of the data points show that, while polarization smoothing reduces the scattering levels, the reduction is not as significant as when it is combined with SSD. This combination gave the most effective beam smoothing ever observed in Nova gasbag experiments. These results show that NIF will benefit from polarization smoothing of the inner beams.

Some of the backscatter data taken with gasbag targets show stimulated Raman and Brillouin scattering values with large departures from their respective averages. We have identified possible systematic reasons for these departures in some, but not all, cases. Backscattering values that exhibit a sudden departure from the average are typically characterized by an increase (decrease) in the SRS and a decrease (increase) in the SBS. We are continuing to analyze the full data set in an effort to identify all reasons for scatter in the data. These observations, if borne out by further analysis, indicate that the interdependence of SRS and SBS makes the study of the effect of beam smoothing on one, or both, more complicated. We are continuing our efforts to develop a predictive model for laser beam filamentation and SBS and SRS backscatter (F3D) that will enable us to calculate the interaction of a complete NIF beam with a macroscopic target.

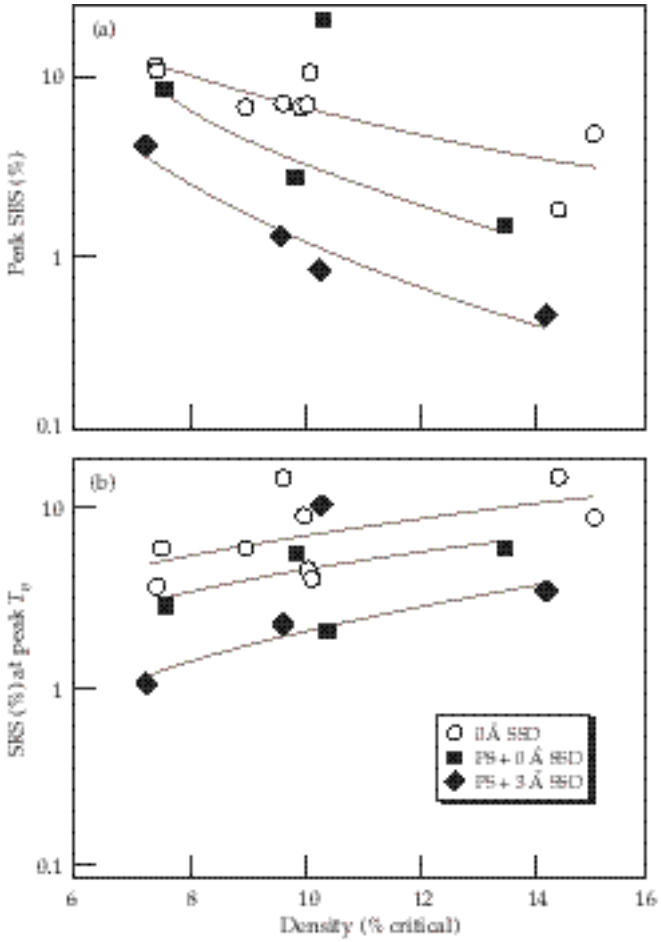

FIGURE 4. Experimental measurements of the (a) stimulated-Brillouin and (b) stimulated-Raman scattered light in gasbag plasmas. The probe intensity is 2×10^{15} W/cm^2, except at the high density where it is 5×10^{15} W/cm^2. The SSD bandwidth is given at 1.053 nm. The scattering includes backscattered light measured in a 15° cone around the backward direction. (08-00-1298-2538pb01)

Conclusions

Our F3D numerical simulations have given us a very optimistic view about the usefulness of polarization smoothing as a highly effective smoothing technique for suppressing laser-plasma instabilities. Although the data indicates that polarization smoothing, by itself, is only partly effective at reducing backscattering losses, our measurements confirm the trends in the simulations. In particular, they show that combining polarization smoothing with smoothing by spectral dispersion provides the most effective way to suppress the instabilities.

The peak scattering observed over the entire experimental range under the maximum (combined) smoothing conditions is below 6% most of the time. Occasionally, either the stimulated Raman or the stimulated Brillouin scattering exhibits a jump, with a corresponding drop in the other, which (in some cases) can be associated with a density or temperature change in the gasbag plasma. Other cases exist, however, in which the sudden jumps in scattering cannot yet be associated with a possible cause. We are continuing to investigate the details of these cases and are

developing a more rigorous connection between the jump in scattering levels and a change in plasma or laser parameters.

The stimulated Brillouin and Raman scatterings in NIF-scale hohlraums should be at tolerable levels with moderate amounts of beam smoothing, even at the higher intensities and densities expected in the 350-eV ignition designs. Our polarization smoothing experiments suggest that this technique, when combined with smoothing by spectral dispersion, can improve the margin against plasma instabilities, thereby increasing the operating region available to the NIF for ICF experiments. The experimental results strongly suggest considering a retrofit of the NIF to include polarization smoothing and its further investigation as part of the experiments scheduled for the NIF's first bundle.

Acknowledgments

The authors acknowledge the contributions of B. J. MacGowan, S. H. Glenzer, R. K. Kirkwood, C. Geddes, L. J. Suter, E. Lefebvre, A. B. Langdon, E. A. Williams, and B. Still.

Notes and References

1. J. D. Lindl, *Phys. Plasmas* **2**, 3933 (1995).
2. R. H. Lehmberg and S. P. Obenschain, *Optics Comm.* **46**, 27 (1983); R. H. Lehmberg and J. Goldhar, *Fusion Technology* **11**, 532–541 (1987).
3. Y. Kato, K. Mima, N. Miyanaga, S. Arinaga, Y. Kitagawa, M. Naktsuka, and C. Yamanka, *Phys. Rev. Lett.* **53**, 1057–1060 (1984).
4. S. Skupsky, R. W. Short, T. Kessler, R. S. Craxton, S. Letzring, and J. M. Soures, *J. Appl. Phys.* **66**, 3456 (1989).
5. J. E. Rothenberg, *Proc. Soc. Photo-Opt. Instrum. Eng.* **2633**, 634 (1995).
6. "Phase Conversion Using Distributed Polarization Rotation," *LLE review* **45**, 1–12 (1990).
7. K. Tsubakimoto, M. Nakatsuka, H. Nakano, T. Kanabe, T. Jitsuno, and S. Nakai, *Opt. Commun.* **91**, 9–12 (1992); K. Tsubakimoto, T. Jitsuno, N. Miyanaga, M. Nakatsuka, T. Kanabe, and S. Nakai, *Opt. Commun.* **103**, 185–188 (1993).
8. S. Pau, S. N. Dixit, and D. Eimerl, *J. Opt. Soc. Am. B* **11**, 1498 (1994).
9. E. Lefebvre, R. L. Berger, A. B. Langdon, B. MacGowan, J. E. Rothenberg, and E. A. Williams, *Phys. Plasmas* **5**, 2701 (1995).
10. S. N. Dixit, J. K. Lawson, K. R. Manes, H. T. Powell, and K. A. Nugent, *Opt. Lett.* **19**, 417 (1994).
11. B. J. MacGowan et al., *Phys. Plasmas* **3**, 2029 (1996). B. J. MacGowan et al., *Proceedings of the IAEA, 16th International Conference on Plasma Physics and Controlled Nuclear Fusion*, Montreal, Quebec, Canada, Oct. 1996, *Fusion Energy* 1996, Vol. 3, 181 (1997).
12. B. J. MacGowan et al., *Proceedings of the IAEA, 17th International Conference on Plasma Physics and Controlled Nuclear Fusion*, Yokohama, Japan, Oct. 1998, *Fusion Energy 1998*, in press. (Article preprint available as: *Laser Beam Smoothing and Backscatter Saturation Processes in Plasmas*, UCRL-JC-132191.)
13. S. W. Haan et al., *Phys Plasmas* **2**, 2480 (1995).
14. Y. Katoet al., *Phys. Rev. Lett.* **53** 1057 (1984).
15. S. H. Glenzer et al., *ICF Quarterly Report*, **8**(1), 7–14, Lawrence Livermore National Laboratory, Livermore, CA, UCRL-LR-105821-98-1 (1997).
16. J. W. Goodman, "Statistical Properties of Laser Speckle Patterns," in *Topics in Applied Physics*, J. C. Dainty, ed., vol. 9, pp. 12–29, Springer-Verlag, New York (1984).
17. *Ibid*, pp. 35–40.
18. R. L. Berger, C. H. Still, E. A. Williams, and A. B. Langdon, manuscript submitted to *Physics of Plasmas* (1998).
19. S. H. Glenzer et al., *Phys. Rev. Lett.* (1998).

DESIGN AND PERFORMANCE OF FLASHLAMP-PUMPED ND:GLASS AMPLIFIERS FOR THE NIF

A. C. Erlandson *C. Marshall* *M. Rotter* *O. Carbourdin** *G. LeTouze**

T. Alger *E. Moor* *S. Sutton* *E. Grebot** *X. Maille**

J. Horvath *L. Pedrotti* *L. Zapata* *J. Guenet** *S. Seznec**

K. Jancaitis *S. Rodriguez* *J. Beullier** *M. Guenet**

Introduction

The National Ignition Facility (NIF) will use a 192-beam, 1.8-MJ laser for inertial confinement fusion (ICF) experiments.[1] A major laser component of the NIF, the flashlamp-pumped Nd:glass amplifiers must provide sufficient gain and stored energy to meet requirements for laser energy and power while adding minimal wavefront distortion to the laser beams. The NIF amplifiers differ from those used in previous ICF laser systems mainly in their overall scale and packaging. Figure 1 shows a two-slab-long, 4×2 NIF amplifier module, where the $n \times m$ designation denotes the number (height $\times$ width) of parallel amplifying channels or beam apertures that are combined. The NIF amplifiers use 40-cm-square apertures, which approximate the practical size limit imposed by amplified spontaneous emission (ASE) that depumps the laser slabs and limits gain. Large-aperture size reduces system costs by reducing the number of laser beams needed to produce the required energy on target. Previously, the largest amplifiers constructed were the 2×2 Beamlet amplifiers, which combined only four 40-cm-square apertures.[2]

Amplifiers with combined beams were first proposed by Lawrence Livermore National Laboratory (LLNL) in 1978 as a way of reducing the cost of MJ-class fusion laser systems.[3] Combining beams in a single enclosure reduces costs in three ways: (1) by making amplifiers more compact, thereby reducing the size and cost of the building; (2) by increasing pumping efficiency, thereby reducing the size and cost of the power-conditioning system; and (3) by reducing the number of internal amplifier parts. The NIF design achieves considerable cost savings by making the NIF amplifiers larger than the Beamlet amplifiers. Similar amplifiers will be used in the Laser Megajoule (LMJ), a 240-beam laser system now being developed and designed by the French Commissariat a l'Energie Atomique (CEA). Much of the development work for the LMJ amplifiers resulted from collaborative efforts between scientists and engineers at LLNL and the French CEA.

This article describes the design and performance of the NIF amplifiers. First, we describe the NIF amplifier design. Next, we describe the prototype amplifier we tested and discuss the equipment used to measure its optical performance. We then compare model predictions with measurement results, and show performance predictions for the NIF amplifiers that are based on our test results and validated models.

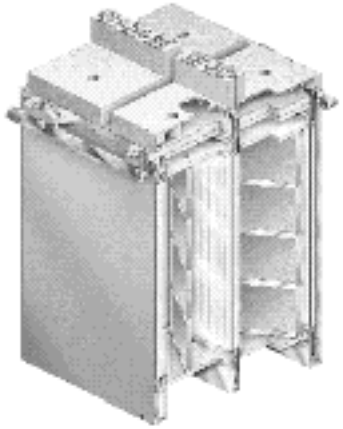

FIGURE 1. A two-slab-long, 4×2 NIF amplifier module. (70-00-0199-0056pb02)

*Commissariat a l'Energie Atomique (French Atomic Energy Commission)

NIF Amplifier Design

Pump Cavity Design and Performance

The NIF amplifiers provide optical gain at the 1.053-μm wavelength by using neodymium-doped, phosphate glass, rectangular laser slabs oriented at Brewster's angle with respect to the beam, to eliminate reflection losses. The slabs have absorbing glass edge claddings to prevent internal parasitic laser oscillation. Each slab holder supports four slabs, one stacked above the other. Central flashlamps cassettes pump slabs in both directions, while side flashlamp cassettes with large silver reflectors pump slabs in one direction. The glass blastshields between the flashlamps and the laser slabs serve three purposes: (1) they prevent acoustic waves generated by the flashlamps from propagating into the beam path and causing wavefront distortion; (2) they provide a contamination barrier between the flashlamp cavity and the critical slab cavity; and (3) they form one wall of the channel used for flowing cooling gas around the flashlamps. Figure 2 shows a plan view of a single NIF amplifier slab column that illustrates the arrangement of the slabs, flashlamps, blastshields, and reflectors.

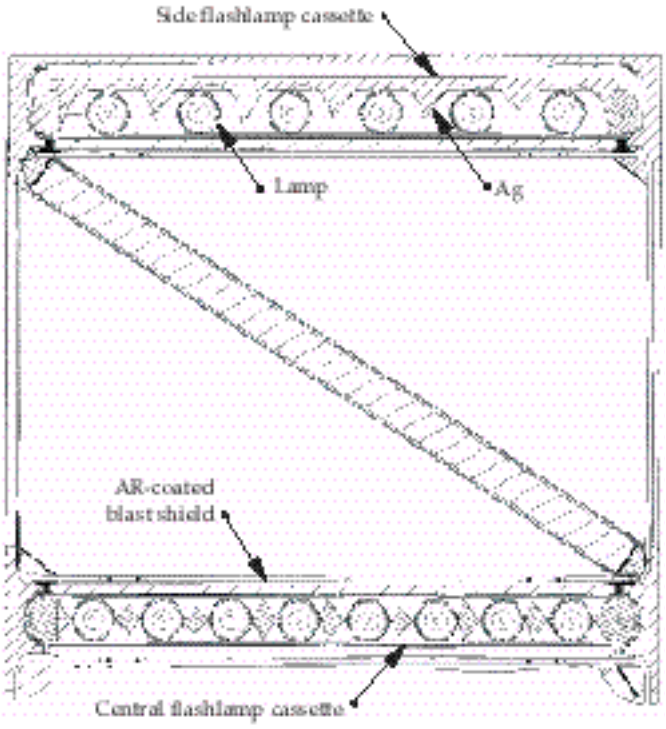

FIGURE 2. Plan view of the NIF amplifier pump cavity.
(70-00-0199-0057pb02)

The NIF amplifiers must meet requirements for gain, gain uniformity, wavefront distortion, and thermal recovery rate. High gain is required for the laser to meet its output energy and power requirements, especially because of the limited injected-energy from an affordable pulse generation system. At the same time, the amplifier must achieve its gain requirements efficiently to reduce the size and cost of the power-conditioning system used to drive the flashlamps. Accordingly, the NIF amplifiers use several features to increase efficiency. The side flashlamp arrays use silver reflectors with involute reflector shapes. They are designed to reflect flashlamp light toward the laser slabs, while returning little flashlamp light back to the absorbing flashlamp plasma.[4] Compared with flat reflectors, the involute reflectors reduce the flashlamp electrical energy required to meet the gain requirement by ~15%. Additional reductions in flashlamp electrical energy are achieved by using sol-gel antireflective (AR) coatings on both sides of the blastshields (7%) and by preionizing the flashlamps with weak electrical pulses delivered several hundred microseconds before the main pulse (10%). Preionization causes the flashlamp arc to develop more uniformly, and it increases the electrical-to-optical conversion efficiency of the flashlamp plasma. Overall, the predicted storage efficiency of the NIF amplifiers is 3.8%, which is significantly higher than those in previous ICF lasers (3.0% and 1.8% for the Beamlet and Nova amplifiers, respectively).[2] Storage efficiency is defined as the total extractable energy stored in the laser slabs divided by the electrical energy delivered to the flashlamps.

In addition to the above criteria, we want the amplifiers to produce uniform gain distributions across their apertures, so that uniform beam output fluence can be readily obtained. Uniform output fluence is essential for maximizing output energy while maintaining acceptable optical damage risk. With significant gain variations, it becomes necessary to compensate by increasing the input fluence distribution in regions of the aperture with lower gain, as was done on the Beamlet laser. In large slabs, such as the 4.1- × 45.8- × 80.9-cm slabs used in the NIF amplifiers, the transverse gain uniformity is determined not only by the distribution of flashlamp light across the slab, but also by internal amplified spontaneous emission. ASE preferentially depletes gain near the slab's ends because this position has the longest path length for internal amplification.[2,5] The skewed diamond-shaped reflectors in the central flashlamp arrays reduce gain variations in the NIF pump-cavity design by directing flashlamp light preferentially near the slab ends.

We used a 3D ray-trace code to evaluate reflector shapes and to predict gain distributions across the aperture. The 3D code calculates pump rates for the

neodymium-ion inversion by using a reverse ray-trace technique where rays were propagated backward from the point of interest in the slab to the flashlamp plasma. The ray-trace model tracked the change in the spectral content of each ray as it interacts with various reflecting and transmitting media present in the pump cavity. The absorption and reflectance properties of cavity components and the emission properties of the lamp plasma were determined experimentally.[6] Once the pump distribution was calculated as a function of flashlamp power, the peak gain-coefficient distribution was calculated by solving the differential equation for stored energy density as a function of time at each point in the slab. In addition to radiative and non-radiative spontaneous decay processes, the model also tracked spatially- and temporally-dependent ASE decay rates throughout the volume of the laser slabs. Both the physical assumptions in the model and the calculational techniques used in the computer programs that implement the gain model have been described in detail in earlier publications.[7,8,9]

Wavefront distortion is produced by waste heat deposited in the laser slabs by flashlamp pumping processes. Wavefront distortion has a prompt component that is caused by the flashlamp heating the laser slabs during the shot; it also has a residual thermal component that is caused by thermal energy remaining in the pump cavity from previous shots. The prompt component is primarily caused by the uneven heating of the two sides of the slab. This causes the slab to warp before the laser beam passes through the slabs when peak gain is attained.[10] Residual thermal distortions are caused by thermal gradients in the laser slabs themselves, as well as thermal gradients in the gas that is convectively heated by the laser slabs. The residual slab distortions, like the prompt pump-induced distortion, tend to be low order. The deformable mirror system now planned for the NIF is expected to correct the residual slab distortions. The gas distortions, however, have higher spatial frequencies and are more rapidly varying, making them difficult to correct.

To accelerate the recovery from residual thermal distortion, the NIF flashlamps will be actively cooled by flowing gas. Flashlamp cooling is effective because some 60% of the pump waste heat resides in the flashlamp envelopes immediately after a shot. Although water cooling has been successfully used to accelerate the shot rate of the OMEGA Laser at the University of Rochester,[11] gas cooling was chosen for the NIF to eliminate water-jacket tubes and to leave more room for efficiency-enhancing reflectors. NIF flashlamp cooling system will provide gas flow rates of up to 20 cubic feet per minute per flashlamp, with the gas flow direction alternating between flashlamp cassettes as shown in Figure 3. The inlet temperature of the cooling gas will be controlled over a ±5°C range centered about the ambient temperature with ±0.3°C accuracy.

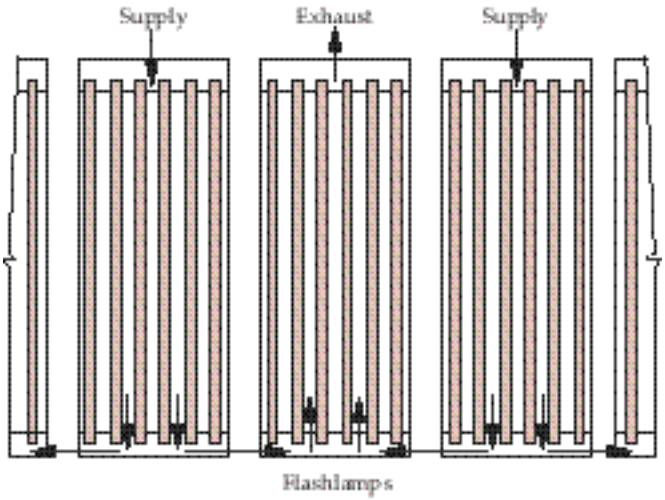

FIGURE 3. Alternating the direction of cooling gas flow through the flashlamp cassettes enabled us to put cooling-gas connections at the top of the amplifier, thereby simplifying the amplifier mechanical design. (70-00-0199-0058pb02)

We used several computer codes to calculate the wavefront distortion induced by flashlamp pumping processes. The prompt temperature rise, which was assumed to be proportional to the time-integrated local pump rate, was calculated using a 2D ray-trace code, which was a precursor to the 3D ray-trace code described above.[12] The residual temperature component was calculated using a finite-element heat transfer program, with starting temperatures set equal to values measured on a test amplifier shortly after firing the flashlamps.[13] The calculated temperature distributions were used as input for finite-element calculations of the deformation and stress in the laser slabs.[14] The final step in the calculation sequence was to use the calculated temperature, deformation, and stress distributions in a ray-trace algorithm to evaluate the optical path length variations across the aperture.[15] The effects of refractive index responses to temperature and stress were included in the calculations.

Mechanical Design

The large scale of the NIF amplifiers requires new mechanical designs that allow convenient assembly and maintenance. Accordingly, the NIF amplifiers use a modular design in which the most critical components, including the flashlamps, laser slabs, and reflectors, are mounted in line-replaceable units or cassettes that can be readily inserted or removed without disturbing their neighbors.[16] See Figure 4.

The design uses sealed maintenance carts that access the bottom of the amplifiers in order to install and remove flashlamp cassettes and four-high slab cassettes. The cassettes are inserted and removed from their enclosure, called the frame assembly unit, which

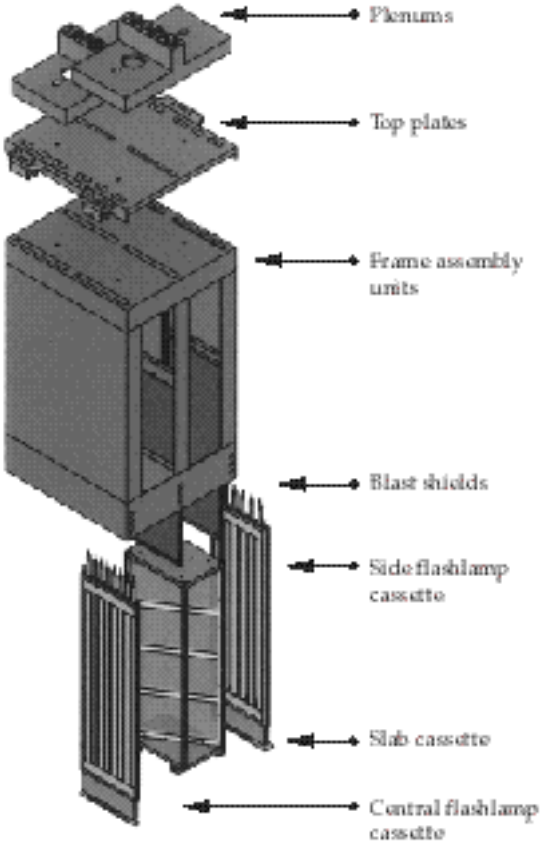

FIGURE 4. The NIF amplifiers use a modular design. (70-00-0199-0059pb02)

is supported by top plates mounted to an overhead support structure. Plenums distribute electricity and cooling gas to the flashlamps from the top, through holes on the top plate.

Each NIF 4 × 2 beam bundle uses an 11-slab-long main amplifier that the beam passes four times, and a five-slab-long power amplifier that the beam passes twice. Assembly of these amplifiers begins in an off-line clean room, where the frame assembly units are cleaned and the top plates and blast shields with anti-reflective coatings are installed. A flashlamp-light-resistant polymer is used to bond the blast shields to a metal frame, and silicone inflatable seals are used to seal the metal frame to the inside of the frame assembly unit. These seals reduce leak rates between the flashlamp cavity and the slab cavity. After the blast shields have been installed, frame assembly units are bolted together to form 5- and 11-slab-long units that are transported to the laser bay where they are mounted to an overhead support structure by their top plates.

The laser slabs, reflectors, and metal parts that comprise the slab cassettes are spray-cleaned and assembled in an elevated, class-100 clean room. We have to maintain high cleanliness levels because small particles resting on the laser slabs can cause damage when heated by flashlamp and laser light. Current specifications call for the laser slabs and metal surfaces to be maintained at cleanliness levels of 50 and 100, respectively. The levels correspond to particle-size distributions in which there are only one 50- or 100-µm particle per square foot of surface area, respectively. Following assembly, the slab cassettes are lowered into a specialized clean cart. Once the cart has been moved to the laser bay, it docks to the bottom of a frame assembly unit and establishes a hermetic seal to maintain cleanliness. After the top cover of the cart and the bottom cover of the frame assembly unit have been pressed together to trap residual particles, the cover pair is moved to the side to open a passageway for the slab cassette to be raised into the frame assembly unit. Rollers mounted in the corners of the cassette guide the cassette during insertion and prevent metal-on-metal rubbing, which generates particles. A fail-safe mechanism in the cart activates latches that hold the slab cassette in place. Slab cassettes can be removed for occasional refurbishment by reversing this installation process. Figure 5 shows a prototype slab cassette cart, which has successfully completed some 50 slab-cassette transfers in our laboratory. Similar carts will be used to install and remove the NIF flashlamp cassettes and blast shields.

NIF Prototype Amplifier Design

We have built and tested a prototype amplifier at LLNL to validate key requirements prior to deployment in NIF. This prototype amplifier was extremely close to the NIF amplifier design, as it used the same size flashlamps and laser slabs and nearly the same reflector shapes. The prototype amplifier was slightly more compact in the direction transverse to the laser beam because the insertion clearances between the slab cassettes and the frame assembly units are smaller, and the blast shields are thinner. In addition, the prototype was slightly more compact in the direction parallel to the beam due to smaller gaps between frame assembly units. Ray-trace codes that we have developed to predict amplifier gain show that the differences in gain and storage efficiency between the prototype amplifier and the NIF amplifiers are negligible.

The prototype amplifier was tested as a one- , two- , and three-slab-long amplifier. Both the “diamond” and “X” configurations of the two-slab-long amplifier were tested. Amplifiers of different lengths were tested in order to infer the gain and wavefront distributions of the interior slab; this was important because the 5- and 11-slab-long NIF amplifiers have many interior slabs in addition to X and diamond end slabs. Figure 6 shows the diamond, X, and three-slab-long amplifier configurations we tested.

To measure temperatures at approximately 80 different locations inside the amplifier, we used

FIGURE 5. The prototype slab cassette cart shown inserting a slab cassette into the NIF prototype amplifier. (70-00-0199-0060pb02)

thermocouples. They were placed on three laser slabs in one of the slab cassettes with holes drilled through the slabs to establish good thermal contact. Thermocouples were also placed on flashlamps, blast shields, and reflectors near the slab cassette. The purpose of the temperature measurements was to determine the initial temperature rise of the pump cavity components and to determine cooling rates after shots.

The laser slabs in the prototype amplifier were finished from LG-770 glass made by Schott Glass and LHG-8 glass made by Hoya. Both types of laser glass had Nd ion concentrations of 4.2×10^{20} ions/cm^3. The flashlamps were made by EG&G and ILC Technology.

Apparatus for Gain and Wavefront Measurements

We constructed an optical diagnostic system to perform time-resolved gain and wavefront measurements over the entire aperture of our prototype amplifier. Measurements were performed using a pulsed, injection-seeded, single-longitudinal mode, Nd:YLF probe laser operating at 1.053 μm. This laser produced 80-mJ, 20-ns-long pulses at a repetition rate of 13 Hz. The probe laser beam was expanded and image relayed by a series of telescopes. After passing through the amplifier once, the beam reflected back through the amplifier and telescopes a second time. After returning from the amplifier, a portion of the beam was sampled with a beam splitter and reflected to scientific-grade charge-coupled device (CCD) cameras for gain and wavefront measurements. Figure 7 shows a schematic of our equipment.

Amplifier gain distributions were determined by calculating the ratio of the images produced by two CCD cameras (the gain reference camera and the gain probe camera); they recorded the laser beam intensity before and after the beam passed through the amplifier. Measured background contributions from the flashlamp light and amplified spontaneous emission were subtracted from the gain camera image. A correction factor for passive transmission losses was determined by firing the probe laser without firing the amplifier flashlamps. Crosshair images were used to ensure proper registration of the gain and reference camera images.

Wavefront distributions were measured by interfering the probe beam with a reference beam, which was generated with an ~25-m-long single-mode optical fiber cut so that its optical length approximately matched the probe laser path length. To increase the fringe contrast ratio, a half-wave plate and a polarizer

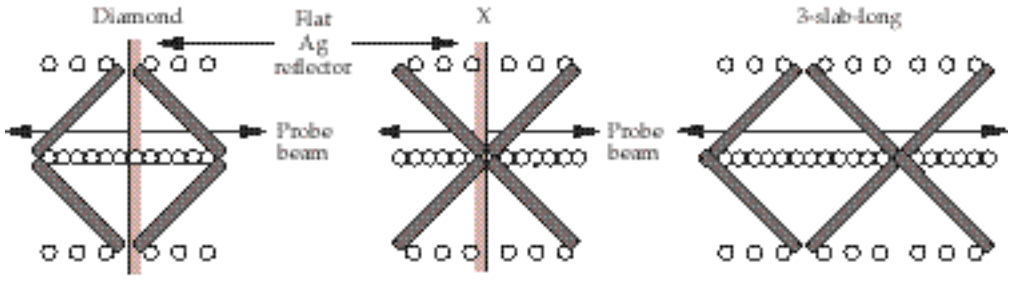

FIGURE 6. Plan view of the prototype amplifier in the diamond, X, and 3-slab-long configurations. (70-00-0199-0061pb02)

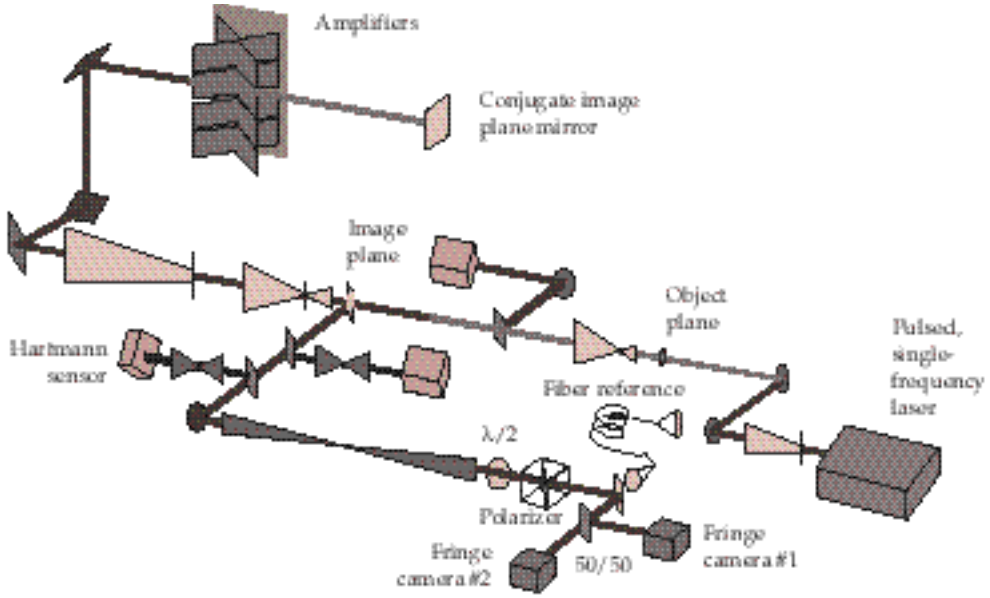

FIGURE 7. We constructed a large-aperture diagnostic system to measure gain and wavefront distributions produced by the prototype amplifier. (70-00-0199-0062pb02)

were used to attenuate the probe laser to approximately the same intensity as the reference beam. Two cameras were used to record interferograms on successive pulses of the 13-Hz probe laser. A Fourier-transform technique was used to calculate wavefront distributions from the interferograms.[17] We checked the calibration of the interferometer by measuring the wavefront of a known lens. From this check, we estimate the accuracy of our wavefront measurements to be ±0.02 waves rms, for both cameras. Prompt pump-induced wavefront distortion was determined by subtracting the wavefront measured at the time of peak gain from the wavefront measured 75 ms earlier.

Measurement Results and Comparison with Model Predictions

Gain measurements were in close agreement with model predictions. For example, Figure 8 shows measured and predicted gain-coefficient distributions for the two-slab-long X configuration, with the flashlamp pulses close to the 34-kJ per lamp, 360-μs-long pulses anticipated for the NIF. Although the distributions in Figure 8 characterize the aperture next to the bottom, distributions measured in the other apertures were

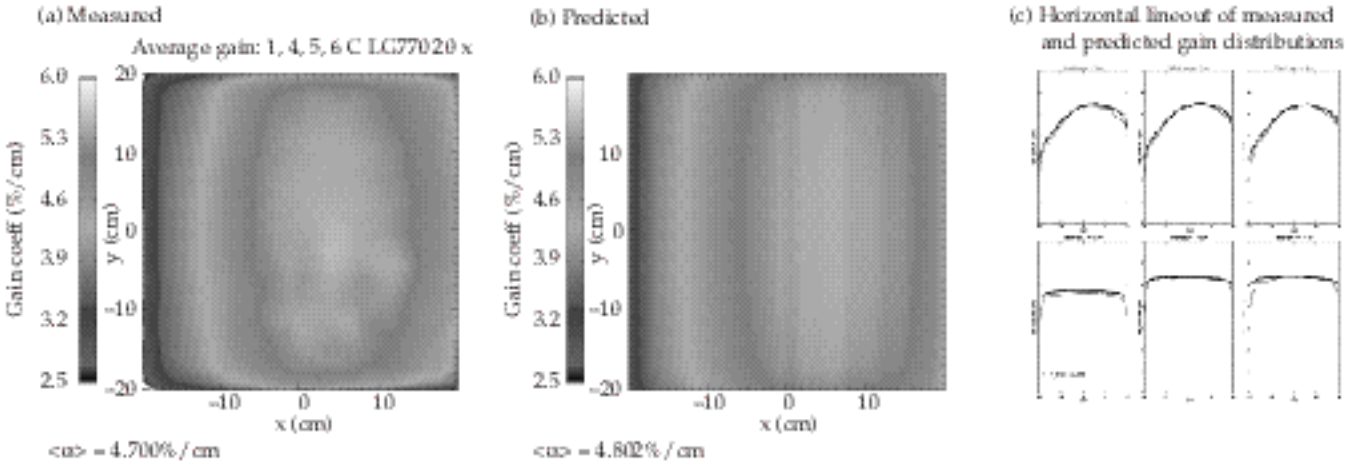

FIGURE 8. Measured and predicted gain distributions for the two-slab-long X configuration, with flashlamps energized with 34-kJ-per-lamp, 360-μs-long pulses. Measurements were made in the next-to-bottom aperture. (70-00-0199-0063pb02)

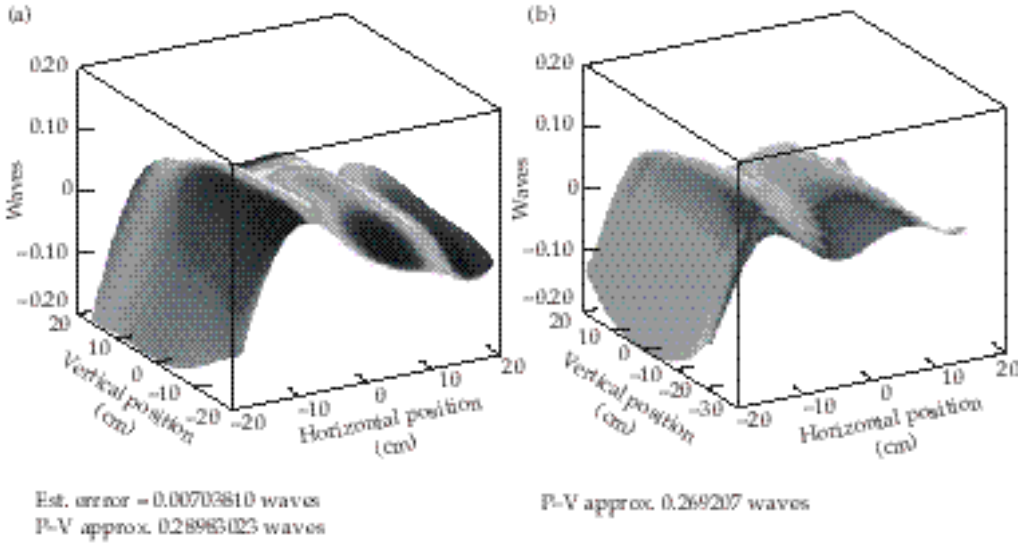

FIGURE 9. (a) Measured and (b) predicted prompt pump-induced wavefront distributions for the two-slab-long "X" configuration, with flashlamps energized with 34-kJ-per-lamp, 360-µs-long pulses. Measurements were made in the next-to-bottom aperture. (70-00-0199-0064pb01)

nearly the same, due to the vertical translation symmetry of the pump cavity. Gain was lower on the right-hand side of the aperture because the right-hand sides of both slabs were close to the ends of the amplifier where pump-light fluences were lower. Differences between the model predictions and measurements were less than 1% rms for all other combinations of apertures and configurations (diamond, X, and 3-slab-long). This agreement was achieved with a single value of the adjustable parameter used in the model to scale the flashlamp pumping rate.

Prompt pump-induced wavefront distortion measurements were also in close agreement with model predictions. Figure 9 compares the measured and predicted prompt pump-induced wavefront distortion for the X configuration and for the standard flashlamp energy of 34 kJ/lamp. The results have been normalized to a single-slab pass. The close agreement between measurements and predictions was obtained using a scaling factor that adjusts the prompt temperature rise in the slab relative to the calculated pumping rate. Equally close agreement was obtained for other apertures and for time delays of up to 1 ms after the time of peak gain, using a single value for the scaling factor.

In addition to the optical characterizations, we also performed temperature measurements to determine the efficacy of the flashlamp cooling system. Figure 10 shows average slab temperature versus time after a flashlamp shot, for two cases: (1) with flashlamp gas set at ambient temperature; and (2) with the flashlamp cooling gas set 0.5°C below ambient temperature. Our data show that the average slab temperature recovers to within ~0.1°C of the ambient temperature in about eight hours using ambient-temperature cooling gas, and in about four hours using slightly chilled gas. Measured gas distortions had high frequency components, with the rms amplitude varying linearly with the difference between the average slab temperature and the ambient temperature. Measured slab distortions were low order and recovered to less than 0.04 waves (peak-to-valley) per slab per pass within 3–4 hours after each shot. This measurement is consistent with the magnitude of the slab distortions, which we expect to correct with a deformable mirror on NIF.

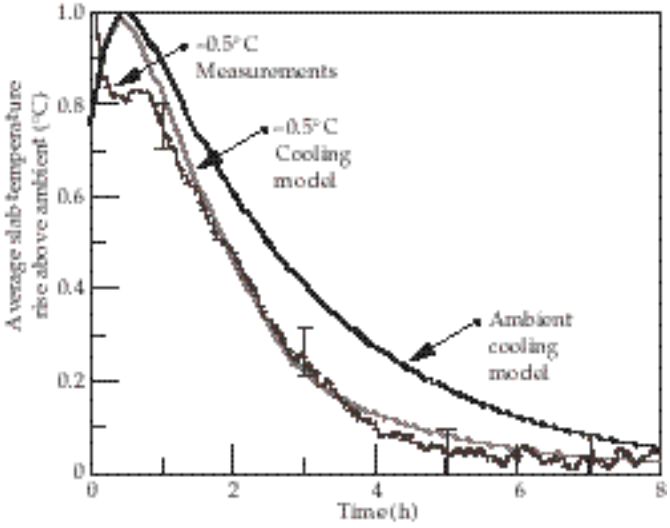

FIGURE 10. Using slightly chilled (–0.5°C) cooling gas accelerates slab thermal recovery rates. (70-00-0199-0065pb02)

Performance Predictions for the NIF Amplifiers

Figure 11 shows the beamline-averaged gain-coefficient distribution for a NIF laser beam, predicted by our validated 3D ray-trace code. The code took into account several features of the NIF amplifiers that were

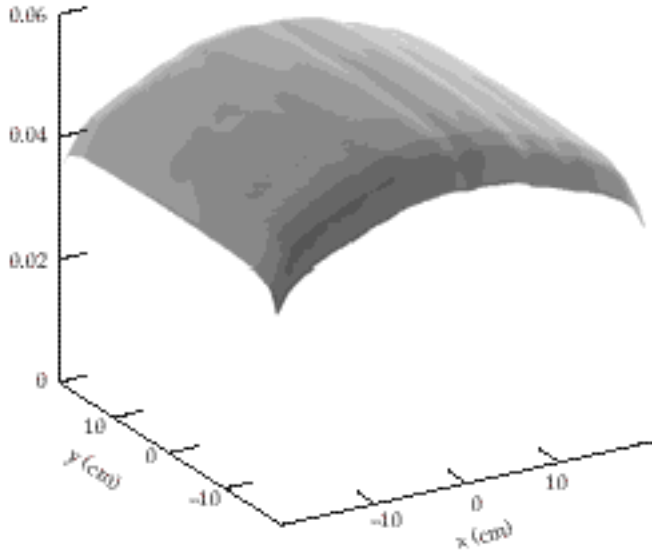

FIGURE 11. NIF beamline-averaged gain-coefficient distribution predicted with the 3D ray-trace code. (70-00-0199-0066pb01)

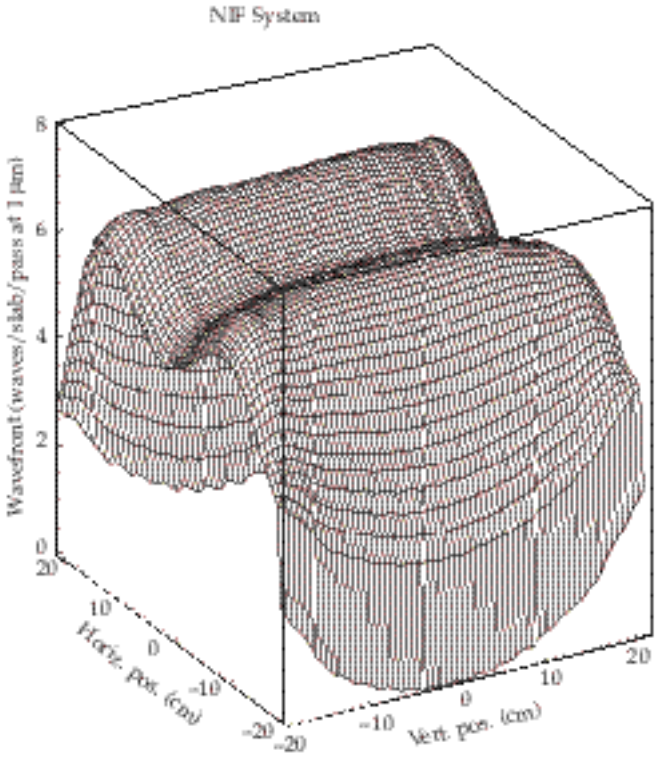

FIGURE 12. NIF beamline prompt pump-induced wavefront distortion predicted with ray-trace and finite-element codes. (70-00-0199-0067pb02)

different from the prototype amplifier: protectively coated Ag reflectors with stable, higher reflectances; improved, two-layer sol-gel antireflective coatings on the blast shields; use of equal numbers of LG-770 and LHG-8 laser slabs; and slight reflector-shape differences. The predicted aperture-averaged gain coefficient was 5.3%/cm, and the distribution shows the expected gain roll-off near the edges due to ASE. Propagation code modeling of the NIF beamline shows that the gain has sufficient magnitude and uniformity for the NIF laser to meet its beam power and energy requirements. To achieve a uniform output fluence distribution and maximum beam output energy, however, the input fluence distribution of the injected laser beam has to be tailored to compensate for the anticipated gain variations.

Figure 12 shows the total prompt pump-induced wavefront distortion for a NIF beamline, predicted with our codes using the source-term scaling factor derived from AMPLAB experiments. The distribution is a low-order "M" shape, with a peak-to-valley value of 5.9 waves. This distribution possibly overestimates the prompt pump-induced wavefront distortion that the NIF beamlines will actually produce, because it is conceivable that stray flashlamp light may have distorted the optics, which are part of the diagnostic. Nonetheless, the predicted distortions are within the range that now appears to be largely correctable with the NIF deformable mirror.

To estimate the effect of the gas distortions on the NIF laser beams, we scaled the gas distortions measured on the prototype amplifier to account for the greater path length and greater number of slabs in the NIF amplifiers. In addition, we used a beam propagation code to calculate the beam focal spot. Our estimate shows that the gas distortions will meet the NIF requirement (less than 5 μrad added beam divergence) within 3 hours after the shot, provided the temperature of the flashlamp cooling gas is ~1°C below the ambient temperature. Figure 13 shows model results for flashlamp cooling with gas at ambient temperature and at 1°C below ambient temperature. The conservative and aggressive estimates correspond to scaling the AMPLAB results by length (for aggressive estimates) and by number of laser slabs (for conservative estimates).

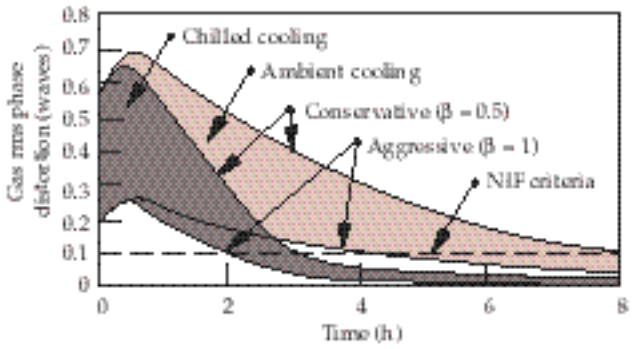

FIGURE 13. Predicted gas-distortion phase disturbances in NIF for ambient and chilled gas cooling. Aggressive and conservative assumptions are used to bracket the problem. (70-00-0199-0068pb02)

Conclusion and Summary

Advances in amplifier technology developed for the NIF include a modular design and bottom-access carts to improve maintenance; features to improve storage efficiency that reduces the size and cost of the power-conditioning; and active gas cooling to accelerate the laser shot rate. Further, gain, wavefront, and thermal recovery measurements performed on the NIF prototype amplifier are consistent with meeting NIF performance requirements.

Acknowledgments

We thank numerous contributors to our design, analysis, and experimental efforts: Richard McCracken, Charles Petty, Lawrence Smith, Alex Drobshoff, John Trent, Drew Hargiss, Randy Aceves, Jerome Hall, Rene Neurath, Joe Smith, Wil Davis, Jean Marie Morchain,* Beatrice Bicrel,* Patrick Manac'h,* Thierry Adjadj,* Gary Ross, John Toeppen, Larry Morris, Jean Lobit,* Douglas Swort, Ronald Bettencourt, Michael Weddle, Loretta Kleinsasser, Dzung Nguyen, John H. Campbell, Daniel Walmer, William, Jerry Britten, Curly Hoagland, Gregory Rogowski, Steve Letts, Cindy Alviso, Irving Stowers, Joe Menapace, Douglas Larson, Scott Hulsey, Phil Test, Steve Fulkerson, George Pollock, Andy Hinz, Anthony Lee, Janice Lawson, Wade Williams, Mark Newton, Ken Manes, Richard London, Yuri Zakharenkhov, Peter Amendt, Jean-Francois Mengue, Fabrisse Laniesse,* John Hunt, Ken Manes, John Murray, Richard Hackel, Jeff Paisner, Steve Payne, and Howard Powell.

Notes and References

1. W. H. Lowdermilk, *Second Annual Conference on Solid State Lasers for Application to Inertial Confinement Fusion*, in *Proc.SPIE*, Bellingham, WA, Vol. 3047, p. 16–37 (1997).
2. A. C. Erlandson, M. D. Rotter, D. N. Frank, and R. W. McCracken, *ICF Quarterly Report* **5**(1), 18–28, Lawrence Livermore National Laboratory, Livermore, CA, UCRL-LR-105821-95-1 (1995).
3. W. F. Hagen, *Laser Program Annual Report–1977*, Lawrence Livermore National Laboratory, Livermore, CA, UCRL-50021-77, pp. 2-228 to 2-231 (1978).
4. W. T. Welford and R. Winston, *High Collection Nonimaging Optics,* Academic Press, New York, NY, p. 266 (1989).
5. A. C. Erlandson, K. S. Jancaitis, R. W. McCracken, and M. D. Rotter, *ICF Quarterly Report* **2**(3), 105–114, Lawrence Livermore National Laboratory, Livermore, CA, UCRL-LR-105821-92-3 (1992).
6. H. T. Powell, A. C. Erlandson, and K. S. Jancaitis, Conference on Flashlamp-pumped Laser Technology, in *Proc.SPIE*, Bellingham, WA, Vol. 609, pp. 78–94 (1986).
7. H. T. Powell, A. C. Erlandson, K. S. Jancaitis, and J. E. Murray, *High-Power Solid State Lasers and Applications*, in *Proc.SPIE*, Bellingham, WA, Vol. 1277, pp. 103–120 (1990).
8. K. S. Jancaitis, S. W. Haney, D. H Munro, G. LeTouzé, and O. Cabourdin, in *Proc.SPIE*, Vol. 3047, pp. 106–111 (1997).
9. G. LeTouzé et al., "3-D Gain Modeling of the LMJ and NIF Amplifiers," *Solid State Lasers for Application to Inertial Confinement Fusion*, Third International Conference 1998 (to be published).
10. J. E. Murray, W. F. Hagen, and B. W. Woods, *Laser Programs Annual Report*, UCRL-50021-82, Lawrence Livermore National Laboratory, Livermore, CA, p. 7–72, (1982).
11. J. H. Kelly, M. J. Shoup III, M. D. Skeldon, and S. T. Bui, *Solid State Lasers III*, edited by G. J. Quarles, in *Proc.SPIE*, Bellingham, WA, Vol. 1627, p. 252–259 (1992).
12. G. LeTouzé, O. Cabourdin, J. F. Mengue, M. Rotter, and K. Jancaitis. "Shaped Reflectors for Pump Cavities," *2nd Annual Conf. Solid State Lasers for Application to ICF*, Limeil, France (1996).
13. A. Shapiro, *TOPAZ3D—A 3-D Finite Element Heat Transfer Code*, UCID-20484, Lawrence Livermore National Laboratory, Livermore, CA (1985).
14. B. N. Maker, *NIKE3D—A Nonlinear, Implicit 3-D Finite Element Code for Solid and Structural Mechanics*, UCRL-MA-105268, Rev. 1, Lawrence Livermore National Laboratory, Livermore, CA (1995).
15. S. Doss and R. Gelinas, *Laser Program Annual Report*, UCRL-50021-86, Lawrence Livermore National Laboratory, Livermore, CA, p. 7–132 (1986).
16. A. C. Erlandson et al., *Second Annual Conference on Solid State Lasers for Application to Inertial Confinement Fusion*, in *Proc.SPIE*, Bellingham, WA, Vol. 3047, p. 16–37 (1997).
17. M. Takeda, H. Ina, and S. Kobayashi, *J. Opt. Soc. Am.*, **72**, 156–160 (1982).

*Commissariat a l'Energie Atomique (French Atomic Energy Commission)

STATUS OF OUR UNDERSTANDING AND MODELING OF IGNITION HOHLRAUM X-RAY COUPLING EFFICIENCY

L. J. Suter *J.-P. Jadaud** *C. Decker* *D. Juraszek**
*E. Dattolo** *R. Turner* *M.-C. Monteil** *B. Lasinski*
S. Glenzer *N. Dague** *O. Landen* *B. MacGowan*

Introduction

The National Ignition Facility (NIF) in the United States[1] and the Laser Megajoule (LMJ) in France[2]—the next generation of high-energy, high-power laser drivers—have the potential of achieving thermonuclear fusion in the laboratory. One key element of achieving that goal is coupling a significant fraction of that energy to a fuel capsule. We can relate the quantity of x-rays absorbed by an indirect-drive ignition capsule, E_{cap}, to the laser energy, E_L, via the expression

$$E_{cap} = \eta_{abs}\,\eta_{CE}\,\eta_{HR\text{-}cap}\,E_L \ , \qquad (1)$$

where η_{abs} is the fraction of incident laser energy absorbed by the hohlraum, η_{CE} is the conversion efficiency of laser light into x rays, and $\eta_{HR\text{-}cap}$ is the fraction of generated x-rays that are actually absorbed by the capsule. As indicated in Figure 1, η_{abs} is typically assumed to be 1 – (SBS + SRS), where SBS is the fraction of incident laser light reflected or scattered out of the hohlraum by stimulated Brillouin scattering and SRS is the fraction reflected by stimulated Raman scattering.[3] E_L is nominally 1.8 MJ for both LMJ and NIF. In the case of NIF, the standard point design capsule[4,5] absorbs 150 kJ of x rays, requiring $\eta_{abs}\,\eta_{CE}\,\eta_{HR\text{-}cap}$ = 0.083. Additional constraints[4] are that the hohlraum be

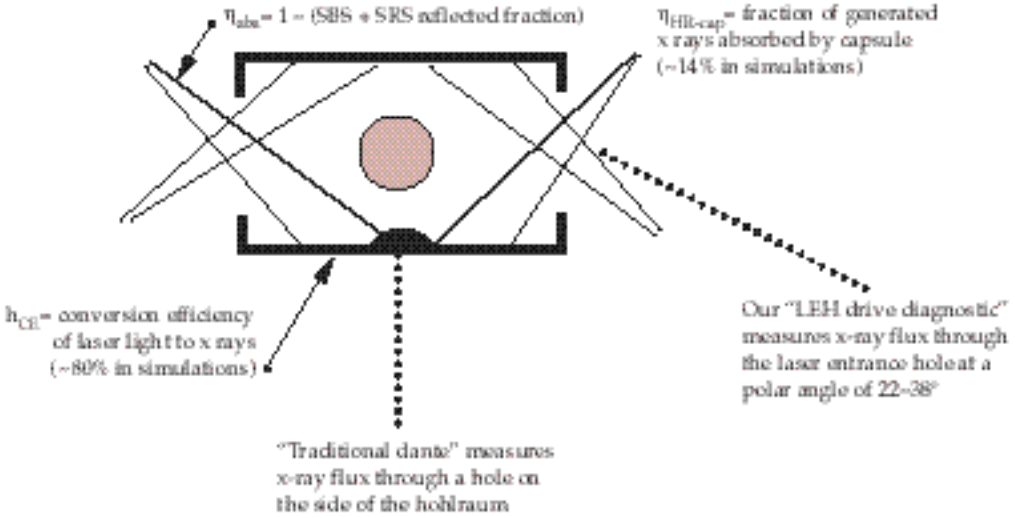

FIGURE 1. Our traditional technique for measuring hohlraum drive is to measure the absolute flux of x rays emerging through a hole in the side of the hohlraum. More recently we have changed to measuring the absolute flux of x rays emerging from the laser entrance hole (LEH) at an angle between 22 and 38°.
(50-00-0199-0085pb01)

*CEA, Centre de Bruyeres-le-Chatel, Bruyeres-le-Chatel, France

gas filled, the laser pulse shape be carefully tailored, and the peak radiation temperature (T_r) be 300 eV.

Numerical simulations of NIF ignition hohlraums show a theoretical conversion efficiency of ~80% and an $\eta_{HR\text{-}cap}$ of ~14%, producing a theoretical $\eta_{CE}\,\eta_{HR\text{-}cap}$ of 0.11. Compared to the 0.083 required efficiency, this provides a 25% margin. This margin was intentionally incorporated into the U.S. program in the early '90s in order to compensate for uncertainties, allowing us to be off somewhat in our assumptions and still be able to achieve ignition. For example, if $\eta_{abs} = 1$ and $\eta_{CE}\,\eta_{HR\text{-}cap} = 0.11$, then $E_L = 1.35$ MJ would successfully drive our ignition design. Or if stimulated backscattering losses proved to be as much as 25% but $\eta_{CE}\,\eta_{HR\text{-}cap} = 0.11$, then NIF's expected 1.8 MJ will successfully drive the ignition design. Likewise, if $\eta_{abs} > 0.75$ and $E_L = 1.8$ MJ, then values of $\eta_{CE}\,\eta_{HR\text{-}cap} < 0.11$ would also work. Similar arguments also apply to the LMJ laser.

Given this picture of capsule coupling efficiency, much of our ongoing Nova research can be broken down into two tasks related to hohlraum energetics.

1. Make η_{abs} as close to 1 as possible in ignition hohlraums.
2. Test if $\eta_{CE}\,\eta_{HR\text{-}cap}$ is as given by hydro simulations.

Success in these two tasks will reduce the uncertainty associated with ignition and perhaps allow us to more profitably use the 25% margin built into the program.

These Nova experiments and their related analysis indicate that both LMJ and NIF coupling efficiency will meet the requirements for ignition. Ongoing experiments studying stimulated Brillouin and Raman backscattering (also known as laser plasma interactions or LPI) in ignition hohlraum "plasma emulators" imply that the total backscattered losses from these two processes should be <10%. These experiments are detailed elsewhere.[6] Here we discuss recent work examining the radiation environment of Nova hohlraums. This work indicates that x-ray production and capsule coupling indeed are very close to our modeling.

$\eta_{CE}\,\eta_{HR\text{-}cap}$

We can test our ability to properly predict $\eta_{CE}\,\eta_{HR\text{-}cap}$ by testing our ability to model / predict the relationship between a hohlraum's drive $T_r(t)^4$ and the incident laser power P_L. To see this heuristically, rewrite equation (1) as

$$\eta_{CE}\,\eta_{HR\text{-}cap}\,(\eta_{abs}\,P_L) = P_{cap} = (1 - \alpha_{cap})A_{cap}\sigma T_r^4, \qquad (2)$$

where P_L is the laser power, $P_{cap} = d\,E_{cap}\,/\,dt$, A_{cap} is the area of the capsule, α_{cap} is the fraction of incident x rays reemitted by the capsule (also known as its albedo), and σ is the Stefan-Boltzmann constant. Thus, for a given capsule of known albedo and area, if we know η_{abs}, then a knowledge of the relationship between laser power, $\eta_{abs}P_L$, and T_r^4 gives us knowledge of $\eta_{CE}\,\eta_{HR\text{-}cap}$.

For a number of years experiments have been carried out on Nova[7,8] and on other facilities[9] to measure radiation flux, or drive, in laser-heated hohlraums. The principal experimental technique was to measure absolute x-ray flux emerging from a diagnostic hole in the side of the hohlraum (which we call here "traditional dante") as shown in Figure 1. The earliest experiments demonstrated the fundamental scaling of drive with laser energy, pulse duration, and hohlraum dimensions. This work also demonstrated increasing hohlraum x-ray conversion efficiency with increased plasma filling; a consequence of the confined nature of the system.[8,9] Efforts were also made to use the traditional-dante data to test the ability of detailed numerical simulations to model the time-dependent hohlraum drive. This work was done both by U.S. researchers with the LASNEX computer code and by French scientists using the code FCI-2 (Fusion Confinement Inertial). Unfortunately, comparisons with detailed modeling often suffered at later times,[8] as shown in Figure 2. We long suspected that this disagreement was not due to fundamental errors in our two-dimensional (2D) modeling but, rather, due to the three-dimensional (3D) nature of our measurements. In particular, we suspected that a plume of cold plasma might be emerging from the hole at later times and scatter out of the diagnostic's line of sight some of the collimated x-ray flux emerging from the hole. For example, a cold plume of optical depth 0.2 could reduce the measured, collimated x-ray flux by 20%.

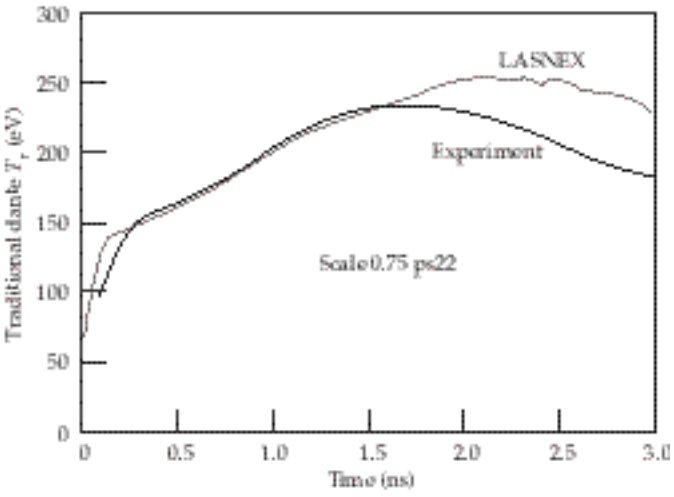

FIGURE 2. "Traditional dante" measurements of time-dependent hohlraum temperature, proportional to (x-ray flux)$^{1/4}$, agrees with detailed simulations up to a certain point. Beyond that, traditional dante is cooler than the modeling. (50-00-0199-0086pb01)

Since the publication of the papers demonstrating and explaining fundamental drive scaling,[7,8] we have redressed the issues related to detailed time-dependent drive in the course of making a number of significant changes in the way in which we study hohlraum drive. These changes include:

1. We now do indirect-drive experiments on Rochester's OMEGA facility.[10] This has demonstrated the fundamental reproducibility of radiation drive in two ways. First, results from that facility behave, quantitatively, as we expect from Nova experiments. Second, the very reproducible laser performance has resulted in drive measurements that virtually overlay one another.
2. Ten smoothed beams have been implemented on Nova,[11] greatly reducing the backscatter in many classes of hohlraums. Complementing this, we now have time-dependent measurements of stimulated Brillouin and Raman backscatter losses available on a regular basis.[12]
3. A very complementary relationship between the French ICF program and the Livermore ICF program has led to a broad range of experiments where, together, we have explored not only main-line ignition hohlraums, but also "pushed the envelope" in drive physics. Figure 3 shows a sample of the variety of hohlraums we have shot through this collaboration. They include "scale 1.0" (25-μm-thick Au cylinders 1.6 mm in diameter, ~2.4 mm long, typically with 1.2-mm-diam laser entrance holes, LEHs, in the endcaps) gas-filled and vacuum hohlraums, various-size reduced-scale hohlraums, some of which are gas filled, and very large hohlraums. These hohlraums were irradiated by a variety of pulses, including flattop pulses of varying lengths and the shaped pulses of Figure 4. As we describe below, many of these experiments have been modeled by both the French ICF code (FCI-2) as well as by LASNEX. The agreement that we find between these two independent codes and experiments is important. It increases our confidence that our successful modeling is due to having properly implemented the essential physics in both our design codes.
4. Possibly the most significant improvement we have made has been to adopt a new diagnostic line of sight; one that measures absolute x-ray flux emerging from the LEH (see Figure 1).[13,14] This was used first on OMEGA[13] and then on Nova.[14] We first tried this because of our concerns, mentioned above, that the later time discrepancy between traditional dante and 2D modeling could be due to the 3D nature of the measurement. We reasoned that a 2D code that includes all the essential physics ought to be able to model an axisymmetric line of sight, such as one through the LEH. Moreover, the plasma plume emerging from the LEH is hot (and therefore transparent to soft x rays) and can be included in our modeling.

Given this background, the balance of the paper divides into two sections. In the first section, we present a sampling of drive measurements made on the variety of OMEGA and Nova hohlraums shown in

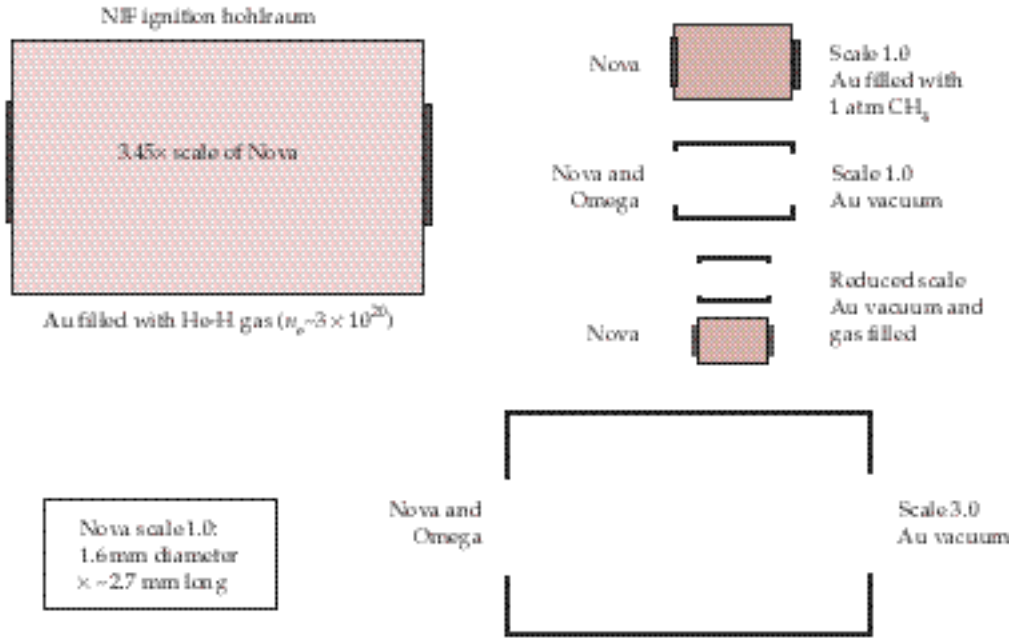

FIGURE 3. We have shot a variety of hohlraums on both Nova and OMEGA. They include gas-filled hohlraums and empty (or "vacuum") hohlraums of various sizes. A scale 1.0 Nova hohlraum is typically 1.6 mm diam, 2.5–2.8 mm long, has LEHs that are 50–75% of the hohlraum diameter, and are made of Au. Other size hohlraums are scaled from these figures. The NIF point design hohlraum is ~3.45 times the Nova hohlraum size. Gas-filled hohlraums have polyimide windows, typically 3500 Å thick. (50-00-0199-0087pb01)

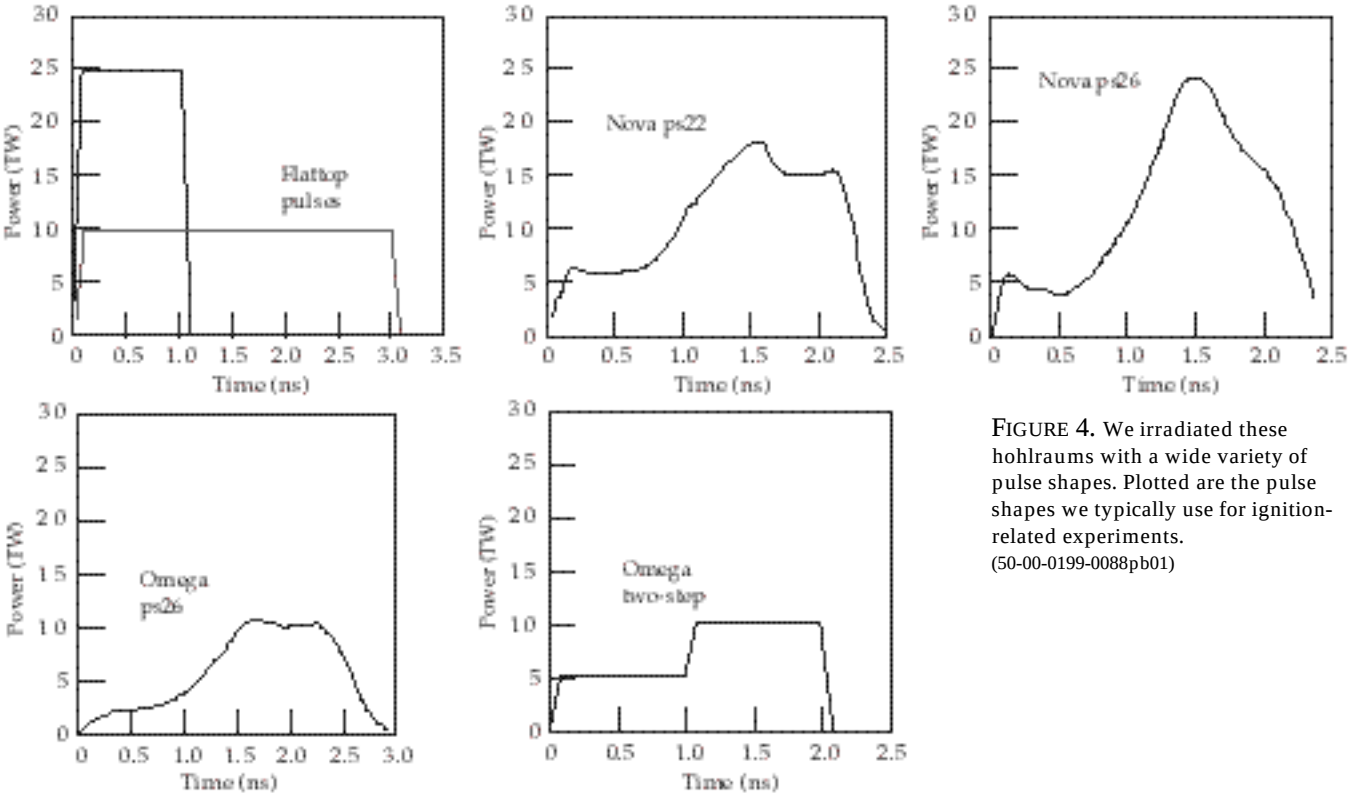

FIGURE 4. We irradiated these hohlraums with a wide variety of pulse shapes. Plotted are the pulse shapes we typically use for ignition-related experiments.
(50-00-0199-0088pb01)

Figure 3, heated by the range of pulse shapes (ps) discussed above. The close comparison between modeling and measurement allows us to quantify the accuracy with which we can model $T_r^4(t)$, which in turn gives us confidence that we can accurately model $\eta_{CE} \cdot \eta_{HR\text{-}cap}$ in an ignition hohlraum.

In the second section, we discuss the set of experiments that conclusively demonstrated that the late time discrepancy between traditional dante and modeling becomes progressively worse with longer pulses, while drive measured through the LEH line of sight agrees reasonably well with simulation. These experiments led to a general acceptance of the LEH line of sight and a repudiation of the traditional dante line of sight in hohlraums that "fill" with plasma. However, just because the LEH line of sight agrees with expectations, it does not mean it is right. In this section, we also discuss work we have done to independently validate this line of sight.

OMEGA and Nova Drive Measurements and Modeling

In April 1998, a series of scale 1.0 hohlraums containing capsules were fielded on OMEGA.These hohlraums were irradiated by OMEGA ps26 (see Figure 4). The hohlraums were oriented so OMEGA dante peered into the hohlraums' LEH at a polar angle of 37.5°. The solid line of Figure 5 represents the drive measured on eight consecutive experiments which had essentially the same incident laser power vs time. Two different LASNEX simulations of the LEH drive are shown. They span the

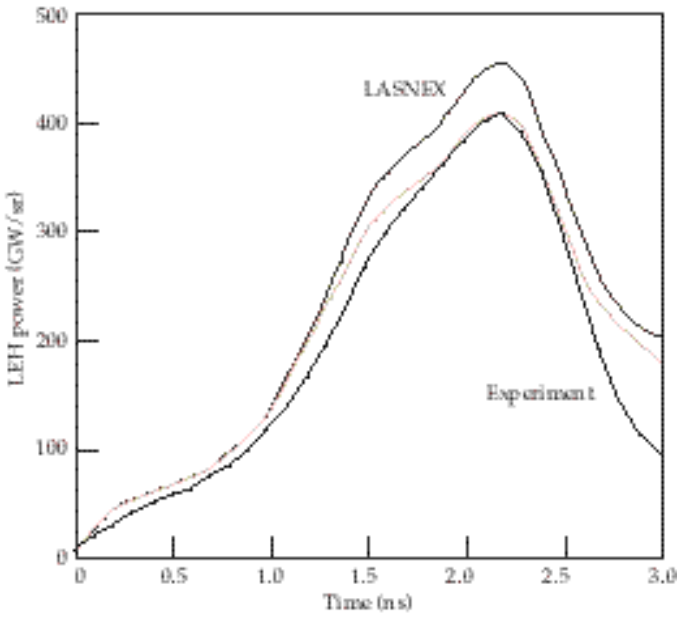

FIGURE 5. Omega ps26 drive measurment vs LASNEX. The experimental data from eight shots overlays one another.
(50-00-0199-0089pb01)

uncertainty in absorption. In order to model a hohlraum with either FCI-2 or LASNEX, we must first reduce the measured, incident laser power by the measured SBS and SRS losses. The upper curve of Figure 5 assumes that the backscattering losses were only what was seen coming directly back into the lens of the OMEGA beam that has a backscatter diagnostic. The lower curve, which nearly coincides with the experimental measurement, assumes that there was also an equal amount of backscatter outside the beam (where there is not yet a diagnostic). This second assumption is consistent with extensive Nova experience.[15] Regardless of the backscattering assumption, the modeling simulates the experiment within ~10% in flux not only throughout the pulse but also well after the laser is turned off, at 2.3 ns.

Figure 6 shows the drive in a methane-filled scale 1.0 Nova hohlraum irradiated by Nova ps26 (Ref. 11). All 10 of Nova's beams were smoothed with kinoform phase plates (KPP)[16] and smoothing by spectral dispersion (SSD).[17] The radiation flux emerging from the LEH at a polar angle of 25° was measured with an absolutely calibrated photo-conducting diamond (PCD)[14] "flat response" detector. Figure 6 shows detailed modeling of the LEH radiation flux made with LASNEX to be quite close to the experiment throughout the pulse; the experimental peak being about 7% higher than simulation. Similarly, Figure 7 shows a propane-filled scale 0.75 hohlraum irradiated by ps22 compared with both French and U.S. simulations. The propane fill corresponded to a fully ionized density ~1.8×10^{21} electrons/cm^3 or ~$0.2n_c$, where n_c is the critical density. The hohlraum was irradiated by 10 smoothed beams (KPP only, no SSD). The performance of this relatively high-energy-density, gas-filled hohlraum, which achieved 260 eV, is very close to both FCI-2 and LASNEX.

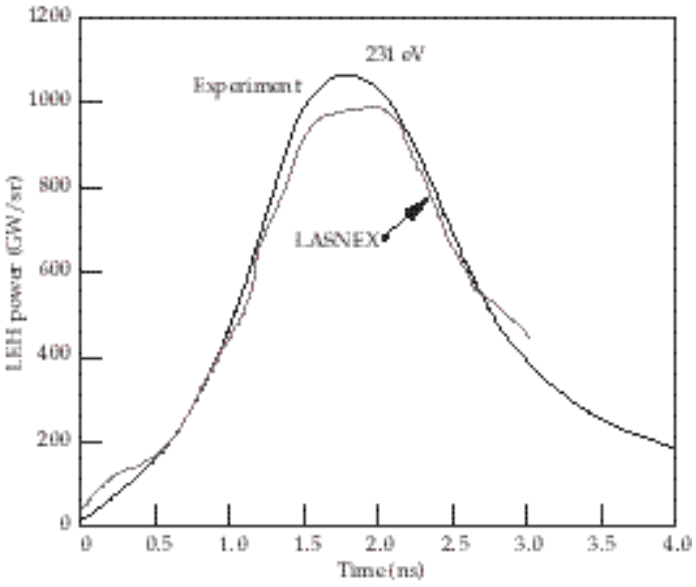

FIGURE 6. LEH drive measurement and modeling for a Nova methane-filled hohlraum irradiated by ps26. (50-00-0199-0090pb01)

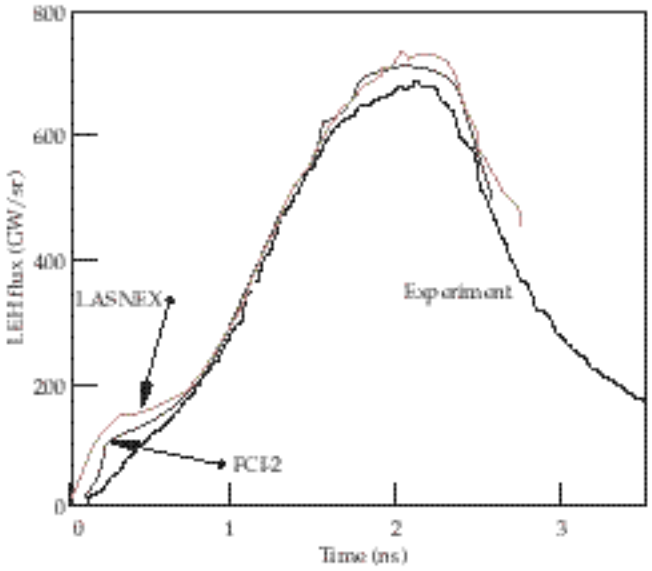

FIGURE 7. Scale 0.75 ps22 propane hohlraum. Both FCI-2 and LASNEX agree with one another and with the data. (50-00-0199-0091pb01)

Finally, Figure 8 plots the LEH flux per square centimeter from three of the most extreme hohlraums we have shot. It demonstrates detailed, quantitative understanding of drive that spans two orders of

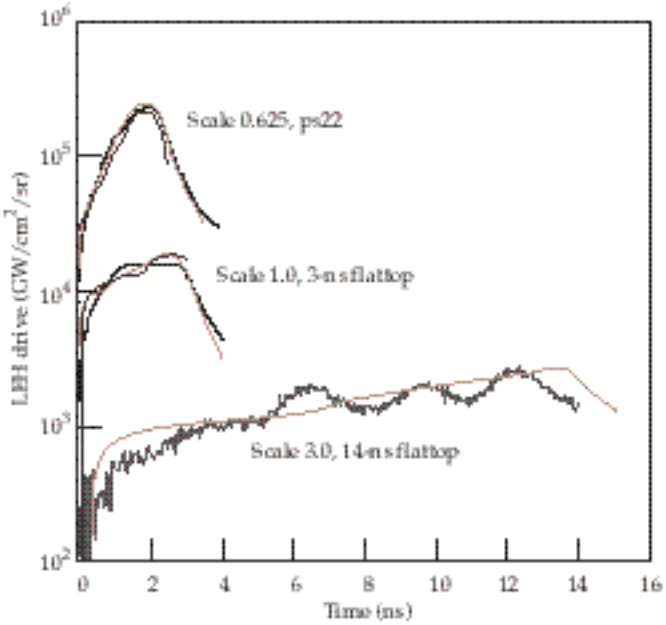

FIGURE 8. LEH measurements (GW/cm^2/sr) and modeling from three very different types of experiments. The upper curve is from a scale 0.625 hohlraum irradiated with ps22. The middle curve is a scale 1.0 hohlraum irradiated with a 3-ns flattop. The lower curve is a scale 3.0 hohlraum irradiated with a 14-ns pulse constructed by sequentially firing eight of Nova's ten beams. (50-00-0199-0092pb01)

magnitude in radiation flux/cm^2/sr. The upper curves show experiment and simulation for a scale 0.625 vacuum hohlraum irradiated by ps22. It achieved a peak T_r of ~283 eV. The middle curves plot experiment and simulation for a scale 1.0 hohlraum irradiated by a 3-ns flattop. FCI-2 and LASNEX have modeled both of these experiments and, as is shown, agree very well both with each other and with the measurements. Finally, the lower curves are the LEH drive from a scale 3.0 hohlraum irradiated by 1.9 TW for 13.5 ns. Once again there is excellent agreement between experiment and simulation. The rolling nature of the data in the lower temperature hohlraum is explained by Nova's beams being fired sequentially in order to produce this long pulse shape, instead of simultaneously.[18] This rolling cannot be included in our axisymmetric 2D modeling.

We have used LASNEX and FCI-2 to simulate, in detail, a wide variety of experiments. Examination of our entire collection of data leads us to estimate that LASNEX reproduces LEH measurements of time-dependent $T_r(t)^4$ to 4%±7%. By this we mean that the experimental $T_r(t)^4$ measurement will typically be contained within a band constructed by taking $1.04 \cdot T_{Lasnex}(t)^4 \pm 7\%$. However, the absolute calibration uncertainty of our principal x-ray flux diagnostic[19] is ±10%. Adding this in quadrature to the ±7% leads us to conclude that the true $T_r(t)^4$ will be 1.04±0.12 of LASNEX's $T_r(t)^4$.

Given this, we conclude that for a given capsule area and albedo, an ignition hohlraum's $\eta_{CE}\ \eta_{HR\text{-}cap}$ will be ~1.04±0.12 of coupling predicted by our simulations. Applying that to the NIF point design gives an estimated coupling of 0.115±0.012.

Discussion

Over the years various researchers have frequently speculated that hohlraums will begin to fail at $0.1n_c$. This has been based on the pessimistic assumption that laser plasma instabilities will necessarily wreak havoc with the intense laser beams at densities higher than this. However, pulse-shaped, reduced-scale hohlraums, such as the 0.625 scale that provided the upper radiation flux plot of Figure 8, are part of a database that belies this assumption. For example, Figure 9 plots electron density contours at 2 ns from a simulation of the scale 0.625 hohlraum. At this instant, which is the time of peak radation drive, simulations indicate that the plasma density inside the hohlraum is everywhere greater than $0.2n_c$. Indeed, most of the plasma volume traversed by the laser would appear to be $n_c/4$ or higher. In spite of this, the hohlraum radiation flux appears to be in very good agreement with expectations indicating that the hohlraum is working well. Moreover, the measured backscattering is relatively low; the time integrated SBS + SRS being <10%.

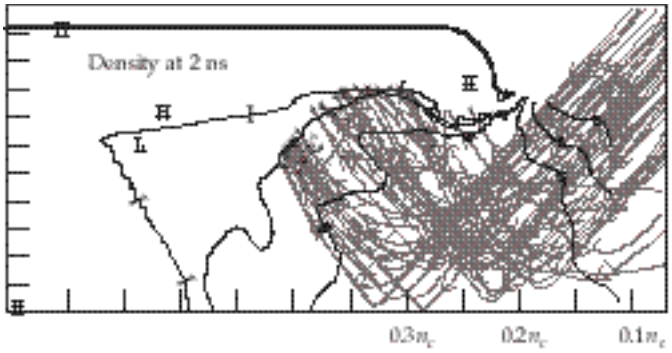

FIGURE 9. The scale 0.625 hohlraum of Figure 8 filled to relatively high plasma density by 2 ns. Nevertheless, the drive measurement indicates that it is performing as expected. (50-00-0199-0093pb01)

That hohlraums continue to operate properly, even when very filled with plasma, coupled with low backscatter losses with 10 smooth beams, has allowed us to greatly exceed performance goals set for us by the National Academy of Sciences in their Nova Technical Contract (NTC). The NTC called for temperatures >210 eV in pulse-shaped, "advanced" (e.g., gas-filled) hohlraums and >230 eV in vacuum, pulse-shaped hohlraums. Figure 10 compares predicted peak temperatures with measured peak temperatures for our database of pulse-shaped hohlraums shot from

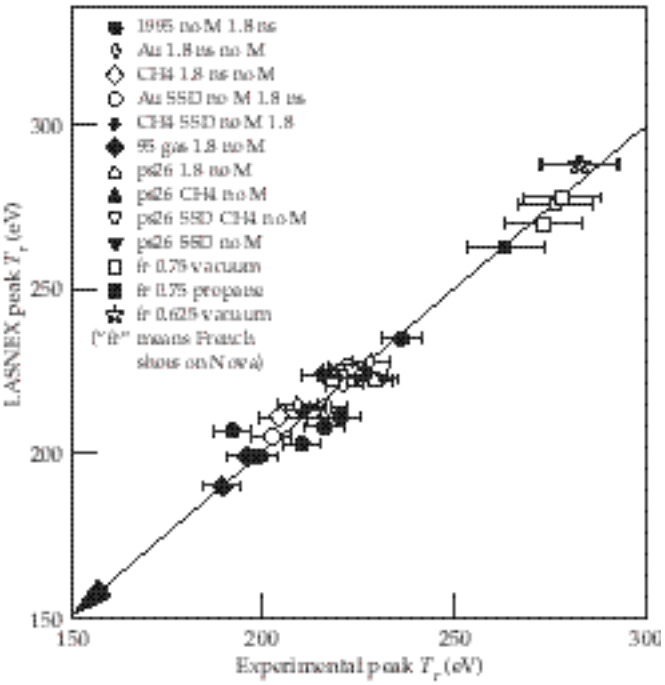

FIGURE 10. Comparisons of predicted peak temperatures with measured peak temperatures for our database of ignition-relevant pulse-shaped hohlraums shot from 1995 through 1998. (50-00-0199-0094pb01)

1995 through 1998. The NTC goals were laid out in 1990 and, at the time, were considered quite challenging. Our recent experiments very significantly exceed the NTC requirements, underscoring the technical progress we have made since that time.

The close agreement between simulation and experiment after the peak of the laser pulse provides validation of one important aspect of simulations: the way in which hohlraums manifest energy conservation at later times. In a long-pulse hohlraum, considerable thermal energy can be stored in the hot corona blowoff that fills it. After the peak of the laser pulse, this blowoff can cool, converting the released thermal energy to radiation. The later time release of stored plasma energy is a noticeable part of Nova-scale energetics and an even more important part of larger scale ignition hohlraum energetics. Without it, significantly more late-time laser power would be needed to maintain the desired radiation temperature.[8,9]

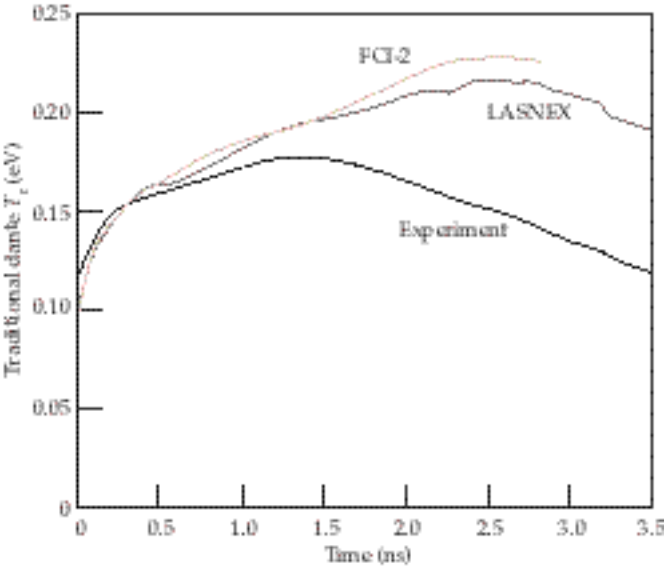

FIGURE 11. Traditional dante measurement of radiation temperature from a 3-ns BAP experiment compared with modeling. (50-00-0199-0095pb01)

Validating the LEH Line of Sight

In 1997 we performed a compelling series of experiments which demonstrated that in situations where there is gross disagreement between traditional dante and modeling, the LEH line of sight indicates that the hohlraum is in fact performing as expected. This sequence of experiments provided the strongest evidence to date that there is something wrong with the traditional dante line of sight later in times, when the hohlraums fill with plasma (more precisely, after the time at which wall blowoff stagnates on axis, thereby ending the hohlraum's free-expansion phase). This "build-a-pulse" (BAP) experimental series consisted of scale 1.0 vacuum hohlraums with 75% LEHs irradiated with flattop laser pulses that varied from 0.6 ns to 3 ns. The dante holes themselves were the standard "Be-washer" type.[7] For example, Figure 11 plots the observed and simulated traditional dante flux vs time for a hohlraum irradiated by a 3-ns flattop. It is quite evident that after ~1 ns, there can be extraordinary disagreements between this measurement and modeling with both codes. For very filled systems like this, the disagreement can be far worse than we typically saw (cf Figure 2). In this case there is approximately a factor of three difference in integrated flux. In contrast, the drive measurements made through the LEH on all these experiments (e.g., the middle curves of Figure 8 show the 3-ns BAP experiment and modeling) were very much closer to our expectations throughout the pulse and even after the pulse.

The gross difference between findings from the two views quickly led to the LEH line of sight becoming the preferred drive diagnostic for virtually all experiments. However, we were quite concerned that just because the results are close to our expectations, it does not guarantee that they are right. For example, one could construct a pathological situation that could make the LEH drive seem "right" yet still starve the center of the hohlraum of radiation. This scenario combines lower than expected radiation production with greater than predicted plasma evolution. This could conspire to move the weaker source close to the LEH, where it would look bright but no longer effectively heat the center of the hohlraum.

In an effort to validate that the central temperature in a hohlraum really is close to modeling, we performed two types of experiments. The first type was to measure the burn-through time of thin gold foils covering holes in the center of a hohlraum. The thicknesses were chosen so that the burn-through times would readily distinguish which of two grossly different drives was more likely correct. These burn-through measurements were part of our second series of BAP experiments. We observed burn-through signals on four of six foils placed on the hohlraums (no signals were seen on two foils which were thick and should have been weak). The burn-through times of the four foils is consistent with simulated drive (which, for these hohlraums, is very close to the simulated LEH drive). Figure 12 plots expected burn-through time against observed burn-through time. The expected times were calculated by a 1D LASNEX simulation using STA opacities.[20] The simulated foils were driven with multifrequency radiation sources extracted from LASNEX simulations of each experiment. The close agreement between observed burn-through time and simulated burn-through time is further evidence that hohlraums, at late-time, are performing approximately as modeled. This, in turn, is evidence that the LEH

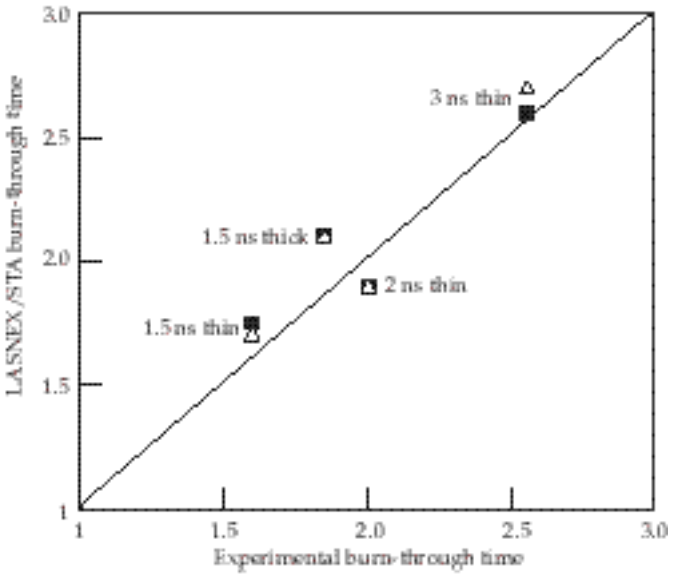

FIGURE 12. Burn-through foil measurements made on BAP hohlraums are consistent with drive measurements made through the LEH and with simulation. (50-00-0199-0096pb01)

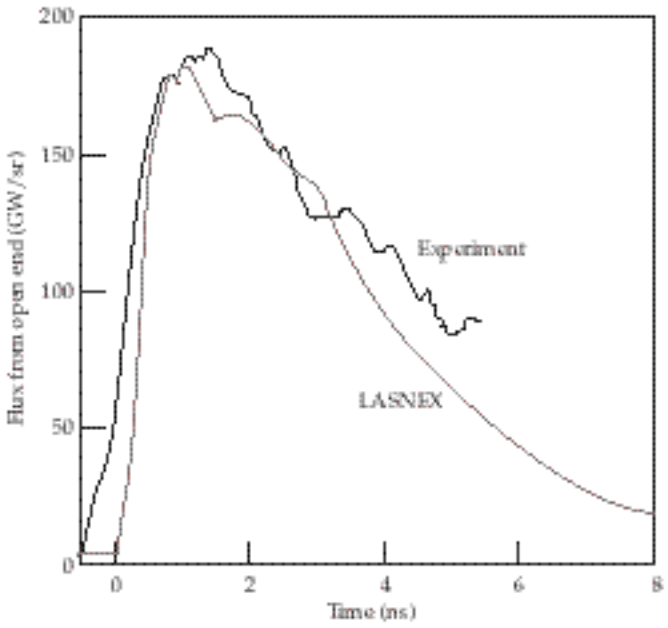

FIGURE 13. Radiation flux emerging from the midplane of a half-hohlraum irradiated by a very long pulse. This indicates that a real hohlraum midplane will not see a radiation flux that is significantly different than that expected from radiation hydrodynamic simulations. (50-00-0199-0097pb01)

line-of-sight provides a valid measure of late-time drive while the traditional-dante line of sight may not.

Complementing the burn-through measurements, we also have made a few measurements on "half-hohlraums." The basic idea is to cut a hohlraum in half, irradiate it through only one end and use the "LEH" drive diagnostic to measure the x-ray emission through the open, unirradiated end. If the open end of the hohlraum were, in fact, being starved of radiation at later times, then it should be very evident in the LEH drive diagnostic. Figure 13 is a comparison of simulated and measured radiation flux vs time from a scale 1.41 hohlraum irradiated by an 8-ns-long drooping pulse. In the simulated hohlraum, there is a large amount of plasma evolution that progressively moves the laser deposition region closer to the LEH throughout the pulse. Nevertheless, the flux exiting the midplane of this half-hohlraum is quite close to what we expect, indicating that in this very long-pulse system the center of the hohlraum is not "starved" of radiation but is, in fact, receiving close to the expected amount.

Notes and References

1. J. T. Hunt et al., *A Design Basis for the National Ignition Facility*, Lawrence Livermore National Laboratory, Livermore, CA, UCRL-JC-117399 (1994).
2. M. Andre, M. Novaro, and D. Schirmann, "Technologie pour un Laser Megajoule," *Review Scientifique et technique de la darection des applications militaires, Chocs*, Numero 13, 73, April, 1995.
3. See, for example, *The Physics of Laser Plasma Interactions*, by W. L. Kruer, Addison-Wesley Publishing Co., ISBN 0-201-15672-5 (1988).
4. S. W. Haan et al., *Phys. Plasmas* **2**, 2480 (1995).
5. W. J. Krauser et al., *Phys Plasmas*, **3**, 2084 (1996).
6. B. J. MacGowan, R. L. Berger, et al., *Laser Beam Smoothing and Backscatter Saturation Processes in Plasmas Relevant to National Ignition Facility Hohlraums*, submitted to the proceedings of the 17th IAEA Fusion Energy Conference, Yokohama, Japan (October, 1998).
7. R. L. Kauffman et al., *Phys. Rev. Lett.* **73**, 2320 (1994).
8. L. J. Suter et al., *Phys. Plasmas* **3**, 2057 (1996).
9. R. Siegel et al., *Phys. Rev. A* **38**, 5779 (1988).
10. J. M. Soures et al., *Phys. Plasmas*, **3**, 2108 (1996).
11. S. H. Glenzer et al., *Phys. Rev. Lett.*, **80**, 2845 (1998).
12. B. J. MacGowan et al., *Phys. Plasmas*, **3**, 2029 (1996).
13. C. Decker et al., *Phys. Rev. Lett.*, **79**, 1491 (1997).
14. R. E. Turner et al., *Rev. Sci. Inst.*, **70**(1), 656 (1999).
15. R. L. Kirkwood, Lawrence Livermore National Laboratory, Livermore, CA, private communication (1996).
16. S. N. Dixit et al., "Kinoform Phase Plates for Tailoring Focal Plane Intensity Profiles," *1994 ICF Annual Report*, UCRL-LR-105820-94 (1994).
17. S. Skupsky et al., *J. Appl. Phys.*, **66**, 3456–3462 (1989).
18. O. L. Landen, Lawrence Livermore National Laboratory, Livermore, CA, private communication (1996).
19. H. N. Kornblum and R. L. Kauffman, *Rev. Sci. Inst.*, **57**, 2179 (1986).
20. A. Bar-Shalom, J. Oreg, and W. H. Goldstein, *Phys. Rev. E* **51**, 4882 (1995); A. Bar-Shalom, J. Oreg, W. H. Goldstein, D. Shvarts, and A. Zigler, *Phys. Rev. A* **40**, 3183 (1989).

NOVA/BEAMLET/NIF UPDATES JULY–SEPTEMBER 1998

R. Ehrlich/P. Wegner/S. Kumpan

Nova Operations

Nova Operations performed 256 experiments during this quarter, which was enough to exceed the goal of 900 experiments during FY98. These experiments supported efforts in ICF, Defense Sciences, university collaborations, Laser Science, and Nova facility maintenance.

While continuing to make minor improvements to the capabilities of Nova, we began the process of planning the decommissioning of the Nova facility during the upcoming fiscal year. Nova will be shut down to make room in Building 391 for National Ignition Facility (NIF) Project activities. Some of the laser components from Nova will be reused in the NIF facility; the remaining components will be made available for use at other facilities.

The operation of the Petawatt Laser Project was substantially improved with the installation of a set of mirrors that allows beamline 6 to bypass the 46-cm amplifiers without physically removing them from the space frame. This saves several hours during the process of converting that beamline to and from the Petawatt configuration, allowing Nova to use beamline 6 for Petawatt shots and ten-beam target shots during the same day. Also during this quarter, we initiated the installation of hardware required for a campaign of cryogenic ten-beam target shots, which are among the 585 experiments planned for next year.

Beamlet Operations

The fourth quarter of FY98 saw Beamlet complete its mission as laser physics and engineering test bed for the National Ignition Facility (NIF). The last Beamlet shot was fired on July 31, capping a highly productive four-year period of NIF laser technology and component development activities, including over 1000 full-system shots in over twenty experimental campaigns since its activation milestone in September 1994. In the first month of this quarter, 46 shots were completed in two campaigns: (1) large-aperture damage testing of a polarizer and mirrors for the French Commissariat a l'Energie Atomique (CEA) and (2) high-energy operation of a NIF-like final optics configuration at 3ω (the third harmonic). Shutdown activities commenced immediately thereafter.

The damage testing of the CEA polarizer was conducted with "p" polarized light at a beam size of 34 cm. The polarizer was conditioned off-line prior to the test. Minor damage sites a few hundred microns in size were observed after the first shot at an aperture-averaged fluence of 1.9 J/cm^2 in a 9-ns square pulse. This was the only damage observed, however, and it did not grow on subsequent shots at fluences up to 11.9 J/cm^2. Two CEA mirrors were also damage tested. One of the mirrors was unconditioned and the other had two levels of conditioning applied in different regions of the aperture. Both mirrors were exposed to aperture-averaged fluences of 20 to 30 J/cm^2 in 3-ns square pulses, which was achieved by positioning the mirrors 3.5 m downstream of the Beamlet final focus lens at a beam size of 17.8 cm. The only damage occurred midway through the testing of the first mirror and was caused by contamination.

The high-energy tests of NIF prototype final optics achieved third-harmonic fluences of up to 8 J/cm^2 and NIF-equivalent energies of up to 9.6 kJ in 3-ns square pulses. The purpose of the test was twofold: (1) to validate the design of the NIF final optics cell (FOC) at high fluence and (2) to operate an integrated NIF-like final optics package, including diffractive optics, to obtain data for estimating component lifetimes on the NIF. Tests of the FOC alone confirmed that it can be operated at full fluence without the large-area damage previously observed and attributed to a mismanaged back reflection. Isolated damage was observed, however. Results of the integrated tests revealed problems

with color-separation–grating (CSG)-induced beam modulation and damage associated with the sol-gel coating being nonconformal with the grating—an effect previously identified as being responsible for reducing CSG diffraction efficiency. Improved CSG designs under development are expected to eliminate this problem.

Disassembly of the Beamlet Facility began on August 3. Approximately two-thirds of the laser was designated to be shipped to Sandia National Laboratories (SNL), New Mexico, for use as a backlighter on the "Z pinch" facility. The remaining one-third was packaged and turned over to various groups of the NIF Project. The disassembly was completed by October 1, and the facility was turned over to Lawrence Livermore National Laboratory's (LLNL) Plant Engineering Directorate for transition to the NIF Frame Amplifier Unit Assembly Area. Over 350 crates were shipped to SNL, varying in size from 2 ft square to the largest crate containing the front-end frame which was 7 ft tall, 8 ft wide and 51 ft long and weighed ~18,000 lbs. The large amplifiers are still on site, in storage, awaiting clean disassembly and eventual transfer to SNL.

National Ignition Facility

Overall Assessment

Overall progress on the NIF Project remains satisfactory for the fourth quarter of FY98. The current top-level assessment of Project status remains similar to that stated at the end of the third quarter 1998; that there will be no change to the fourth quarter 2001 Level 2 milestone for the End of Conventional Construction, nor to the fourth quarter 2003 Project Completion date. However, the NIF Project Office now anticipates that based upon the status of Conventional Facilities, CSP-4, work on the Laser Bay Core and the status of Special Equipment design and procurement, there could be an impact of 6 to 8 weeks in the fourth quarter 2001 completion of the Level 4 milestone for start-up of the First NIF Bundle. The impact of current field conditions on this important milestone, which is to be completed in three years, continues to be evaluated on a weekly basis at the Project Top Ten Scheduling meeting.

For NIF Conventional Facilities, fourth quarter 1998 was a period of relatively high productivity. Work completed in the field progressed from 17.5% at the end of June to over 28% by the end of September. Efforts on the site rapidly accelerated as the average manpower on site increased to over 180 and will approach 300 by the end of the first quarter 1999. The structural steel erection, bolting, and plumbing has been completed for the Laser Bays and Core sections, and roofing and siding is in process, but the progress on critical interfaces to CSP-9 is approximately eight weeks behind schedule. Efforts to accelerate the Laser Bay steelwork during the fourth quarter 1998 did not materialize due to labor difficulties with the ironworkers, but the Laser and Capacitor Bay areas will be sufficiently "dried-in" prior to the start of the rainy season. The concrete walls have been poured to about ground level in the Target Area and Switchyards, and installation of the Target Chamber on its pedestal is on schedule for March of 1999. The Optics Assembly Building (OAB) structural steelwork is complete and is generally on schedule.

In Special Equipment, at the end of the fourth quarter the Mid-Title II (65%) Design Reviews were 93% complete, and final Title II (100%) Design Reviews were 60% complete. There were four Special Equipment Title II (100%) Design Reviews planned for FY98 that remain to be completed in the first quarter 1999. Design closure and drawing production were slower than planned, but critical path designs were generally on schedule. Major awards have been made for the spatial filter vacuum vessels and vacuum beam tubes, the Laser Bay structures, and for the Switchyard 2 structural steel tubing.

In Optics, facilitization was in final stages at most vendors as they started or prepared to start pilot in early FY99. All laser glass contracts were either in place or will be placed at the beginning of the new fiscal year. Nd was in hand at both Schott Glass Technologies and Hoya Optics for their pilots. Potassium dihydrogen phosphate (KDP) rapid-growth facilitization at Cleveland Crystals, Inc. (CCI) and Inrad has gone well, and they have made excellent progress growing their first crystals, up to 27 cm in size. Corning was nearing completion of facilitization. The accelerated fused silica pilot was awarded early in September and has begun. Tinsley continued to make excellent progress on their finishing facility, and they demonstrated outstanding performance with the first four lenses, which will be used on the NIF first bundle. Zygo was making good progress with their facility, including resolution of the pitch problem discussed in previous reports and initial hiring for pilot production. The University of Rochester Laboratory for Laser Energetics (UR-LLE) and Spectra-Physics continued to make good progress preparing for their pilots.

Key Assurance activities during the fourth quarter were all on schedule, including construction safety support, litigation support to the Department of Energy (DOE) for the settlement of 60(b) (e.g., quarterly reports), and the *Final Safety Analysis Report*. The *Pollution Prevention and Waste Minimization Plan* was completed in August, one month ahead of schedule, achieving a Level 2 DOE milestone.

There were 39 DOE/OAK Performance Measurement Milestones due in the fourth quarter,

and 33 were accomplished. There were a total of 95 milestones due through the end of FY98, and 85 have been accomplished.

Site and Conventional Facilities

The fourth quarter of FY 1998 was a period of high productivity for NIF Conventional Facilities. Work completed in the field progressed from 17.5% at the end of June to over 28% by the end of September. Efforts on the site are rapidly accelerating as the average manpower on site has increased to over 180 and will approach 300 by the end of the first quarter 1999.

Bolting the core steel was the main focus on the Laser Building so that as much of the deck as possible could be released to CSP-9 to allow for rough-in and concrete placement to start in September. Bolting and plumbing of Laser Bay 1 lagged due to the lack of ironworkers, but by the end of September, the entire crew completed work on the core and started work on Laser Bay 1, which should be completed during the month of October.

Roofing operations started in September and made significant progress. In the three-week time frame that the roofing subcontractor worked, the entire Laser Bay 2 roof was dried-in along with nearly half of the Laser Building core area. The roofing subcontractor accelerated its schedule to complete all the roofing on the Laser and Target Area Building (LTAB) in an eight-week time frame.

A primary focus of work for October will be to continue to "dry-in" the building and to protect the site to the fullest extent possible from the upcoming winter weather. The site storm drainage system has been completed and is ready to receive runoff from the Laser Building and OAB roof drains. The Target Building will not have the roof constructed and will be open to weather this coming winter. Regrading and surface treatment of the site to allow for proper drainage will occur in October to permit access and laydown through the coming winter. *Storm Water Pollution Prevention Plan* requirements are scheduled to be completed during October. The *NIF Site Winterization Plan* will be reviewed by wet weather specialists, EarthTech, and finalization of the plan will occur in October.

- FY98 DOE/OAK Performance Measurement Milestones completed this quarter included: "OAB Start Structural Steel Erection," achieved in June; "Laser Bays: Complete Structural Steel Erection," completed in August; and "Power Available," completed in August.
- Nielsen Dillingham (NDBI) completed erection of structural steel for the OAB Corridor and is substantially complete with all steel erection for CSP-4 Phase I.
- Activities increased in the OAB in September as more trades manned the site. Midstate Steel nearly completed their work, including the roof truss punch list. Magnum Drywall mobilization occurred in September; they installed studs around the perimeter of the building and, by the end of the quarter, were ready to start sheathing installation (see Figure 1).
- Work by CSP-6/10 continued in all four areas of the Target Building. The target pedestals have been constructed up to the ring at elevation –8'-9" (see Figure 2). The radius wall up to elevation –3'-6" is formed on one side with rebar, and embed/blockout installations are nearing completion. The radius wall pour from elevation –21'-9" to –3'-6" is taking longer than expected, but the complexity and need for precision of the blockouts and embeds is very critical. This pour and the similar one higher up on the radius wall from elevation 48'-0" to 68'-3" are the most difficult pours on the project; therefore, the extra time required to assure they are correct is justified. Despite the extra time used, the milestone for installation of the Target Chamber has not slipped. The first lift for Switchyards 2 and 1 walls up to elevation 3'-6" have been completed on all three sides. Forms for walls in Switchyard 2 are being jumped for the next lift in October. The south wall of the Diagnostics Building basement was placed in September. Currently, CSP-6/10's schedule meets the critical milestone dates for installation of the Target Chamber and Switchyard structures.
- The bulk of the Site Utilities scheduled for this year were completed in the fourth quarter by

FIGURE 1. Installation of metal studs in the OAB.
(40-60-0998-1855#11)

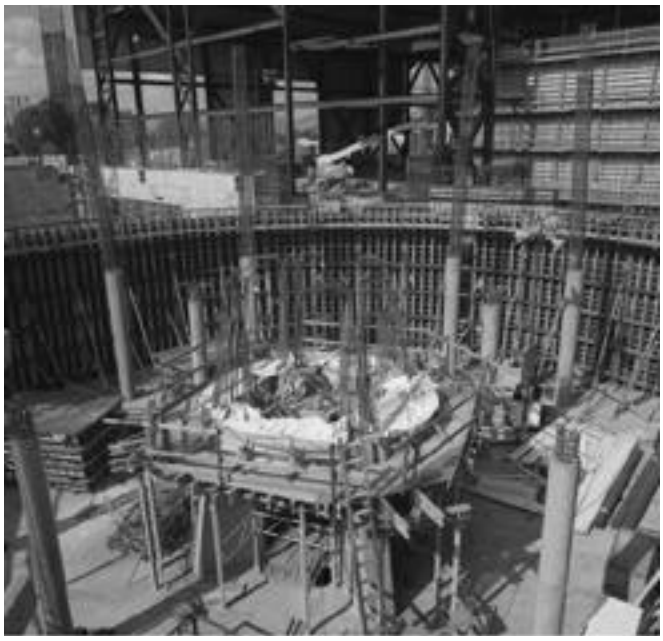

FIGURE 2. Shoring and forming for the target bay pedestal. (40-60-0998-1942#08)

Hensel Phelps (HPCC). The Site Utilities are continuing (but are winding down): including installation of temporary / permanent duct-banks around the OAB, south side of the site, and sectionalizing switches and vaults north of CB4. Complete installation of the storm drain system will occur in October. In addition, HPCC completed erection of Central Plant structural steel as well as completed forms, reinforcing, and placement of Cooling Tower walls. The placement of concrete on the metal deck was completed for parts of Core Areas "A" and "B" elevations 28' and 47'-6". Within LB2 and CB4, HPCC began installation of underslab precast duct in LB2 and began installation of underslab conduit in CB4. The installation of LB2 overhead platform up to Column Line 24 was completed and HPCC began installation of mechanical, fire sprinkler, and electrical rough-in off of the platform. Work by CSP-9 in the core area was under way at both mezzanine levels. CSP-9 overhead rough-in work in Laser Bay 2 (utilizing the overhead platform) was off to a good start and progress appeared to be at or above the originally scheduled pace.

Special Equipment

Design Reviews continued to be successfully held at both the Mid-Title II (65%) and final Title II (100%) design levels. Design closure and drawing production were slower than planned, but critical path designs were on schedule. Awards were made for the Laser Bay structures.

During the fourth quarter, many of the Special Equipment Title II Engineering activities were brought to an end. Title II 65% Design Reviews were held for the OSECS Safety Interlock and Video Surveillance System and for the Transport and Handling System. The final (100%) Design Reviews were held in July and August for the Alignment System, Pockels Cell, the Mechanical Utilities, the Optical Design, the Gas Handling System, the Laser Auxiliary System, and the Safety System. Ten final (100%) Design Reviews were conducted in September, including Final Optics Damage Inspection / Pulse Synchronization, Output Sensor / Relay Optics, Optical Mounts, Target Positioner, Target Area Structures, Main Laser Alignment, Optical Pulse Generation, Power and Back Reflection Sensor / 3ω Energy / Portable Sensor / Energy Diagnostics / Power Diagnostics, Target Chamber Vacuum, and Laser Amplifier. Final Documentation Reviews were held for the Switchyard 2 Support Structures Procurement Documents, the Switchyard Tube Enclosures Design and Procurement, and for the Laser Bay Support Structures Concrete Pedestals.

Laser Systems. The optical pulse generation (OPG), plasma electrode Pockels cell (PEPC), and amplifier subsystems each held well-received 100% Title II Design Reviews during the fourth quarter. The fabrication drawings are now complete, or nearly so, in each of these areas. The emphasis is now shifting to procuring and assembling hardware for the first bundle. In the Power Conditioning area, assembly of the First Article module essentially realized the baseline capacitor bank design for the NIF. Over 1000 shots were accumulated at full NIF current levels.

- The OPG 100% Title II Design Review was completed in September. This milestone represented a shift in the team's focus from design to procurement and fabrication. The current plan calls for an integrated test of the OPG hardware in Building 381 prior to reinstallation in the LTAB. A major focus of the OPG team during the past quarter has been identifying and testing a distributed feedback (DFB) oscillator connected to a high-gain fiber amplifier to provide the required input pulse to the master oscillator fiber distribution system. DFB oscillators from two vendors were evaluated and both demonstrated excellent single-mode operation. The requisite power and noise levels were achieved using a high-gain, double-pass fiber amplifier. Testing of the Stimulated Brillouin Scattering (SBS) fail-safe circuit (intended to prevent propagation of a pulse with inadequate bandwidth to prevent SBS) began during the last quarter and produced encouraging results. A new circuit approach in

the arbitrary waveform generator was tested and was shown to reduce the electrical noise to a level consistent with meeting the stability requirement during the "foot" of the Haan pulse shape. This change allows the vendor to proceed with the final design of the pulse shape generator for the NIF. The prototype preamplifier module demonstrated all of its key performance requirements including energy and phase error during this quarter, adding substantial credibility to the design.

- The 100% Title II Review of the Amplifier was held as scheduled in September. The 13-volume Amplifier design basis book was prepared, reviewed, and submitted to the NIF document center. Approximately 95% of the drawings of the Amplifier components were submitted to the NIF Project Database Management system, and approximately 30% of the assembly, interface, and assembly equipment drawings were completed. All interface control documents were completed and are under configuration control, though some will be modified as the interfacing system designs evolve. Approximately 75% of the supporting calculations were completed, and many but not all of the design implementation plans were prepared. The failure modes and effects analysis and reliability, availability, and maintainability analyses were updated for Title II. A 700-shot cleanliness test was completed using the AMPLAB amplifier. The results indicated that damage growth on a slab in the amplifier is consistent with achieving the recently modified operational contamination damage levels proposed by the Project Scientist (beam obscuration <1% and no damage site larger than 1 mm). This result indicates that NIF contaminant levels can be achieved at installation and that in operation, the slab damage levels are within acceptable replacement limits.
- The PEPC subsystem also completed a very successful 100% Title II review during the fourth quarter. There were very few action items generated by the reviewers, and responses have been completed for all of them. All of the mechanical drawings for the PEPC subsystem are complete, and the procurement process is under way at an aggressive pace to attempt to benefit from a slack period for machine shops that traditionally support Silicon Valley companies. During the past quarter, the emphasis was on demonstrating acceptable switching performance over a 100-ns time window to enable appropriate timing of target backlighter beams. The requirement was met after minor modifications to the switch pulse termination resistors to sharpen the rise and fall times of the pulse, effectively broadening the "in spec" portion of the pulse. Control system software testing has begun in the prototype laboratory to demonstrate proper controls operation and robustness for operation in the Pockels cell electromagnetic interference environment.
- The NIF First Article capacitor module was assembled during the fourth quarter. Roughly 1000 full-current shots were completed, and the lifetime of the switch under NIF-like operating conditions is consistent with predictions. Late delivery of the flashlamp load, coils, and cables consistent with the baseline design resulted in the use of the old prototype parts for these initial tests. Therefore, the waveshape and charge voltage are not yet representative of the NIF. Module operation consistent with the amplifier requirements is planned for the first quarter of FY99. An environmental, safety, and health (ES&H) review of the module design and operation concluded that the gaseous effluent from the switch contains sufficient ozone and nitrogen compound levels that an outside exhaust vent is needed. The noise level and other safety-related controls were found to be acceptable.

Beam Transport System. In this quarter, major fabrication contracts were awarded, mill order material was shipped, and production of Laser Bay structures and vessels was ramped up after completion of shop drawings and quality assurance submittals. Shop operations during this period included welding fixture fabrication, plate cutting, and structural member preparation. These 11 contracts are currently on schedule to meet the installation milestones.

The Beam Transport System acquired government excess material-handling equipment for upcoming installation activities, including an Oshkosh diesel prime mover, a 45-ton Taylor forklift, and a 60-ton capacity battle tank trailer. These assets are now at LLNL for the cost of shipment and are fully operational.

Laser Bay concrete structure and Switchyard 2 structure design drawings were released for construction change order quotations from the existing Conventional Facilities contractors. The mill order for Switchyard 2 tube steel was awarded in August. Auxiliary Subsystems completed the Title II Design Reviews for the Gas Handling System, Amplifier Cooling System, and Conventional Utilities. All amplifier cooling fan units have been received and are currently stored in the laydown area awaiting installation into the LTAB. Other activities include the following:

- Production of the stainless steel plate neared completion. Vacuum vessel fabrication activities are proceeding with the three selected contractors. Two contractors completed preliminary

documentation, and their fabrication activities are proceeding on schedule. Fabrication plans and procedures are being reviewed and revised with the third contractor to ensure compliance with the specifications and drawings.

- The drawing packages for the Switchyard 2 beam tube enclosures are complete, and the procurement requisition is prepared and submitted for request for proposals (RFP) release. The specification for the Switchyard and Interstage Beam Enclosures was updated and revised, incorporating design review comments and other recommended changes learned during ongoing fabrications for the vessels and beam tubes.
- The Airlock/Sliding Door feature of the Roving Enclosure was removed to reduce costs. Roving Enclosure design will continue to include features that can accommodate future installation and conversion on a "Not to Preclude" basis.
- Design detailing is proceeding on the interstage docking frames at the Spatial Filter (SF) end vessels. Engineering review and design checking remain to be performed. Design development and detailing is behind schedule on the large interstage components at the switchyard wall. These structures must be fabricated and installed into the Laser Building before closure of the facility holdouts.
- The Title II 100% Design Reviews for the Amplifier Cooling System, the BTS Auxiliary Subsystems, Gas Handling system, and the Mechanical Utilities, which included Fire Protection as well as Lighting and Power subsystems, were completed.
- The mill order for Switchyard 2 tube steel was awarded in August. The Title II 100% procurement review was held in preparation for the change order proposal solicitation from the CSP–6/10 contractor.
- The Cavity Spatial Filter Optical Bench, Transport Spatial Filter Optical Bench, Injection Structure, and Preamplifier Support Structure Safety Notes were completed. Contracts were awarded for the Main and Power Amplifiers, Laser Mirror 1 structures, Cavity and Transport Spatial Filter optics benches, Injection Structures, Preamplifier Support Structures, and Periscope structures.

  The Optical Mounts Title II 100% Review was held in September. Final designs were presented for spatial filter lens cassettes, the injection system, cavity mirror/polarizer mounts, shutter/beamdump, Switchyard transport mirrors, and Target Area transport mirrors.
- A full-size rectangular test mirror with "holes" drilled in the back was mounted and evaluated interferometrically (the mirror was tested vertically and in the down-facing orientation shown in Figure 3). This test is part of the validation plan for the transport mirror attachment concept and mount design. The preliminary results indicate that the observed distortion is less than predicted from finite-element analysis. The results to date indicate that the so-called "expanding mandrel" design will hold the mirror sufficiently well.

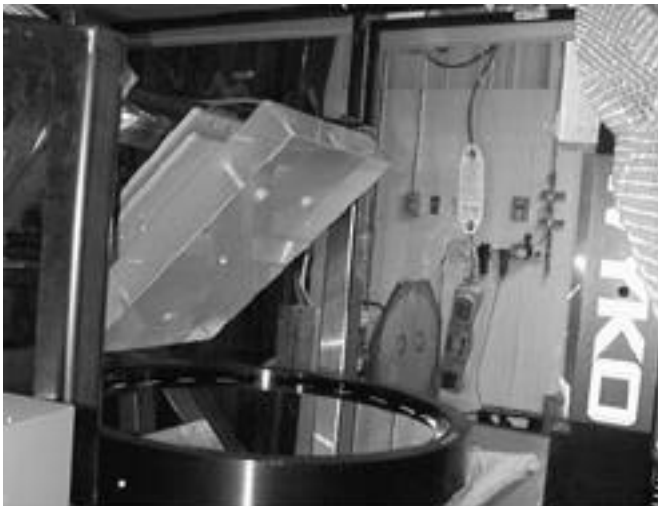

FIGURE 3. Transport Mirror Mount testing at use angle. (40-00-0199-0193pb01)

Integrated Computer Control System. Title II design progress is satisfactory. Seven out of a total of eight scheduled 100% reviews have been completed. Two reviews were completed during the fourth quarter: the Integrated Safety System and the Automatic Alignment System.

- At the end of September, the controls team accomplished the last of the FY98 Cost Account Plan milestones. These milestones, scheduled some fourteen months ago, were transformed into a much larger software delivery: the first integrated production prototype (code named Nightlight), consisting of incremental deliveries of 8 supervisory and 15 (out of 18) front-end processors (FEPs) (see Figure 4).

This prototype (the first of seven planned) had several major goals:

- Risk mitigation by early execution of important functions.
- Testing frameworks in actual use within applications.
- Gaining experience and confidence with software tools and engineering processes.

FIGURE 4. Nightlight software demonstration at the test bed operator console. (40-00-0199-0194pb01)

- Activating the independent software testing capability.

The theme of this first prototype was the vertical slice: the execution of initial functionality in each subsystem using either emulated or prototype hardware. Most slices included both supervisory and FEP functions; a few were limited to FEPs only. Almost all slices made use of the reusable frameworks upon which all controls software will eventually be built. Those that did not concentrated upon important application-specific behavior. In addition, significant new work was done on frameworks prototyped or designed earlier in the Project. Among these were the message logger, the sequence control language, the graphical user interface, the sample (or generic) application, and the shot life cycle.

To date, the vertical slices for target diagnostics, laser diagnostics, PEPC, integrated timing system, special imaging sensors, graphical user interface, and the sample application have been demonstrated—the first of three steps that certify completion of the software delivery: (1) demonstration to a project management team member, (2) placing the software under configuration control, and (3) independent testing of the software.

Due to the complexity and importance of the shot director and power-conditioning slice, its delivery has been delayed to the end of October. Because effort was redirected toward the graphical user interface portion of the sample application, the industrial controls vertical slice was also delayed to the end of October. The remaining slices are expected to be demonstrated in early October.

A major goal of Nightlight was validation of the distributed software architecture and the implementation process. While not every goal was achieved in this release, the important risks were successfully addressed and confidence was gained that the software needed to control the first bundle can be incrementally completed by repeating this process.

- The example supervisor software that will serve as a pattern for all eight NIF subsystems was constructed and tested. This demonstrates how the supervisory architecture is to be deployed and how each program is connected to the database, framework services for configuration, system manager, monitor, message logging, and graphical user interfaces. The new generic supervisor is analogous to the generic FEP that has been in use for several months. The new component adds a number of features needed by supervisor-level code: public and private internal objects for upper-level controls, communication with one or more graphical user interfaces, and bidirectional connections between distributed objects.
- Berkeley Nucleonics presented a satisfactory design review for the prototype Integrated Timing System delay generator in September. About 200 units are needed for the NIF. They have selected an acceptable optical receiver and are progressing on the basis that it will meet requirements, while also testing a discrete design intended to reduce propagation delay as a function of optical power level.

The version of the timing FEP for Nightlight is complete and delivered to the software test team. It consists of a computer crate containing actual NIF hardware, except that a similar 4-channel delay generator was substituted for the custom 8-channel NIF delay generator currently under development. The Nightlight FEP provides a complete vertical slice of the architecture using the supervisory frameworks (system manager, configuration server, generic FEP, and graphical user interface) to create devices for trigger channels, trigger diagnostics, and precise trigger diagnostics. The software provides the ability to set delays, enable / disable channels, create epochs and activate triggers as well as measure and read the resultant delay using two types of time interval meters. The release demonstrates integration under both Solaris and VxWorks operating systems.

- The 100% Design Review of the Integrated Safety System was conducted in July, and the Automatic Alignment 100% Design Review was presented in August. System operations for optics inspection were analyzed and documented in the *Preliminary System Analysis for the Damage Inspection Control System*. In summary, the inspection of vacuum-loaded optics in the

spatial filters and final optics assembly (FOA) will require slightly more than two hours. Amplifier cooling time and the brief target chamber center keep-out period extend the maintenance access time to as long as three hours following the shot. Inspection time is dominated by mechanical actions times. For example, repositioning the roving mirror assembly accounts for 24% of this time.
- Integration activities have concentrated on the project-wide tasks required to develop and test Nightlight. Preliminary planning also began on deployment of integrated software for the second production prototype ("Penlight") that will feature software operation and testing in the Preamplifier Module and input sensor prototype labs.

Optomechanical Systems Management. Title II 100% Design Reviews were held for Optical Design and Optical Mounts. Detail drawing checking and final approval is lagging in Optical Mounts (spatial filter lens cassettes have been completed; others are in creation or checking). The Title II Design Review for Final Optics was delayed about one month to allow for additional scientific evaluations of the final Beamlet campaign results. About 60% of the detail drawings for Final Optics are approved or in checking.

Optical Design. Design and analysis activity has been focused on completing the detailed optical design, manufacturing tolerances, and specifications for small optics subsystems (e.g., output sensor relays and preamplifier beam transport).

- The Optical Design Title II 100% Review was held in July. The presentation included the review for compliance, Main Laser system optical design, Switchyard/Target Area mirror system optical design, final optics optical design status, large-aperture optics specification and drawings, and stray light control.
- Some follow-up ghost analysis was conducted for the Main Laser, diagnostic system, and the final optics. In the Main Laser model, mechanical elements (e.g., beam tubes) were added so that the analysis of stray light paths could be completed. A worst-case target back reflection was modeled in the FOA to determine ghost fluences in the 3ω calorimeter chamber. A simplified model of the 1ω diagnostic system was constructed; a second-order ghost analysis provided useful feedback for the final optical design.
- The optical model for the FOA was completed; the configuration will be described in an upcoming revision of the configuration drawing. Final revisions included detailed ray tracing of the 1ω diagnostic reflection from the focus lens and transfer of optical design data to Pro-E.
- The "Small Optics Summit" was held in September. Representatives from 66 optics and optomechanics manufacturers attended this very successful one-day event. The morning session comprised presentations from the responsible engineers who will deliver line replaceable units (LRUs) containing small optics (≤150 mm diameter) to the NIF. In the afternoon, the vendors set up displays in a tent, allowing NIF Project and other LLNL personnel to come by and ask questions about the capabilities of each supplier of interest to them.

Optical Components. All NIF optics Title II Design Reviews were held in September except the KDP Crystals. The reviews focused on progress to date of facilitization at vendor sites and at LLNL and validated readiness to proceed with Title III and with pilot production.

The contract for 13.5 metric tonnes of Nd salts was negotiated and is ready to place early in October with FY99 funding. This will support the first production runs of laser glass for Hoya and Schott. The NIF Amplifiers (slabs), NIF Lenses, NIF Mirrors, NIF Polarizers, and NIF Windows 100% Title II Design Reviews were completed in early September. The NIF QA/Metrology and NIF Processing Title II Design Reviews were completed in early September as well.

Laser Control. Four Title II 100% Design Reviews were presented in August. Taken together, they covered Main Laser alignment, the output sensor package, the beamline to output sensor relay optics, final optics damage inspection, pulse synchronization, power sensors, the 3ω energy module, portable streak camera, back-reflection sensor, FEPs for energy diagnostics, power diagnostics, and special charge-coupled device sensors.

- The last of the input sensor drawings, namely the sensor assembly drawing and the test stand base plate and rails are now expected to be completed in October.
- Updated cost estimates for the beamline centering references were found to be higher than the plan, and efforts were made to simplify their implementation. A significantly less expensive approach to the centering reference on the FOA was identified.
- Optical design was begun for the spatial filter tower test stand that will be used for assembly and test in the OAB.
- Assembly of the Target Alignment Sensor hardware began. If performance meets expectations, this unit will be designated for use in the initial operation of the NIF.

- The number of FEPs was reduced in the plan from 108 to 100 to implement a decision removing motors from those mirror mounts in the Switchyard and Target Bay that are not part of the closed-loop control system.
- The optical alignment section of the acceptance test plan has been verified on the prototype. Other parts of the test plan, including motion tests of the motorized components, will be checked for suitability when the motor control electronics are added to the test stand.
- Efforts began to establish test capability for accurately measuring the reflectivity of 1ω sol-gel coatings in the 0.1% range. A preliminary capability was demonstrated using recent sample sol-gel samples.
- End-to-end tests of the power measurement instrumentation were completed in August. The results, which included a demonstrated precision of 1.5%, were documented during September and satisfy the appropriate part of the NIF power balance error budget.
- Disassembly of the precision diagnostics prototype systems in Beamlet was completed, and components were readied for storage.
- Tests on the LLNL deformable mirror prototype went very smoothly. The mirror clearly met the range specifications and showed a preliminary residual error of about 0.04 waves (rms surface) compared to the specification of 0.025 waves. The LLNL mirror is currently the only one of the three prototypes whose performance compares reasonably with NIF requirements; it will appear as the baseline for this review.

  The adaptive optic was identified as a high-risk system component to be reviewed by the Project Risk Management Group. This group will review test data, modeling results, and other aspects of deformable mirror status as a basis for recommending a plan to complete development activities.

Target Experimental Systems. All 18 sphere plates have had their weld joint configurations machined on the edges and the inside surfaces smoothed (grinding marks removed) and have been shipped to LLNL. The last three are en route. The first three plates were installed on a welding fixture inside the temporary enclosure and welded to form a subassembly. PCC moved from the machining of the sphere plates to the fabrication of the weld necks. All of the cylindrical pieces are completed and the flanges are now being welded to them.

- The 60-foot-diameter, 62-foot-high, cylindrical enclosure, built on the E7 parking lot, which is to be used for the construction of the target chamber, was completed. It is now being used for the welding of the first three sphere plates that form the bottom of the chamber. Yet to be installed is the HVAC for the building, planned for October.
- The chamber gunite shielding (hereafter known as shotcrete) design was reviewed by LLNL. An alternative design was proposed and analyzed by Project personnel. The result was a system that would provide shielding but not become a structural member (composite) with the target chamber. This simplified design was discussed with two potential shotcrete installers who felt it was a very workable installation. The system consists of wire mesh attached to the chamber with studs on a 1.3-foot spacing. Additional limited rebar will be used around the weld necks, which will be isolated from the shotcrete by a barrier. This concept greatly reduced the amount of engineering and installation time for the shielding.
- The prototype stainless steel beam dump was removed from the Nova chamber at the end of July, and another fused silica optic was placed in the chamber after the prototype was removed to use as a baseline in the optic damage tests. The stainless steel beam dump showed no signs of catastrophic damage, and there was no evidence of excessive amounts of elements of stainless steel in the chamber.
- The target chamber vacuum 100% Title II Design Review was held in September. The first revision of the equipment specifications for the target chamber cryogenic high-vacuum pumps, gate valves, tritium gas-roughing pump, and turbodrag high-vacuum pumps was completed.
- The target positioner 100 % Title II Design Review was held in September.
- A web page has been developed to share diagnostic design information with representatives from LLNL, SNL, LLE, Los Alamos National Laboratory, and Atomic Weapons Research Establishment (AWE), U.K. The web page is internally accessible to LLNL experimenters and will soon be password accessible to NIF diagnostic users at other DOE sites. Discussions are taking place with a working group of people from other test facilities and labs to establish standards for diagnostics and their associated control and support equipment so that diagnostic can be used at multiple test facilities.

  Software Requirements Specifications (SRS) and Software Design Descriptions (SDD) documents for Embedded Controller Software and FEP Software have been started. These will form the foundation of the Target Diagnostics FEP and controller SRS and SDD documents.

- The Diagnostic Instrument Manipulator (DIM) drive system is now being manufactured. The trolley is finished and has been fitted onto the bench. The electronic rack has been finished and is awaiting checkout. The DIM extension tube was being fabricated in the United States. The extension tube will be completed by the end of September and shipped to AWE early in October.
- In September, the 100% Title II Design Review was conducted for the engineering of the major mirror frame structural components. This included the target chamber pedestal, the mirror frame supports and enclosures, the seismic restraints, and the FOAs.
- The peer review team met with the NIF team in August and reviewed the revised calculations for the seismic loads applied to the top of the pedestal and the target chamber to floor. They agreed with calculations presented and supported the use of a steel encasement around the upper ring beam to increase the load-bearing capacity and increase the safety factor. The steel encasement was fabricated and delivered and is awaiting incorporation into the pedestal.

FIGURE 5. IOM 2-dof fixture with IOM in fully retracted position. (40-00-0199-0195pb01)

- The Tritium Environmental Protection Systems work has been delayed until 2004 to be able to prepare for the introduction of tritium into the facility in 2005. The exception to this delay is the stack monitoring system, which will be in place for first bundle.
- The prototype 2 degree-of-freedom Integrated Optics Module (IOM) handling fixture (see Figure 5) was successfully tested on the FOA test stand in Building 432. The fixture was tested at angular orientations of 130°, 135.5°, 150°, and 156.5°, which represent the positions of IOM units on the lower half of the target chamber. These initial tests have validated the basic concept. All drive mechanisms, alignment features, and installation procedures worked as planned. Deflection of the IOM translation arm was within tolerance with no interference with adjacent IOM units. All tests were conducted with a 125% test load of 1050 pounds.
- The FOA 100% Title II Review presentation was delayed by approximately one month until November to allow more time for scientific review of the last Beamlet tests using the final optics cell (FOC). The Project Scientist has been leading the scientific review of the data and establishing priorities for future work. The last series of shots (high-damage-threshold campaign) tested frequency conversion crystals, focus lens, and diffractive optics plates in a configuration similar to the NIF optical design. (There are some differences between the optomechanical configuration in Beamlet and the baseline NIF configuration.) Optical damage was expected and was observed; however, it is taking some time to reduce the data, understand the mechanisms, and determine the contributing factors.
- The frequency conversion technical management plan has succeeded in establishing a firm understanding of frequency conversion performance for the NIF final optics design (i.e., significant factors, status of technology, error budget). Requirements from a detailed error budget have been flowed down to metrology equipment, crystal fabrication, coating performance, and mount tolerances. There is very good correlation between analysis predictions and experiment.
- The ghost analysis of the IOM was completed during the quarter. The baseline absorbing material is a PTFE (Teflon) product with a trade name of Spectralon. This material selection is based on adequate damage threshold, fabrication/installation ease, and cost. Extensive ghost mitigation measures have been incorporated into the FOC final design. Additional measures can be implemented if

future tests and First-Bundle operation indicate that they are needed.

- Integrated testing of the fully assembled FOA prototype hardware began in the high bay of Building 432. The vacuum/venting sequence evaluations will confirm (or suggest modifications to) the final design details of the debris shield module, pumping rates, and so on.
- A modification to the FOA debris shield cassette frame is shown under test in Figures 6 and 7. (The tests are conducted in a clean, enclosed hood with particle measurement wafers beneath the hardware.) Particulate generation has almost been completely eliminated with this design, which uses a solid stainless steel guide bar.

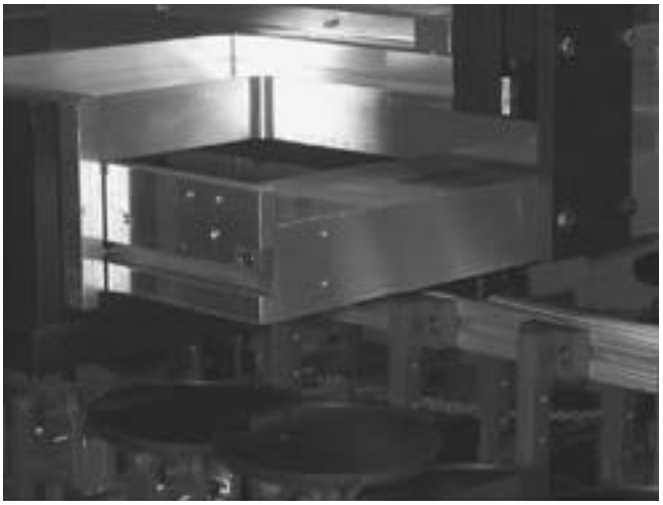

FIGURE 6. Debris shield cassette frame. (40-00-0199-0196pb01)

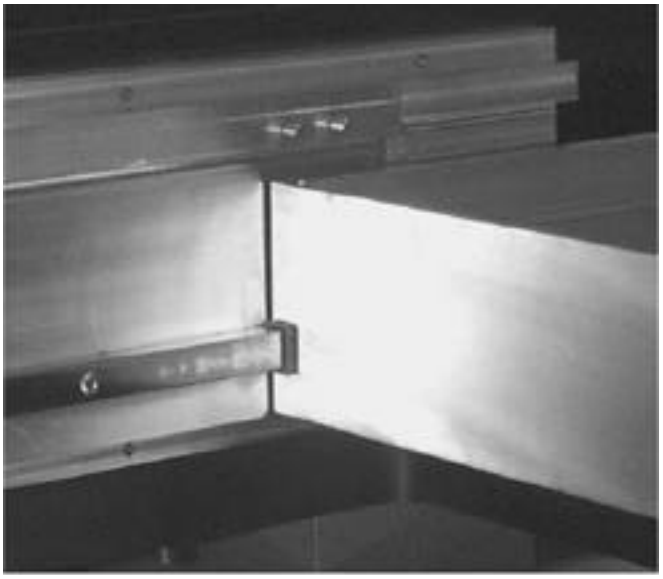

FIGURE 7. Cassette frame guide bar. (40-00-0199-0197pb01)

Operations Special Equipment

This has been a successful quarter with good progress in detailed design and prototype testing. Several DOE milestones were completed, including large procurements and design reviews. Preparations are currently under way for hardware installation in the OAB scheduled for October 1998.

- A number of significant changes for the OAB were agreed to in August during an LRU storage review. The IOM assembly area, Cave, and shutter assembly have been moved to Building 391. Space available in the OAB resulting from the location changes will be used for storage of LRUs. A complete 3D model of the animation sequence is being developed for formal review. This 3D integrated model will show extensive stay-out zones and will hopefully prevent major interference and space conflicts for the OAB, the corridor, and the LTAB aisles.
- The Transport and Material Handling 65% Design Review was successfully completed in August. Also an installation schedule is being developed for the T&H systems going into the Laser Bay Facility.
- The 65% review for T&H FEP controls was completed. The SRS for Bottom Loading, Top Loading, and Side Loading are nearly complete, which includes the requirements specification for the electronics, sensors and actuators, I/O boards, and software.
- The contract was awarded in August to AGV Products, Inc. for the fabrication of the hardware and software of the Laser Bay Transport System. Fabrication has begun, parts have been ordered, and the contract for the large fabrications has been awarded.
- Detailed design, prototyping, and procurement are in process for the Optical Assembly and Alignment Design. All drawings and procurements for equipment that will be installed in the OAB during October/November are complete. A new installation plan was also completed for equipment to be installed between October and November.

Start-Up Activities

- Level 0-3 Integrated Project Schedule (IPS) milestones are on track. The Target Area construction, CSP-6/10, is currently ahead of schedule. With the inclusion of the subcontractor baseline schedule for Conventional Facilities CSP-6/10, the IPS now contains all facility construction

baseline schedules. An Engineering Change Request has been submitted that modifies the Project milestone dictionary to be consistent with CSP-9 dates and definitions, excluding the core area of the Laser Bay for which workarounds are still under evaluation. First-bundle installation details in Laser Bay 2, which have been in planning off-line for several months, have now been added to the IPS database.

- A significant effort was devoted to preparing for the detailed review of the NIF First Bundle Start-Up Plan in July. The review was held for a committee that included reviewers from the NIF Project, the ICF-NIF Program, SNL-Albuquerque, UR-LLE, and LANL. The major goals of the review were to inform the Project staff on the detailed plans for First-Bundle Start-Up and to collect detailed feedback on the operational test procedures and their interfaces. Both goals were successfully achieved. A draft revision of the First Bundle Start-Up Test Plan was completed and is presently being proofed and edited. This draft revision included a review of all sections except the "Beam Transport to Target-Chamber Center and Final Optics Assembly Tests" and the "Beam Smoothing Tests." Further revision of the "Amplifier-Gain Test" section is being considered to add a subsection to discuss an on-line amplifier cleanliness test. Once the revision is completed, the Start-Up Plan will serve as the basis for the FY99 planning activities, including the writing of detailed operational test procedures. It will provide the interfaces to the Master Test Plan and contain sufficient information to create a resource plan and detailed schedule for execution of the first bundle start-up testing.
- The computer controls software acceptance test team's largest effort was developing system test procedures for the ICCS Nightlight release due in October. Five formal test procedures were drafted for OPG, PEPC, Laser Diagnostics, Automatic Alignment, and Power Conditioning/Shot Director. The technical staffs from NIF hardware and software development reviewed four of these test procedures. The fifth procedure, Laser Diagnostics process, has progressed more slowly due to key development staff focusing on non-laser diagnostic tasks. The procedure is expected to be completed in early October.
- The NIF Laser Operations Model is a code that will be used by Beam Controls and Diagnostics to set up the correct operating and diagnostic parameters to achieve power balance based on performance parameters of the individual beamlines and their components. This model will also provide critical information to support start-up planning and execution.
- Performance-based training (PBT) infrastructure development continues, and 16 functional areas have been identified for the development of training materials. Operations procedures are identified as part of this process. A detailed schedule has been developed using Project milestones so that training materials will be available when needed. Thus far, the first two (of three) phases of the PBT process are complete for the Optics Processing area, and the first phase is complete for the OAB area.
- A draft sequence for conducting facility readiness reviews is being prepared for review by the Project Manager. Planning for readiness reviews is being coordinated with the ICF/NIF Program, which is responsible for ICF facilities that are not part of the LTAB or OAB, but which will support NIF equipment testing, assembly, or development. Start-up has hired an ES&H specialist from the AVLIS program to provide part-time help planning readiness reviews.

Optics Technology

- Facilitization was in final stages at most vendors at the end of the fourth quarter as they started or prepared to start pilot in early FY99. All laser glass contracts are either in place or will be placed when the new fiscal year begins. Nd was in hand at both Schott and Hoya for their pilots. KDP rapid-growth facilitization at CCI and Inrad has gone well, and they have made excellent progress growing their first crystals, up to 27 cm in size. Corning was nearing completion of facilitization. The accelerated fused silica pilot was awarded early in September and has begun.
- Tinsley continued to make excellent progress on their finishing facility. They demonstrated outstanding performance with the first four NIF SF1 and SF2 lenses, which will be the first non-prototype optics they have made, and that will be used on the NIF First Bundle. Zygo was making good progress with their facility including resolution of the pitch problem discussed in previous reports. Initial hiring for pilot production has begun. LLE and Spectra-Physics continued to make good progress preparing for their pilots.
- Metrology issues with the interferometers have been resolved, and the final units have been ordered from Wyko.
- Postprocessing equipment has been arriving weekly to support the laser glass pilot run that starts in October. The laser glass pilot contracts were in place for the October start-up. Schott plans to ship the first laser glass slab to Zygo by

January or February 1999. The cladding glass pilot/production run is scheduled for January 1999.

- At Hoya, the full-scale furnace frame has been constructed and the bricking has begun. Several melter components, the lehr, and several fine-annealing ovens have been shipped from Japan. Hoya's batch mixing room is nearly complete. Laser glass and cladding glass pilot contracts are in place. Hoya starts their pilot in October with 200 slab equivalents of cladding glass being produced in Japan, which will support first-bundle needs. Their laser glass pilot run is scheduled for January 1999 with the first laser glass slab shipped to Zygo for finishing by April 1999.
- A deuterated potassium dihydrogen (DKDP) boule grown at LLNL reached NIF size at the end of September. The boule is large enough to yield 17 NIF tripler crystals, demonstrating substantial improvement in our ability to control inclusion formation. Optical quality was very good, but 3ω laser damage threshold has yet to be measured. A 15-cm KDP crystal rapidly grown with constant filtration achieved the highest 3ω laser damage threshold of the year and would be expected to have negligible damage at maximum NIF fluences. Both CCI and Inrad grew KDP boules >25 cm in their shakedown runs using NIF production equipment.
- The Moore Tool Company continued to assemble the diamond turning machine at LLNL. Their efforts did not proceed as rapidly as estimated, and it appears that they will need the month of October to make the machine ready for acceptance tests beginning in November. Several items associated with the fly cutter and drive spindles, X and Z slides, and the temperature control must be addressed before the acceptance tests can begin.
- Corning has completed installation of the new overarm lapping machine and begun installation of the polisher. Their new Zygo 24" interferometer is in-house and will be operational by mid-October. The fused silica pilot was awarded to Corning in early September.
- Tinsley's lens and window finishing facility building construction has continued on schedule. Beneficial occupancy and installation of manufacturing equipment is planned for November and December. All manufacturing equipment for the facility has been accounted for and is nearing completion. Most equipment has been run and tested in Tinsley's existing facility and has been used during an early pilot production to produce NIF specification lenses. An award was made to Kodak to construct the NIF Flexible Finishing Facility, which will be designed to augment flats finishing capacity for NIF amplifiers, mirrors, and fused silica windows and to provide a backup for the critical 3ω focus lens.
- Zygo's automated cleaning equipment passed its acceptance tests. LLNL's software for power spectral density (PSD) was installed and run successfully on the first 24" Zygo interferometer. Cavity measurements demonstrated the instrument has an acceptably low noise floor level. The first NIF demonstration amplifier slab has been processed through both phases of edge-cladding bonding, edge machining, and automated beveling.
- Facilitization work at LLE focused on design efforts to reduce the deposition time by the removal of "hot" substrates, planetary design in the 54" chamber for complete devotion of the 72". coater to NIF work, and mount designs for the laser conditioning stations. All of the facility modifications were completed at Spectra-Physics including the cleaning, coating, and metrology areas. The large NIF chamber was returned to operating condition and resumed process optimization activities.
- A NIF-size color separation grating (CSG) was successfully fabricated with the prototype long hydrofluoric etch station. This full-sized optic achieved a 3ω transmission of 89.4% with a sigma of 0.3%, which is significantly lower variability than CSGs previously etched by hand.
- The facility modifications for the Building 391W phase I Optics Processing Research and Development Area were completed. Balancing of the air-handling systems and certification of the clean room is under way. Beneficial occupancy is targeted for mid-November.

PUBLICATIONS AND PRESENTATIONS JULY–SEPTEMBER 1998

A

Allshouse, G. O., Olson, R. E., Callahan-Miller, D., and Tabak, M., *Deposition and Drive Symmetry for Light Ion ICF Targets*, Lawrence Livermore National Laboratory, Livermore, CA, UCRL-JC-131395. Submitted to *Nucl. Fusion*.

Amendt, P. A., Turner, R. E., Landen, O., Glendinning, S. G., Kalantar, D., Cable, M., Colvin, J., Decker, C., Suter, L. J., and Wallace, R., *High-Convergence Indirect-Drive Implosions on OMEGA: Design and Simulations*, Lawrence Livermore National Laboratory, Livermore, CA, UCRL-JC-130677 ABS Rev. Prepared for *40th Annual Mtg of the Div of Plasma Physics*, New Orleans, LA, Nov 16, 1998.

Arnett, D., Drake, R. P., Remington, B. A., and Takabe, H., *Emergence of Laboratory Astrophysics with Intense Lasers*, Lawrence Livermore National Laboratory, Livermore, CA, UCRL-JC-131535. Submitted to *Science Magazine*.

Auerbach, J. M., Barker, C. E., Couture, S. A., Eimerl, D., De Yoreo, J. J., Hackel, L. A., Hibbard, R. L., Liou, L. W., Norton, M. A., and Perfect, S. A., *Modeling of Frequency Doubling and Tripling with Converter Refractive Index Spatial Non-Uniformities due to Gravitational Sag*, Lawrence Livermore National Laboratory, Livermore, CA, UCRL-JC-130030. Prepared for *3rd Annual Intl Conf on Solid State Lasers for Application (SSLA) to Inertial Confinement Fusion (ICF)*, Monterey, CA, Jun 7, 1998.

B

Back, C. A., Bauer, J. D., Turner, R. E., Lasinski, B. F., Suter, L. J., Landen, O. L., Hsing, W. W., and Soures, J. M., *Temporally- and Radially-Resolved Breakout of a Heat Wave in Radiatively Heated Foam Targets*, Lawrence Livermore National Laboratory, Livermore, CA, UCRL-JC-131363 ABS. Prepared for *40th Annual Mtg of the Div of Plasma Physics*, New Orleans, LA, Nov 16, 1998.

Back, C. A., Woolsey, N. C., Missalla, T., Landen, O. L., Dalhed, S., Libby, S. B., and Lee, R. W., *Accessible Dense Matter Physics Using Hohlraum-Driven Implosions*, Lawrence Livermore National Laboratory, Livermore, CA, UCRL-JC-131394 ABS. Prepared for *40th Annual Mtg of the Div of Plasma Physics*, New Orleans, LA, Nov 16, 1998.

Back, C. A., Woolsey, N. C., Missalla, T., Landen, O. L., Libby, S. B., Klein, L. S., and Lee, R. W., *Implosions: an Experimental Testbed for High Energy Density Physics*, Lawrence Livermore National Laboratory, Livermore, CA, UCRL-JC-129715. Prepared for *2nd Intl Workshop on Laboratory Astrophysics with Intense Lasers*, Tucson, AZ, Mar 19, 1998.

Battersby, C. L., Sheehan, L. M., and Kozlowski, M. R., *Effects of Wet Etch Processing on Laser-Induced Damage of Fused Silica Surfaces*, Lawrence Livermore National Laboratory, Livermore, CA, UCRL-JC-131224 ABS. Prepared for *30th Boulder Damage Symp: Annual Symp on Optical Materials for High Power Lasers*, Boulder, CO, Sept 28, 1998.

Berger, R. L., Cohen, B. I., Langdon, A. B., MacGowan, B. J., Rothenberg, J., Still, C. W., Williams, E. A., and Lefebvre, E., *Polarization and Spectral Dispersion Smoothing: Effects on SBS, SRS, and Filamentation*, Lawrence Livermore National Laboratory, Livermore, CA, UCRL-JC-130578 ABS Rev. Prepared for *40th Annual Mtg of the Div of Plasma Physics*, New Orleans, LA, Nov 16, 1998.

Bittner, D. N., Collins, G. W., Burmann, J., and Unites, W., *Forming Uniform HD Layers in Shells Using Infrared Radiation*, Lawrence Livermore National Laboratory, Livermore, CA, UCRL-JC-131371 ABS. Prepared for *40th Annual Mtg of the Div of Plasma Physics*, New Orleans, LA, Nov 16, 1998.

Boley, C. D., and Rhodes, M. A., *Modeling of Plasma Behavior in a Plasma Electrode Pockels Cell*, Lawrence Livermore National Laboratory, Livermore, CA, UCRL-JC-131445. Submitted to *Transactions on Plasma Science*.

Boley, C. D., Estabrook, K. G., Auerbach, J. M., Feit, M. D., and Rubenchik, A. M., *Modeling of Laser Knife-Edge and Pinhole Experiments*, Lawrence Livermore National Laboratory, Livermore, CA, UCRL-JC-129613. Prepared for *3rd Annual Intl Conf on Solid State Lasers for Application (SSLA) to Inertial Confinement Fusion (ICF)*, Monterey, CA, Jun 7, 1998.

Britten, J. A., Dixit, S. N., Summers, L. J., Herman, S. M., Auyang, L., Rushford, M. C., and Parham, T. G., *Manufacture, Optical Performance and Laser Damage Characteristics of Diffractive Optics for the National Ignition Facility Laser*, Lawrence Livermore National Laboratory, Livermore, CA, UCRL-JC-131517 ABS. Prepared for *30th Boulder Damage Symp: Annual Symp on Optical Materials for High Power Lasers*, Boulder, CO, Sept 28, 1998.

Budil, K. S., *From Nova to NIF: the Quest for Fusion in the Laboratory*, Lawrence Livermore National Laboratory, Livermore, CA, UCRL-JC-131872 ABS. Prepared for *Talk at the Naval Postgraduate School*, Monterey, CA, Oct. 2, 1998.

Budil, K. S., *From Nova to Supernova: Bringing the stars down to earth*, Lawrence Livermore National Laboratory, Livermore, CA, UCRL-JC-131873 ABS. Prepared for *Talk at Washington State University*, Pullman, WA, Sept 29, 1998.

Budil, K. S., Gold, D. M., Estabrook, K. G., Remington, B. A., Kane, J., Bell, P. M., Pennington, D. M., Brown, C., Hatchett, S. P., and Koch, J. A., *Development of a Radiative-Hydrodynamics Testbed Using the Petawatt Laser Facility*, Lawrence Livermore National Laboratory, Livermore, CA, UCRL-JC-131549. Prepared for *2nd Intl Workshop on Laboratory Astrophysics with Intense Lasers*, Tucson, AZ, Mar 19, 1998.

Budil, K. S., Wan, A. S., Lasinski, B., Remington, B. A., Suter, L., and Stry, P. E., *Ablation Front Rayleigh–Taylor Instability in High-Z Materials*, Lawrence Livermore National Laboratory, Livermore, CA, UCRL-JC-131351 ABS. Prepared for *40th Annual Mtg of the Div of Plasma Physics*, New Orleans, LA, Nov 16, 1998.

C

Callahan-Miller, D. A., and Tabak, M., *Close-Coupled, Heavy Ion ICF Target*, Lawrence Livermore National Laboratory, Livermore, CA, UCRL-JC-131243 ABS. Prepared for *40th Annual Mtg of the Div of Plasma Physics*, New Orleans, LA, Nov 16, 1998.

Callahan-Miller, D. A., and Tabak, M., *Distributed Radiator Heavy Ion Target with Realistic, Multibeam Illumination Geometry*, Lawrence Livermore National Laboratory, Livermore, CA, UCRL-JC-131543. Submitted to *Nucl. Fusion*.

Callahan-Miller, D. A., *Heavy-Ion Driven, Inertial Confinement Fusion*, Lawrence Livermore National Laboratory, Livermore, CA, UCRL-JC-131962 ABS. Prepared for *Women's Technical and Professional Symp*, San Ramon, CA, Oct 15, 1998.

Campbell, J. H., McLean, M. J., Hawley-Fedder, R., Suratwala, T., Ficini-Dorn, G., and Trombert, J. H., *Development of Continuous Glass Melting for Production of Nd-Doped Phosphate Glasses for the NIF and LMJ Laser Systems*, Lawrence Livermore National Laboratory, Livermore, CA, UCRL-JC-129804. Prepared for *3rd Annual Intl Conf on Solid State Lasers for Application (SSLA) to Inertial Confinement Fusion (ICF)*, Monterey, CA, Jun 7, 1998.

Celliers, P. M., Collins, G. W., Da Silva, L. B., Gold, D. M., and Cauble, R., *Accurate Measurement of Laser-Driven Shock Trajectories with Velocity Interferometry*, Lawrence Livermore National Laboratory, Livermore, CA, UCRL-JC-130597; *Appl. Phys. Lett.* **73**(10), 1320–1322 (1998).

Celliers, P. M., Collins, G. W., Gold, D. M., Cauble, R. C., Da Silva, L. B., Wallace, R. J., and Foord, M. E., *Shock Transformation of Deuterium from Molecular Fluid to Liquid Metal*, Lawrence Livermore National Laboratory, Livermore, CA, UCRL-JC-131511 ABS. Prepared for *40th Annual Mtg of the Div of Plasma Physics*, New Orleans, LA, Nov 16, 1998.

Chang, J. J., McLean, W., Dragon, E. P., and Warner, B. E., *Emission Spectra and Particle Ejection during Laser Ablation of Graphite for Diamond-Like Coatings*, Lawrence Livermore National Laboratory, Livermore, CA, UCRL-JC-131300 ABS. Prepared for *Photonics West '99 Symp*, San Jose, CA, Jan 23, 1999.

Cohen, B. I., Lasinski, B. F., Langdon, A. B., Williams, E. A., Baldis, H. A., and Labaune, C., *Suppression of Stimulated Brillouin Scattering by Seeded Ion Wave Mode Coupling*, Lawrence Livermore National Laboratory, Livermore, CA, UCRL-JC-129490; *Phys. Plasmas* **5**(9), 3402–3407 (1998).

Cohen, B. I., Lasinski, B. F., Langdon, A. B., Williams, E. A., Wharton, K. B., Kirkwood, R. K., and Estabrook, K. G., *Resonant Stimulated Brillouin Interaction of Opposed Laser Beams in a Drifting Plasma*, Lawrence Livermore National Laboratory, Livermore, CA, UCRL-JC-129491; *Phys. Plasmas* **5**(9), 3408–3415 (1998).

Collins, G. W., Celliers, P. M., Da Silva, L. B., Cauble, R., Gold, D. M., Foord, M. E., Holmes, N. C., Hammel, B. A., Wallace, R. J., and Ng, A., *Temperature Measurements of Shock Compressed Liquid Deuterium up to 230 GPa*, Lawrence Livermore National Laboratory, Livermore, CA, UCRL-JC-131955. Submitted to *Phys. Rev. Lett.*

Collins, G. W., Celliers, P., Gold, D. M., Da Silva, L. B., Cauble, R., Hammel, B. A., and Wallace, R. J., *Shock Compressing Diamond into the Metallic Phase*, Lawrence Livermore National Laboratory, Livermore, CA, UCRL-JC-131400 ABS. Prepared for *40th Annual Mtg of the Div of Plasma Physics*, New Orleans, LA, Nov 16, 1998.

Collins, G. W., Da Silva, L. B., Celliers, P., Gold, D. M., Foord, M. E., Wallace, R. J., Ng, A., Weber, S. V., Budil, K. S., and Cauble, R., "Measurements of the Equation of State of Deuterium at the Fluid Insulator-Metal Transition," *Science* **281**, 1178–1181 (1998).

Colston Jr., B. W., Sathyam, U. S., Da Silva, L. B., Everett, M. J., Stroeve, P., and Otis, L. L., *Dental OCT*, Lawrence Livermore National Laboratory, Livermore, CA, UCRL-JC-131547; *Optics Express* **3**(6), 230–238 (1998).

Colvin, J. D., *Hydrodynamic Stability Analysis of Laser-Driven Double-Shell Capsule Implosions*, Lawrence Livermore National Laboratory, Livermore, CA, UCRL-JC-131375 ABS. Prepared for *40th Annual Mtg of the Div of Plasma Physics*, New Orleans, LA, Nov 16, 1998.

Colvin, J. D., Weber, S., Kalantar, D., and Remington, B., *Drive Modeling and Characterization for Solid-State Instability Experiments on the Nova Laser*, Lawrence Livermore National Laboratory, Livermore, CA, UCRL-JC-131398 ABS. Prepared for *40th Annual Mtg of the Div of Plasma Physics*, New Orleans, LA, Nov 16, 1998.

Correll, D., and Spafford, T., *Lasers*, Lawrence Livermore National Laboratory, Livermore, CA, UCRL-JC-131523. Submitted to *Grolier's New Book of Knowledge*.

Correll, D., *Inertial Confinement Fusion Annual Report 1997*, Lawrence Livermore National Laboratory, Livermore, CA, UCRL-LR-105821-97.

Crane, J. K., Wilcox, R. B., Hopps, N. W., Browning, D., Martinez, M. D., Moran, B., Penko, F., Rothenberg, J. E., Henesian, M., and Dane, C. B., *Integrated Operations of the National Ignition Facility (NIF) Optical Pulse Generation Development System*, Lawrence Livermore National Laboratory, Livermore, CA, UCRL-JC-129871. Prepared for *3rd Annual Intl Conf on Solid State Lasers for Application (SSLA) to Inertial Confinement Fusion (ICF)*, Monterey, CA, Jun 7, 1998.

Crane, J. K., Wilcox, R. B., Hopps, N., Moran, B., Martinez, M., Browning, D., Dane, B., Rothenberg, J. E., Henesian, M., and Penko, F., *Optical Pulse Generation System for the National Ignition Facility*, Lawrence Livermore National Laboratory, Livermore, CA, UCRL-JC-130953. Prepared for *1998 American Nuclear Society Annual Mtg*, Nashville, TN, Jun 7, 1998.

D

Dane, C. B., Hackel, L. A., Daly, J., and Harrison, J., *High Power Laser for Peening of Metals Enabling Production Technology*, Lawrence Livermore National Laboratory, Livermore, CA, UCRL-JC-131104 Rev 1. Prepared for *Advanced Aerospace Materials & Processes Conf '98*, Tysons Corner, VA, Jun 15, 1998.

De Groot, J. S., Deeney, C., Hammer, J. H., Reisman, D. B., Ryutov, D., Sanford, T. W. L., Spielman, B., and Toor, A., *Initiation of Rayleigh–Taylor Instability in Wire Array Plasmas*, Lawrence Livermore National Laboratory, Livermore, CA, UCRL-JC-131392 ABS. Prepared for *40th Annual Mtg of the Div of Plasma Physics*, New Orleans, LA, Nov 16, 1998.

Decker, C., Suter, L., Back, C., Serduke, F., Grun, J., Laming, M., and Davis, J., *Designs for Highly Efficient K-Shell Radiators*, Lawrence Livermore National Laboratory, Livermore, CA, UCRL-JC-131391 ABS. Prepared for *40th Annual Mtg of the Div of Plasma Physics*, New Orleans, LA, Nov 16, 1998.

Dimonte, G., *Atwood (A) Number Variation of Turbulent Rayleigh–Taylor Mixing*, Lawrence Livermore National Laboratory, Livermore, CA, UCRL-JC-131520 ABS. Prepared for *51st Annual Mtg of the Div of Fluid Dynamics*, Philadelphia, PA, Nov 22, 1998.

Dimonte, G., *Atwood (A) Number Variation of Turbulent Rayleigh–Taylor Mixing: Experiments and Model*, Lawrence Livermore National Laboratory, Livermore, CA, UCRL-JC-131860 ABS. Prepared for *Turbulence and Shear Flow Phenomena First Intl Symp*, Santa Barbara, CA, Sept 12, 1999.

Dimonte, G., *Rayleigh–Taylor and Richtmyer–Meshkov Instabilities in Turbulent Regime*, Lawrence Livermore National Laboratory, Livermore, CA, UCRL-JC-131250 ABS. Prepared for *40th Annual Mtg of the Div of Plasma Physics*, New Orleans, LA, Nov 16, 1998.

Dittrich, T. R., Haan, S. W., Marinak, M. M., Hinkel, D. E., Pollaine, S. M., McEachern, R. L., Cook, R. C., Roberts, C. C., Wilson, D. C., and Bradley, P. A., *Capsule Design for the National Ignition Facility*, Lawrence Livermore National Laboratory, Livermore, CA, UCRL-JC-130102. Prepared for *25th European Conf on Laser Interaction with Matter*, Formia, Italy, May 4, 1998.

Dittrich, T. R., Haan, S. W., Marinak, M. M., Pollaine, S. M., Hinkel, D. E., Strobel, G. L., MacEachern, R., Cook, R. C., Roberts, C. C., and Wilson, D. C., *Review of Indirect-Drive Ignition Design Options for the National Ignition Facility*, Lawrence Livermore National Laboratory, Livermore, CA, UCRL-JC-131383 ABS. Prepared for *40th Annual Mtg of the Div of Plasma Physics*, New Orleans, LA, Nov 16, 1998.

Drake, R. P., Glendinning, S. G., Estabrook, K., Remington, B. A., McCray, R., Wallace, R. J., Suter, L. J., Smith, T. B., Carroll III, J. J., London, R. A., and Liang, E., "Observation of Forward Shocks and Stagnated Ejecta Driven by High-Energy-Density Plasma Flow," *Phys. Rev. Lett.* **81**(10), 2068–2071 (1998).

Dubois, P. F., *Facility for Creating Python Extensions in C++*, Lawrence Livermore National Laboratory, Livermore, CA, UCRL-JC-131396. Prepared for *7th Intl Python Conf*, Houston, TX, Nov 9, 1998.

E

Edwards, M. J., Glendinning, S. G., Suter, L. J., Shepard, T. J., Turner, R. E., Graham, P., Dunne, A. M., and Thomas, B. R., *Development of Laser Produced Sources for Hydrodynamic Experiments Driven by Combined Material Pressure and X-Ray Ablation*, Lawrence Livermore National Laboratory, Livermore, CA, UCRL-JC-131361 ABS. Prepared for *40th Annual Mtg of the Div of Plasma Physics*, New Orleans, LA, Nov 16, 1998.

Emanuel, M. A., Skidmore, J. A., and Freitas, B. L., *Final Report for High Beam Quality Laser Diodes (LDRD 96-ERD-003)*, Lawrence Livermore National Laboratory, Livermore, CA, UCRL-ID-126453.

Estabrook, K. G., Glenzer, S. H., Back, C. A., Rozmus, W., Wilson, B. G., De Groot, J. S., Zimmerman, G. B., Langer, S. H., Lee, R. W., and Hart, J. A., *Thomson Scattering Measurements Compared with LASNEX Simulations*, Lawrence Livermore National Laboratory, Livermore, CA, UCRL-JC-131379 ABS. Prepared for *40th Annual Mtg of the Div of Plasma Physics*, New Orleans, LA, Nov 16, 1998.

Estabrook, K., Remington, B. A., Farley, D., Glendinning, G., Suter, L. J., Harte, J. H., Zimmerman, G. B., Stone, J., Wood-Vasey, M., and Drake, R. P., *Simulations of Radiative Astrophysical Jets*, Lawrence Livermore National Laboratory, Livermore, CA, UCRL-JC-131427 ABS. Prepared for *40th Annual Mtg of the Div of Plasma Physics*, New Orleans, LA, Nov 16, 1998.

F

Feit, M. D., *ICF Quarterly Report* **8** (1), Lawrence Livermore National Laboratory, Livermore, CA, UCRL-LR-105821-98-1 (1998).

Feit, M. D., Rubenchik, A. M., Kozlowski, M. K., Genin, F. Y., Schwartz, S., and Sheehan, L. M., *Extrapolation of Damage Test Data to Predict Performance of Large-Area NIF Optics at 355 nm*, Lawrence Livermore National Laboratory, Livermore, CA, UCRL-JC-131222 ABS. Prepared for *30th Boulder Damage Symp: Annual Symp on Optical Materials for High Power Lasers*, Boulder, CO, Sept 28, 1998.

Feit, M. D., Wu, Z. L., Rubenchik, A. M., Sheehan, L. M., and Kozlowski, M. R., *Optical Absorption of Laser Damaged Fused Silica*, Lawrence Livermore National Laboratory, Livermore, CA, UCRL-JC-131223 ABS. Prepared for *30th Boulder Damage Symp: Annual Symp on Optical Materials for High Power Lasers*, Boulder, CO, Sept 28, 1998.

Fernandez, J. C., Bauer, B. S., Bradley, K. S., Cobble, J. A., Montgomery, D. S., Watt, R. G., Bezzerides, B., Estabrook, K. G., Focia, R., Goldman, S. R., Harris, D. B., Lindman, E. L., Rose, H. A., Wallace, J., and Wilde, B. H., "Increased Saturated Levels of Stimulated Brillouin Scattering of a Laser by Seeding a Plasma with an External Light Source," *Phys. Rev. Lett.* **81**(11), 2252–2255 (1998).

G

Geddes, C. G. R., Kirkwood, R. K., Glenzer, S. H., Estabrook, K. G., Joshi, C., and Wharton, K. B., *Study of the Saturation of Stimulated Raman Scattering by Secondary Decays*, Lawrence Livermore National Laboratory, Livermore, CA, UCRL-JC-130328 ABS Rev. Prepared for *40th Annual Mtg of the Div of Plasma Physics*, New Orleans, LA, Nov 16, 1998.

Geddes, C. G., Sanchez, J. J., Collins, G. W., and McKenty, P., *Interferometric Characterization of Hydrogen Ice Layers in NIF Scale Targets*, Lawrence Livermore National Laboratory, Livermore, CA, UCRL-JC-131367 ABS. Prepared for *40th Annual Mtg of the Div of Plasma Physics*, New Orleans, LA, Nov 16, 1998.

Glendinning, S. G., Amendt, P., Cline, B. D., Ehrlich, R. B., Hammel, B. A., Kalantar, D. H., Landen, O. L., Wallace, R. J., Weiland, T. J., and Dague, N., *Hohlraum Symmetry Measurements with Surrogate Solid Targets*, Lawrence Livermore National Laboratory, Livermore, CA, UCRL-JC-129773-DR. Prepared for *12th Topical Conf on High-Temperature Plasma Diagnostics*, Princeton, NJ, Jun 7, 1998.

Glendinning, S. G., Budil, K. S., Cherfils, C., Drake, R P., Farley, D., Kalantar, D. H., Kane, J., Marinak, M. M., Remington, B. A., and Richard, A., *Experimental Measurements of Hydrodynamic Instabilities on Nova of Relevance to Astrophysics*, Lawrence Livermore National Laboratory, Livermore, CA, UCRL-JC-130104. Prepared for *2nd Intl Workshop on Laboratory Astrophysics with Intense Lasers*, Tucson, AZ, Mar 19, 1998.

Glendinning, S. G., Collins, G. W., Marinak, M. M., Haan, S. W., Weber, S. V., Wallace, R. J., and Dague, N., *Rayleigh–Taylor Growth of Ablation Front Modulations in Indirectly-Driven Be/Cu Planar Foils*, Lawrence Livermore National Laboratory, Livermore, CA, UCRL-JC-127922 ABS Rev. Prepared for *40th Annual Mtg of the Div of Plasma Physics*, New Orleans, LA, Nov 16, 1998.

Glenzer, S. H., Rozmus, W., MacGowan, B. J., Estabrook, K. G., De Groot, J. D., Zimmerman, G. B., Baldis, H. A., Hammel, B. A., Harte, J. A., and Lee, R. W., *Thomson Scattering from High-Z Laser-Produced Plasmas*, Lawrence Livermore National Laboratory, Livermore, CA, UCRL-JC-131980. Submitted to *Phys. Rev. Lett.*

Glenzer, S. H., Rozmus, W., MacGowan, B. J., Estabrook, K. G., Harte, J. A., Lee, R. W., Williams, E. A., and Wilson, B. G., *Detailed Characterization of High-Z-Plasmas for Benchmarking of Radiation-Hydrodynamic Modeling*, Lawrence Livermore National Laboratory, Livermore, CA, UCRL-JC-131979 ABS. Prepared for *8th Intl Workshop on Radiative Properties of Hot Dense Matter*, Sarasota, FL, Oct 26, 1998.

Glenzer, S. H., Rozmus, W., MacGowan, B. J., Estabrook, K. G., Suter, L. J., Baldis, H. A., and Moody, J. D., *Thomson Scattering from Laser Plasmas*, Lawrence Livermore National Laboratory, Livermore, CA, UCRL-JC-131357 ABS. Prepared for *40th Annual Mtg of the Div of Plasma Physics*, New Orleans, LA, Nov 16, 1998.

Glenzer, S. H., *X-Ray Spectroscopy from Fusion Plasmas*, Lawrence Livermore National Laboratory, Livermore, CA, UCRL-JC-130122. Prepared for *14th Intl Conf on Spectral Line Shapes*, State College, PA, Jun 22, 1998.

H

Haan, S. W., Koch, J. A., Sangster, T. C., Pollaine, S. M., Dittrich, T. R., Marinak, M. M., and Cable, M. D., *Target Simulations for Diagnostic Design for Ignition Targets for the National Ignition Facility*, Lawrence Livermore National Laboratory, Livermore, CA, UCRL-JC-131431 ABS. Prepared for *40th Annual Mtg of the Div of Plasma Physics*, New Orleans, LA, Nov 16, 1998.

Hammer, J. H., Ryutov, D., Liberman, M., Reisman, D., De Groot, J. S., Tabak, M., and Toor, A., *Discrete Wire Effects on Wire Array Instability*, Lawrence Livermore National Laboratory, Livermore, CA, UCRL-JC-131386 ABS. Prepared for *40th Annual Mtg of the Div of Plasma Physics*, New Orleans, LA, Nov 16, 1998.

Hammer, J. H., Tabak, M., Wilks, S., Lindl, J., Toor, A., Zimmerman, G., Porter, J., McDaniel, D., and Spielman, R. B., *High Gain ICF Target Design for a Z-Pinch Driven Hohlraum*, Lawrence Livermore National Laboratory, Livermore, CA, UCRL-JC-131389 ABS. Prepared for *40th Annual Mtg of the Div of Plasma Physics*, New Orleans, LA, Nov 16, 1998.

Hatchett, S. P., Lasinski, B. F., Phillips, T. W., Wilks, S. C., and Perry, M. D., *Models of γ-Ray Sources for Radiography Driven by Ultra-Intense Lasers*, Lawrence Livermore National Laboratory, Livermore, CA, UCRL-JC-131244 ABS. Prepared for *40th Annual Mtg of the Div of Plasma Physics*, New Orleans, LA, Nov 16, 1998.

Hermann, M., and Fisch, N., *Recent Progress in Simulating α-Channelling*, Lawrence Livermore National Laboratory, Livermore, CA, UCRL-JC-131378 ABS. Prepared for *40th Annual Mtg of the Div of Plasma Physics*, New Orleans, LA, Nov 16, 1998.

Hinkel, D. E., and Haan, S. W., *National Ignition Facility 350 eV Target*, Lawrence Livermore National Laboratory, Livermore, CA, UCRL-JC-131384 ABS. Prepared for *40th Annual Mtg of the Div of Plasma Physics*, New Orleans, LA, Nov 16, 1998.

Ho, D. D., Chen, Y.-J., and Pincosy, P. A., *Methods for Containing the Plasma Plume Expansion from the Targets for X-Ray Radiography*, Lawrence Livermore National Laboratory, Livermore, CA, UCRL-JC-130970 ABS Rev. Prepared for *40th Annual Mtg of the Div of Plasma Physics*, New Orleans, LA, Nov 16, 1998.

Hopps, N. W., Wilcox, R. B., Hermann, M. R., Martinez, M. D., Padilla, E. H., and Crane, J. K., *Optimisation of the Alignment Sensitivity and Energy Stability of the NIF Regenerative Amplifier Cavity*, Lawrence Livermore National Laboratory, Livermore, CA, UCRL-JC-130961. Prepared for *3rd Annual Intl Conf on Solid State Lasers for Application (SSLA) to Inertial Confinement Fusion (ICF)*, Monterey, CA, Jun 7, 1998.

J

Jones, O. S., Pollaine, S. M., and Suter, L. J., *Effects of P6 and P8 Asymmetries on Indirect Drive Implosions*, Lawrence Livermore National Laboratory, Livermore, CA, UCRL-JC-131426 ABS. Prepared for *40th Annual Mtg of the Div of Plasma Physics*, New Orleans, LA, Nov 16, 1998.

K

Kalantar, D. H., Chandler, E., Colvin, J., Michaelian, K., Remington, B., Weber, S., Wiley, L., Wark, J. S., and Hauer, A. A., *Solid State Hydrodynamics Experiments on the Nova Laser*, Lawrence Livermore National Laboratory, Livermore, CA, UCRL-JC-131248 ABS. Prepared for *40th Annual Mtg of the Div of Plasma Physics*, New Orleans, LA, Nov 16, 1998.

Kalantar, D. H., Colvin, J., Remington, B. A., Weber, S., Wiley, L., Wark, J. S., Loveridge, A., Hauer, A. A., Failor, B. H., and Myers, M. A., *Transient X-Ray Diffraction from Shock Compressed Si Crystals on the Nova Laser*, Lawrence Livermore National Laboratory, Livermore, CA, UCRL-JC-131247 ABS. Prepared for *40th Annual Mtg of the Div of Plasma Physics*, New Orleans, LA, Nov 16, 1998.

Kalantar, D. H., Remington, B. A., Chandler, E. A., Colvin, J. D., Gold, D. M., Mikaelian, K. O., Weber, S. V., Wiley, L. G., Wark, J. S., and Loveridge, A., *Developing Solid State Experiments on the Nova Laser*, Lawrence Livermore National Laboratory, Livermore, CA, UCRL-JC-131851-DR. Prepared for *2nd Intl Workshop on Laboratory Astrophysics with Intense Lasers*, Tucson, AZ, Mar 19, 1998.

Kane, J., Arnett, D., Remington, B. A., Glendinning, S. G., Ryutov, D., Fryxell, B., and Drake, R. P., *Supernova-Relevant Experiments on the Nova Laser*, Lawrence Livermore National Laboratory, Livermore, CA, UCRL-JC-131362 ABS. Prepared for *40th Annual Mtg of the Div of Plasma Physics*, New Orleans, LA, Nov 16, 1998.

Kauffman, R. L., *High Intensity Laser–Matter Interaction Experiments at LLNL*, Lawrence Livermore National Laboratory, Livermore, CA, UCRL-JC-131981 ABS. Prepared for *Atomic Molecular and Optical Physics Mtg*, Ellicott City, MD, Oct 25, 1998.

Kauffman, R., *Monthly Highlights*, August 1998, Lawrence Livermore National Laboratory, Livermore, CA, UCRL-TB-128550-98-11.

Kauffman, R., *Monthly Highlights*, July 1998, Lawrence Livermore National Laboratory, Livermore, CA, UCRL-TB-128550-98-10.

Kauffman, R., *Monthly Highlights*, Jun 1998, Lawrence Livermore National Laboratory, Livermore, CA, UCRL-TB-128550-98-9.

Keilty, K., Liang, E., Ditmire, T. R., Remington, B. A., Rubenchik, A. M., Shigemori, K., and Moore, K., *Modeling of Blast Waves Generated on the Falcon Laser*, Lawrence Livermore National Laboratory, Livermore, CA, UCRL-JC-131246 ABS. Prepared for *40th Annual Mtg of the Div of Plasma Physics*, New Orleans, LA, Nov 16, 1998.

Kilkenny, J. D., Bernat, T. P., Hammel, B. A., Kauffman, R. L., Landen, O. L., Lindl, J. D., MacGowan, B. J., Paisner, J. A., and Powell, H. T., *Lawrence Livermore National Laboratory's Activities to Achieve Ignition by X-Ray Drive on the National Ignition Facility*, Lawrence Livermore National Laboratory, Livermore, CA, UCRL-JC-131510. Prepared for *25th European Conf on Laser Interaction with Matter*, Formia, Italy, May 4, 1998.

Kilkenny, J. D., Campbell, E. M., Lindl, J. D., Logan, G. B., Meier, W. R., Perkins, J. L., Paisner, J. A., Key, M. H., Powell, H. T., and McCrory, R. L., *Role of the National Ignition Facility in Energy Production from Inertial Fusion*, Lawrence Livermore National Laboratory, Livermore, CA, UCRL-JC-131355.

Kirkwood, R. K., Berger, R. L., Dixit, S. N., Rothenberg, J., Glenzer, S. H., MacGowan, B. J., Moody, J. D., and Geddes, C. G. R., *Scaling of Saturated SRS with Laser Intensity Correlation Length*, Lawrence Livermore National Laboratory, Livermore, CA, UCRL-JC-131397 ABS. Prepared for *40th Annual Mtg of the Div of Plasma Physics*, New Orleans, LA, Nov 16, 1998.

Koch, J. A., Haan, S. W., Hammel, B. A., Landen, O. L., McEachern, R. L., Phillips, T. W., Suter, L. J., and Wallace, R. J., *Beryllium-Ablator Implosion Experiments on Nova*, Lawrence Livermore National Laboratory, Livermore, CA, UCRL-JC-131358 ABS. Prepared for *40th Annual Mtg of the Div of Plasma Physics*, New Orleans, LA, Nov 16, 1998.

Kozlowski, M. R., Maricle, S., Mouser, R., Schwartz, S., Parham, T., Wegner, P., and Weiland, T., *Laser Damage Performance of Fused Silica Optical Components Measured on the Beamlet Laser System at 355 nm*, Lawrence Livermore National Laboratory, Livermore, CA, UCRL-JC-131221 ABS. Prepared for *30th Boulder Damage Symp: Annual Symp on Optical Materials for High Power Lasers*, Boulder, CO, Sept 28, 1998.

Kozlowski, M. R., Maricle, S., Mouser, R., Schwartz, S., Wegner, P., and Weiland, T., *3ω Damage Threshold Evaluation of Final Optics Components Using Beamlet Mule and Off-Line Testing*, Lawrence Livermore National Laboratory, Livermore, CA, UCRL-JC-129721. Prepared for *3rd Annual Intl Conf on Solid State Lasers for Application (SSLA) to Inertial Confinement Fusion (ICF)*, Monterey, CA, Jun 7, 1998.

Kruer, W. L., Campbell, E. M., Decker, C. D., Wilks, S. C., Moody, J., Orzechowski, T., Suter, L., Afeyan, B., and Dague, N., *Pushing the Limits: Strongly-Driven Laser Plasma Coupling*, Lawrence Livermore National Laboratory, Livermore, CA, UCRL-JC-130986 ABS. Prepared for *40th Annual Mtg of the Div of Plasma Physics*, New Orleans, LA, Nov 16, 1998.

L

Landen, O. L., Amendt, P. A., Barnes, C., Bradley, D., Craxton, S., Decker, C., Glendinning, S., Haan, S., Hammel, B., and Hauer, A., *Time Dependent Hohlraum Symmetry Control*, Lawrence Livermore National Laboratory, Livermore, CA, UCRL-JC-131373 ABS. Prepared for *40th Annual Mtg of the Div of Plasma Physics*, New Orleans, LA, Nov 16, 1998.

Langdon, A. B., Berger, R., Dixit, S., Kirkwood, R., MacGowan, B., Still, C., and Williams, E., *Modeling of Laser-Plasma Interactions with Beams Smoothed by Kinoform Phase Plates and by Random-Phase Plates*, Lawrence Livermore National Laboratory, Livermore, CA, UCRL-JC-131393 ABS. Prepared for *40th Annual Mtg of the Div of Plasma Physics*, New Orleans, LA, Nov 16, 1998.

Langer, S. H., *A Comparison of the Floating Point Performance of Current Computers*, Lawrence Livermore National Laboratory, Livermore, CA, UCRL-JC-130869; *Comput. Phys.* **12**(4), 338–345 (1998).

Langer, S. H., Scott, H. A., Marinak, M. M., and Landen, O. L., *Modeling Line Emission from ICF Capsules in 3 Dimensions*, Lawrence Livermore National Laboratory, Livermore, CA, UCRL-JC-131240 ABS Rev. Prepared for *8th Intl Workshop on Radiative Properties of Hot Dense Matter*, Sarasota, FL, Oct 26, 1998.

Langer, S. H., Scott, H. A., Marinak, M. M., and Landen, O. L., *Modeling Line Emission from ICF Capsules in 3 Dimensions*, Lawrence Livermore National Laboratory, Livermore, CA, UCRL-JC-131240 ABS. Prepared for *40th Annual Mtg of the Div of Plasma Physics*, New Orleans, LA, Nov 16, 1998.

Lasinski, B. F., *PIC Simulations of Ultra Intense Laser Pulses Propagating through Overdense Plasma for Fast-Ignitor Radiography Applications*, Lawrence Livermore National Laboratory, Livermore, CA, UCRL-JC-131245 ABS. Prepared for *40th Annual Mtg of the Div of Plasma Physics*, New Orleans, LA, Nov 16, 1998.

Lefebvre, E., Berger, R. L., Langdon, A. B., MacGowan, B. J., Rothenberg, J. E., and Williams, E. A., *Reduction of Laser Self-Focusing in Plasma by Polarization Smoothing*, Lawrence Livermore National Laboratory, Livermore, CA, UCRL-JC-127739; *Phys. Plasmas* **5**(7), 2701–2705 (1998).

Lerche, R. A., and Ognibene, T. J., *Error Analysis for Fast Scintillator-Based ICF Burn History Measurements*, Lawrence Livermore National Laboratory, Livermore, CA, UCRL-JC-129701. Prepared for *12th Topical Conf on High-Temperature Plasma Diagnostics*, Princeton, NJ, Jun 7, 1998.

Logan, B. G., Perkins, L. J., Ditmire, T. R., Rosen, M. D., Perry, M. D., Key, M. H., Diaz De La Rubia, T., and Wolfer, W. G., *High Flux, Petawatt-Laser-Driven, Neutron Source for Fusion Micro-Materials Irradiation*, Lawrence Livermore National Laboratory, Livermore, CA, UCRL-JC-131440 ABS. Prepared for *40th Annual Mtg of the Div of Plasma Physics*, New Orleans, LA, Nov 16, 1998.

Lund, S. M., and Davidson, R. C., *Warm-Fluid Description of Intense Beam Equilibrium and Electrostatic Stability Properties*, Lawrence Livermore National Laboratory, Livermore, CA, UCRL-JC-130614; *Phys. Plasmas* **5**(8), 3028–3053 (1998).

M

MacFarlane, J. J., Cohen, D. H., Wang, P., Peterson, R. R., Moses, G. A., Back, C. A., Landen, O. L., Leeper, R. J., Olsen, R. E., and Nash, T., *Development of Soft X-Ray Tracer Diagnostics for Hohlraum Experiments*, Lawrence Livermore National Laboratory, Livermore, CA, UCRL-CR-131541.

MacGowan, B. J., Berger, R. L., Cohen, B. I., Decker, C. D., Dixit, S., Geddes, C., Glenzer, S. H., Hinkel, D. E., Kirkwood, R. K., and Langdon, A. B., *Beam Smoothing Experiments at the Nova Laser*, Lawrence Livermore National Laboratory, Livermore, CA, UCRL-JC-131372 ABS. Prepared for *40th Annual Mtg of the Div of Plasma Physics*, New Orleans, LA, Nov 16, 1998.

Maricle, S. M., Wu, Z. L., Stolz, C. J., and Weakley, S. C., *Study of Damage Growth of Large Aperture HfO_2/SiO_2 Multilayer Coatings*, Lawrence Livermore National Laboratory, Livermore, CA, UCRL-JC-131220 ABS. Prepared for *30th Boulder Damage Symp: Annual Symp on Optical Materials for High Power Lasers*, Boulder, CO, Sept 28, 1998.

Marinak, M. M., Dittrich, T. R., Gentile, N., Kerbel, G. D., Haan, S. W., and Jones, O., *Advances in HYDRA and Its Application to National Ignition Facility (NIF) Capsule Designs*, Lawrence Livermore National Laboratory, Livermore, CA, UCRL-JC-131430 ABS. Prepared for *40th Annual Mtg of the Div of Plasma Physics*, New Orleans, LA, Nov 16, 1998.

Marshall, C., Erlandson, A., Horvath, J., Jancaitis, K., Lawson, J., Manes, K., Moor, E., Payne, S., Pedrotti, L., and Rotter, M., *Design and Performance of Amplifiers for the National Ignition Facility*, Lawrence Livermore National Laboratory, Livermore, CA, UCRL-JC-131963 ABS-S. Prepared for *14th Topical Mtg on Advanced Solid-State Lasers Conf*, Boston, MA, Jan 31, 1999.

McEachern, R., Alford, C., Cook, R., Wallace, R., and Bernat, T., *Studies of Morphology and Hydrogen Permeation in Sputter-Deposited Be and B-Doped Be Films*, Lawrence Livermore National Laboratory, Livermore, CA, UCRL-JC-131399 ABS. Prepared for *40th Annual Mtg of the Div of Plasma Physics*, New Orleans, LA, Nov 16, 1998.

Meier, W. R., Bangerter, R. O., and Faltens, A., *Integrated Systems Model for Heavy Ion Drivers*, Lawrence Livermore National Laboratory, Livermore, CA, UCRL-JC-128538. Prepared for *12th Intl Symp on Heavy Ion Inertial Fusion*, Heidelberg, Germany, Sept 24, 1997.

Milam, D., Eimerl, D., Auerbach, J. M., Barker, C., and Milonni, P. W., *Use of Alternating-Z Doubling in High-Dynamic-Range Tripling: Design and Evaluation of an Optimized Prototype Tripler*, Lawrence Livermore National Laboratory, Livermore, CA, UCRL-JC-131507. Prepared for *3rd Annual Intl Conf on Solid State Lasers for Application (SSLA) to Inertial Confinement Fusion (ICF)*, Monterey, CA, Jun 7, 1998.

Milam, D., Murray, J. E., Estabrook, K. G., Boley, C. D., Sell, W. D., Nielsen, N. D., Kirkwood, R. K., Zakharenkov, Y. A., and Afeyan, B. B., *Pinhole Closure Measurements*, Lawrence Livermore National Laboratory, Livermore, CA, UCRL-JC-129864. Prepared for *3rd Annual Intl Conf on Solid State Lasers for Application (SSLA) to Inertial Confinement Fusion (ICF)*, Monterey, CA, Jun 7, 1998.

Moody, J. D., MacGowan, B. J., Afeyan, B. B., Kirkwood, R. K., Glenzer, S. H., Kruer, W. L., Schmitt, A. J., and Williams, E. A., *Measurements of Small Scale Density Inhomogeneities in a Laser Plasma Using Near Forward Scattering*, Lawrence Livermore National Laboratory, Livermore, CA, UCRL-JC-131374 ABS. Prepared for *40th Annual Mtg of the Div of Plasma Physics*, New Orleans, LA, Nov 16, 1998.

Moran, M. J., Brown, C. G., Cowan, T., Hatchett, S., Hunt, A., Key, M., Pennington, D. M., Perry, M. D., Phillips, T., and Sangster, C., *Measurements of MeV Photon Flashes in Petawatt Laser Experiments*, Lawrence Livermore National Laboratory, Livermore, CA, UCRL-JC-131359 ABS. Prepared for *40th Annual Mtg of the Div of Plasma Physics*, New Orleans, LA, Nov 16, 1998.

Murphy, T. J., Wallace, J. M., Delamater, N. D., Barnes, C. W., Gobby, P., Hauer, A. A., Lindman, E., Magelssen, G., Moore, J. B., Oertel, J. A., Watt, R., Landen, O. L., Amendt, P., Cable, M., Decker, C., Hammel, B. A., Koch, J. A., Suter, L. J., Turner, R. E., Wallace, R. J., Marshall, F. J., Bradley, D., Craxton, R. S., Keck, R., Knauer, J. P., Kremens, R., and Schnittman, J. D., "Hohlraum Symmetry Experiments with Multiple Beam Cones on the Omega Laser," *Phys. Rev. Lett.* **81**(1), 108–111 (1998).

Murray, J. E., Milam, D., Boley, C. D., Estabrook, K. G., and Bonneau, F., *Spatial Filter Issues*, Lawrence Livermore National Laboratory, Livermore, CA, UCRL-JC-129751. Prepared for *3rd Annual Intl Conf on Solid State Lasers for Application (SSLA) to Inertial Confinement Fusion (ICF)*, Monterey, CA, Jun 7, 1998.

O

Ognibene, T. J., and Lerche, R. A., *Calculations into the Development of an ICF Burn History Diagnostic for NIF*, Lawrence Livermore National Laboratory, Livermore, CA, UCRL-JC-131370 ABS. Prepared for *40th Annual Mtg of the Div of Plasma Physics*, New Orleans, LA, Nov 16, 1998.

P

Paisner, J. A., *Effect of Laser-Induced Damage on the National Ignition Facility Optical Design*, Lawrence Livermore National Laboratory, Livermore, CA, UCRL-JC-131219 ABS. Prepared for *30th Boulder Damage Symp: Annual Symp on Optical Materials for High Power Lasers*, Boulder, CO, Sept 28, 1998.

Pennington, D. M., Brown, C. G., Cowan, T., Ditmire, T., Fountain, W., Hatchett, S., Hunt, A., Johnson, J., Kartz, M., and Key, M., *Petawatt Class Lasers and Applications to Laser–Matter Interaction Experiments*, Lawrence Livermore National Laboratory, Livermore, CA, UCRL-JC-131783 ABS. Prepared for *Women's Technical and Professional Symp*, San Ramon, CA, Oct 15, 1998.

Perkins, L. J., Logan, B. G., Tabak, M., Miller, D. C., Moir, R., Caporaso, G. J., and Latkowski, J. F., *Advanced Concepts for Inertial Fusion Energy*, Lawrence Livermore National Laboratory, Livermore, CA, UCRL-JC-131439 ABS. Prepared for *40th Annual Mtg of the Div of Plasma Physics*, New Orleans, LA, Nov 16, 1998.

Perry, M. D., Sefcik, J., Moran, M., and Snavely, R., *Fast Gated Detectors for Ballistic Imaging with Hard X-Rays*, Lawrence Livermore National Laboratory, Livermore, CA, UCRL-ID-131518.

Pollaine, S. M., Haan, S., Rothenberg, J., Dixit, S., MacGowan, B., Suter, L., and Williams, W., *National Ignition Facility Focal Spot Size Specifications*, Lawrence Livermore National Laboratory, Livermore, CA, UCRL-JC-131390 ABS. Prepared for *40th Annual Mtg of the Div of Plasma Physics*, New Orleans, LA, Nov 16, 1998.

R

Remington, B. A., Glendinning, S. G., Kalantar, D. H., Budil, K. S., Weber, S. W., Colvin, J., Kane, J., Wood-Vasey, M. W., Moore, K., and Keilty, K., *Hydrodynamics Experiments on Intense Lasers*, Lawrence Livermore National Laboratory, Livermore, CA, UCRL-JC-131249 ABS. Prepared for *40th Annual Mtg of the Div of Plasma Physics*, New Orleans, LA, Nov 16, 1998.

Remington, B. A., *Proceedings from the 2nd Intl Workshop on Laboratory Astrophysics with Intense Lasers*, Lawrence Livermore National Laboratory, Livermore, CA, UCRL-ID-131978. Prepared for *2nd Intl Workshop on Laboratory Astrophysics with Intense Lasers*, Tucson, AZ, Mar 19, 1998.

Rhodes, M. A., Fochs, S., and Biltoft, P., *Plasma Electrode Pockels Cell for the National Ignition Facility*, Lawrence Livermore National Laboratory, Livermore, CA, UCRL-JC-131208. Prepared for *1998 American Nuclear Society Annual Mtg*, Nashville, TN, Jun 7, 1998.

Rosen, M. D., *Physics Issues That Determine ICF Target Gain and Driver Requirements*, Lawrence Livermore National Laboratory, Livermore, CA, UCRL-JC-131381 ABS. Prepared for *40th Annual Mtg of the Div of Plasma Physics*, New Orleans, LA, Nov 16, 1998.

Rothenberg, J. E., Auerbach, J. M., Moran, B. D., Murray, J. E., Weiland, T. L., and Wegner, P. J., *Implementation of Smoothing by Spectral Dispersion on Beamlet and NIF*, Lawrence Livermore National Laboratory, Livermore, CA, UCRL-JC-129771. Prepared for *3rd Annual Intl Conf on Solid State Lasers for Application (SSLA) to Inertial Confinement Fusion (ICF)*, Monterey, CA, Jun 7, 1998.

Rothenberg, J. E., Browning, D. F., and Wilcox, R. B., *Issue of FM to AM Conversion on the National Ignition Facility*, Lawrence Livermore National Laboratory, Livermore, CA, UCRL-JC-129770. Prepared for *3rd Annual Intl Conf on Solid State Lasers for Application (SSLA) to Inertial Confinement Fusion (ICF)*, Monterey, CA, Jun 7, 1998.

Rothenberg, J. E., *Polarization Smoothing for the National Ignition Facility*, Lawrence Livermore National Laboratory, Livermore, CA, UCRL-JC-129769. Prepared for *3rd Annual Intl Conf on Solid State Lasers for Application (SSLA) to Inertial Confinement Fusion (ICF)*, Monterey, CA, Jun 7, 1998.

Rotter, M., Jancaitis, K., Marshall, C., Zapata, L., Erlandson, A., LeTouze, G., and Seznec, S., *Pump-Induced Wavefront Distortion in Prototypical NIF/LMJ Amplifiers—Modeling and Comparison with Experiments*, Lawrence Livermore National Laboratory, Livermore, CA, UCRL-JC-130044. Prepared for *3rd Annual Intl Conf on Solid State Lasers for Application (SSLA) to Inertial Confinement Fusion (ICF)*, Monterey, CA, Jun 7, 1998.

Rubenchik, A., Budil, K. S., Brown, C., Glendinning, S. G., Gold, D., Estabrook, K., Keilty, K., Liang, E., Pennington, D., and Perry, M. D., *Simulating High Speed Meteorite Impact Physics with Experiments on the Petawatt Laser*, Lawrence Livermore National Laboratory, Livermore, CA, UCRL-JC-131352 ABS. Prepared for *40th Annual Mtg of the Div of Plasma Physics*, New Orleans, LA, Nov 16, 1998.

Runkel, M., *Monte Carlo Simulation of the R/1 Automated Damage Test*, Lawrence Livermore National Laboratory, Livermore, CA, UCRL-JC-131515. Prepared for *30th Boulder Damage Symp: Annual Symp on Optical Materials for High Power Lasers*, Boulder, CO, Sept 28, 1998.

Runkel, M., Williams, W., and De Yoreo, J., *Predicting Bulk Damage in NIF Harmonic Generators*, Lawrence Livermore National Laboratory, Livermore, CA, UCRL-JC-131514. Prepared for *30th Boulder Damage Symp: Annual Symp on Optical Materials for High Power Lasers*, Boulder, CO, Sept 28, 1998.

Ryutov, D. D., Budil, K. S., Glendinning, S. G., Remington, B. A., Stone, J. M., and Drake, R. P., *Analysis of Hydrodynamic Instabilities at Photoevaporation Fronts in Astrophysical Settings*, Lawrence Livermore National Laboratory, Livermore, CA, UCRL-JC-131353 ABS. Prepared for *40th Annual Mtg of the Div of Plasma Physics*, New Orleans, LA, Nov 16, 1998.

S

Salleo, A., Chinsio, R., Campbell, J. H., and Genin, F. Y., *Crack Propagation in Fused Silica during UV and IR ns-Laser Illumination*, Lawrence Livermore National Laboratory, Livermore, CA, UCRL-JC-131218 ABS. Prepared for *30th Boulder Damage Symp: Annual Symp on Optical Materials for High Power Lasers*, Boulder, CO, Sept 28, 1998.

Sanchez, J. J., Giedt, W. H., and Pipes, J., *Design, Fabrication and Testing of a Prototype NIF Cryogenic Hohlraum*, Lawrence Livermore National Laboratory, Livermore, CA, UCRL-JC-131368 ABS. Prepared for *40th Annual Mtg of the Div of Plasma Physics*, New Orleans, LA, Nov 16, 1998.

Sangster, C. T., Cowan, T. E., Hatchet, S. P., Henry, E. A., Key, M. H., Moran, M. J., Pennington, D. M., Perry, M. D., Phillips, T. W., and Stoyer, M. A., *Nuclear Activation Techniques for Electron Jet Characterization in Short Pulse Laser Interactions with High Z Matter*, Lawrence Livermore National Laboratory, Livermore, CA, UCRL-JC-131369 ABS. Prepared for *40th Annual Mtg of the Div of Plasma Physics*, New Orleans, LA, Nov 16, 1998.

Sater, J. D., Kozioziemski, B., Collins, G. W., Pipes, J., and Burmann, J., *Cryogenic D-T Fuel Layers Formed in 1 mm Spheres by Beta-Layering*, Lawrence Livermore National Laboratory, Livermore, CA, UCRL-JC-128031 ABS Rev. Prepared for *40th Annual Mtg of the Div of Plasma Physics*, New Orleans, LA, Nov 16, 1998.

Schoenenberger, K. Colston, B. W., Maitland, D. J., Da Silva, L. B., "Mapping of Birefringence and Thermal Damage in Tissue by Use of Polarization-Sensitive Optical Coherence Tomography," *Appl. Opt*. **37**(25), 6026–6036 (1998).

Schwartz, S., Feit, M. D., Kozlowski, M. R., Mouser, R. P., and Wu, Z. L., *Current 3ω Large Optic Test Procedures and Data Analysis for the QA of National Ignition Facility*, Lawrence Livermore National Laboratory, Livermore, CA, UCRL-JC-131217 ABS. Prepared for *30th Boulder Damage Symp: Annual Symp on Optical Materials for High Power Lasers*, Boulder, CO, Sept 28, 1998.

Schwartz, S., Jennings, R. T., Kimmons, J. F., Mouser, R. P., Weinzapfel, C. L., Kozlowski, M. R., Stolz, C. J., and Campbell, J. H., *Vendor Based Laser Damage Metrology Equipment Supporting the National Ignition Facility*, Lawrence Livermore National Laboratory, Livermore, CA, UCRL-JC-129719. Prepared for *3rd Annual Intl Conf on Solid State Lasers for Application (SSLA) to Inertial Confinement Fusion (ICF)*, Monterey, CA, Jun 7, 1998.

Sheehan, L. M., Schwartz, S., Battersby, C., Dickson, R., Jennings, R., Kimmons, J., Kozlowski, M., Maricle, S., Mouser, R., and Rainer, F., *Automated Damage Test Facilities for Materials Development and Production Optic Quality Assurance at Lawrence Livermore National Laboratory*, Lawrence Livermore National Laboratory, Livermore, CA, UCRL-JC-131230 ABS. Prepared for *30th Boulder Damage Symp: Annual Symp on Optical Materials for High Power Lasers*, Boulder, CO, Sept 28, 1998.

Sheehan, L. M., Wu, Z. L., and Kozlowski, M. R., *Defect Characterization on Super-Polished Fused Silica Surfaces Polished for High Power Laser Application at 355 nm*, Lawrence Livermore National Laboratory, Livermore, CA, UCRL-JC-131216 ABS. Prepared for *30th Boulder Damage Symp: Annual Symp on Optical Materials for High Power Lasers*, Boulder, CO, Sept 28, 1998.

Shigemori, K., Ditmire, T., Remington, B. A., Rubenchik, A. M., Keilty, K., Liang, E., and Moore, K., *Measurements of Strong Blast Waves in Gas Targets*, Lawrence Livermore National Laboratory, Livermore, CA, UCRL-JC-131233 ABS. Prepared for *40th Annual Mtg of the Div of Plasma Physics*, New Orleans, LA, Nov 16, 1998.

Still, C. H., Berger, R. L., Cohen, B. I., Langdon, A. B., and Williams, E. A., *Large Scale Filamentation Simulations with pF3D*, Lawrence Livermore National Laboratory, Livermore, CA, UCRL-JC-131385 ABS. Prepared for *40th Annual Mtg of the Div of Plasma Physics*, New Orleans, LA, Nov 16, 1998.

Still, C. H., Langer, S. H., Alley, W. E., and Zimmerman, G. B., *Shared Memory Programming with OpenMP*, Lawrence Livermore National Laboratory, Livermore, CA, UCRL-JC-131544; *Computers in Physics* **12**(6), 577 (1998).

Strobel, G. L., Dittrich, T. R., Haan, S. W., Marinak, M. M., and Pollaine, S. M., *Requirements for Low-Mode Asphericity on Ignition Targets for the National Ignition Facility*, Lawrence Livermore National Laboratory, Livermore, CA, UCRL-JC-131428 ABS. Prepared for *40th Annual Mtg of the Div of Plasma Physics*, New Orleans, LA, Nov 16, 1998.

Suter, L. J., Amendt, P., Jones, O., Pollaine, S., and Tabak, M., *Increasing the Coupling Efficiency of Conventional NIF Hohlraums*, Lawrence Livermore National Laboratory, Livermore, CA, UCRL-JC-131388 ABS. Prepared for *40th Annual Mtg of the Div of Plasma Physics*, New Orleans, LA, Nov 16, 1998.

T

Tabak, M., *Ignition Scaling Issues for the Fast Ignitor*, Lawrence Livermore National Laboratory, Livermore, CA, UCRL-JC-127948 ABS Rev. Prepared for *40th Annual Mtg of the Div of Plasma Physics*, New Orleans, LA, Nov 16, 1998.

Turner, R. E., Amendt, P. A., Glendinning, S. G., Kalantar, D. H., Landen, O. L., Wallace, R. J., Cable, M. D., Hammel, B. A., Bradley, D., and Glebov, V., *X-Ray Drive Symmetry and Implosion Performance in OMEGA Cylindrical Hohlraums Driven by NIF-Like Multiple Cone Geometry*, Lawrence Livermore National Laboratory, Livermore, CA, UCRL-JC-131360 ABS. Prepared for *40th Annual Mtg of the Div of Plasma Physics*, New Orleans, LA, Nov 16, 1998.

V

Verdon, C. P., *Physics Experiments Planned for the National Ignition Facility*, Lawrence Livermore National Laboratory, Livermore, CA, UCRL-JC-131377 ABS. Prepared for *40th Annual Mtg of the Div of Plasma Physics*, New Orleans, LA, Nov 16, 1998.

W

Wang, L., Yan, M., Siekhaus, W., and Oberhelman, S., *Probing Nano-Defects in Fused Silica by Near-Field Scanning Optical Microscopy*, Lawrence Livermore National Laboratory, Livermore, CA, UCRL-JC-233584; *J. Appl. Phys.* **84**(6), 3016–3019 (1998).

Weber, S. V., Collins, G. W., Glendinning, S. G., Wallace, R. J., Ze, F., Dague, N., Jadaud, J. P., and De Sainte Claire, E., *Modeling of Characterization Experiments for NIF Ablator Materials*, Lawrence Livermore National Laboratory, Livermore, CA, UCRL-JC-131376 ABS. Prepared for *40th Annual Mtg of the Div of Plasma Physics*, New Orleans, LA, Nov 16, 1998.

Wharton, K. B., Hatchett, S. P., Wilks, S. C., Key, M. H., Moody, J. D., Yanovsky, V., Offenberger, A. A., Hammel, B. A., Perry, M. D., and Joshi, C., *Experimental Measurements of Hot Electrons Generated by Ultraintense (>10^{19} W/cm^2) Laser–Plasma Interactions on Solid-Density Targets*, Lawrence Livermore National Laboratory, Livermore, CA, UCRL-JC-129230; *Phys. Rev. Lett.* **81**(4), 822–825 (1998).

Wharton, K. B., Kirkwood, R. K., Glenzer, S. H., Estabrook, K. G., Afeyan, B. B., Cohen, B. I., Moody, J. D., and Joshi, C., *Observation of Energy Transfer between Identical-Frequency Laser Beams in a Flowing Plasma*, Lawrence Livermore National Laboratory, Livermore, CA, UCRL-JC-129856; *Phys. Rev. Lett.* **81**(11), 2248–2251 (1998).

Wharton, K. B., Kirkwood, R. K., Glenzer, S. H., Estabrook, K. G., Afeyan, B. B., Cohen, B. I., Moody, J. D., and Joshi, C., *Observation of Resonant Energy Transfer between Identical-Frequency Laser Beams*, Lawrence Livermore National Laboratory, Livermore, CA, UCRL-JC-130320 ABS Rev. Prepared for *40th Annual Mtg of the Div of Plasma Physics*, New Orleans, LA, Nov 16, 1998.

Widmayer, C. C., Nickels, M. R., and Milam, D., *Nonlinear Holographic Imaging of Phase Errors*, Lawrence Livermore National Laboratory, Livermore, CA, UCRL-JC-130142; *Appl. Optics* **37**(21), 4801–4805 (1998).

Wilks, S. C., Kruer, W. L., Cowan, T., Key, M., Langdon, A. M., Lasinski, B., Hatchett, S., Perry, M. D., Tabak, M., and Haines, M. G., *Ultra-Intense Laser-Plasma Interactions Present in the LLNL Petawatt Experiments*, Lawrence Livermore National Laboratory, Livermore, CA, UCRL-JC-131382 ABS. Prepared for *40th Annual Mtg of the Div of Plasma Physics*, New Orleans, LA, Nov 16, 1998.

Willi, O., Haines, M., MacKinnon, A., Borghesi, M., Glenzer, S., Estabrook, K., Hammer, J., Kruer, W., Moody, J., and Powers, L., *Investigation of Magnetic Fields in Laser Produced Plasmas*, Lawrence Livermore National Laboratory, Livermore, CA, UCRL-CR-131532.

Williams, E. A., Berger, R. L., Hinkel, D. E., and Langdon, A. B., *Augmented Ray-Based Laser Plasma Interaction Modeling*, Lawrence Livermore National Laboratory, Livermore, CA, UCRL-JC-131387 ABS. Prepared for *40th Annual Mtg of the Div of Plasma Physics*, New Orleans, LA, Nov 16, 1998.

Williams, W. H., *Simulations of a Phase Corrector Plate for the National Ignition Facility*, Lawrence Livermore National Laboratory, Livermore, CA, UCRL-JC-130033. Prepared for *3rd Annual Intl Conf on Solid State Lasers for Application (SSLA) to Inertial Confinement Fusion (ICF)*, Monterey, CA, Jun 7, 1998.

Wu, Z. L., Feit, M. D., Kozlowski, M. R., Rubenchik, A. M., and Sheehan, L., *Laser Modulated Scattering as a Nondestructive Evaluation Tool for Optical Surfaces*, Lawrence Livermore National Laboratory, Livermore, CA, UCRL-JC-131211 ABS. Prepared for *30th Boulder Damage Symp: Annual Symp on Optical Materials for High Power Lasers*, Boulder, CO, Sept 28, 1998.

Wu, Z. L., Feit, M. D., Rubenchik, A. M., Sheehan, L., and Yan, M., *Single-Beam Photothermal Microscopy—a New Diagnostic Tool for Optical Materials*, Lawrence Livermore National Laboratory, Livermore, CA, UCRL-JC-131212 ABS. Prepared for *30th Boulder Damage Symp: Annual Symp on Optical Materials for High Power Lasers*, Boulder, CO, Sept 28, 1998.

Wu, Z. L., Sheehan, L., and Kozlowski, M. R., *Laser Modulated Scattering as a Nondestructive Evaluation Tool for Defect Inspection in Optical Materials for High Power Laser Applications*, Lawrence Livermore National Laboratory, Livermore, CA, UCRL-JC-131548. Submitted to *Optics Express*.

Y

Yan, M., Oberhelman, S., Siekhaus, W., Wu, Z. L., Sheehan, L., and Kozlowski, M., *Characterization of Surface and Sub-Surface Defects in Optical Materials Using Near Field Evanescent Wave*, Lawrence Livermore National Laboratory, Livermore, CA, UCRL-JC-131225 ABS. Prepared for *30th Boulder Damage Symp: Annual Symp on Optical Materials for High Power Lasers*, Boulder, CO, Sept 28, 1998.

Young, P. E., Still, C. H., Hinkel, D. E., Kruer, W. L., Williams, E. A., Berger, R. L., and Estabrook, K. G., *Observations of Laser-Beam Bending Due to Transverse Plasma Flow*, Lawrence Livermore National Laboratory, Livermore, CA, UCRL-JC-129338; *Phys. Rev. Lett.* **81**(7), 1425–1428 (1998).

Z

Zaitseva, N., Atherton, J., Carman, L., De Yoreo, J., Torres, R., and Yan, M., *Rapid Growth of Large KDP and DKDP Crystals (55–57 cm) for Laser Fusion Applications*, Lawrence Livermore National Laboratory, Livermore, CA, UCRL-JC-131203 ABS. Prepared for *7th Intl Workshop on Laser Physics*, Berlin, Germany, July 6, 1998.

ICF/NIF/HEDES Program
Lawrence Livermore National Laboratory
P.O. Box 808, L-475
Livermore, California 94551

Address Correction Requested